



Center for Disaster Management and Risk Reduction Technology  
Projektbericht 4/2010

## Earthquake risk map development using GIS and optical satellite imagery: A case study for rural areas on Java, Indonesia

Eike - Marie Nolte

## **IMPRINT**

### **Editor**

#### **CEDIM**

Center for Disaster Management and  
Risk Reduction Technology  
c/o Karlsruhe Institute of Technology  
Hertz 16, D-76187 Karlsruhe

**Phone:** +49 721 6084436

**Fax:** +49 721 71173

### **Source cover picture**

Meskouris, K. & Renault, P. (Eds.):  
DGEB Erkundungsreise vom 01.07.-12.07.2006  
Erdbebenschäden bei Yogyakarta, Indonesien.  
DGEB-Publikation Nr. 14, 2006,  
ISBN 3-930108-10-0

# Table of Content

<b>1</b>	<b>INTRODUCTION</b> .....	<b>5</b>
1.1	Problem statement.....	6
1.2	Goals of the study .....	6
1.3	Limitations of the study .....	7
1.4	Organization of the study .....	8
<b>2</b>	<b>STUDY SITE AND DATA</b> .....	<b>11</b>
2.1	Concepts of hazard, vulnerability and risk.....	11
2.2	Earthquake Hazard in the Special Province of Yogyakarta .....	12
2.3	The 2006 Yogyakarta earthquake .....	14
2.4	Underlying data .....	14
2.5	Data uncertainty .....	16
<b>3</b>	<b>REVIEW OF BUILDING DAMAGE DETECTION USING SATELLITE IMAGERY</b> .....	<b>17</b>
3.1	Visual interpretation .....	17
3.2	Semi-automated image analysis .....	19
3.3	Fundamentals of object-oriented image analysis .....	21
3.3.1	Segmentation .....	21
3.3.2	Classification .....	22
3.4	Findings .....	24

## Table of Content

---

<b>4</b>	<b>DETECTION OF BUILDING DAMAGE OF THE 26.05.2006 YOGYAKARTA EARTHQUAKE .....</b>	<b>29</b>
<b>4.1</b>	<b>Pre-processing.....</b>	<b>30</b>
4.1.1	Co-registration Rectification of ground control points .....	30
4.1.2	Non-residential and cloud exclusion mask.....	30
4.1.3	Pansharpening .....	30
<b>4.2</b>	<b>Pixel-based building damage detection using PCI Geomatica .....</b>	<b>31</b>
<b>4.3</b>	<b>Object-oriented building damage detection using Definiens Developer 7 .....</b>	<b>32</b>
<b>4.4</b>	<b>Validation.....</b>	<b>33</b>
<b>5</b>	<b>LAND USE DETECTION FROM PRE-EVENT QUICKBIRD IMAGE.....</b>	<b>35</b>
<b>5.1</b>	<b>Analysis of pre-existing land use / land cover data sets .....</b>	<b>35</b>
<b>5.2</b>	<b>Analysis of class separability .....</b>	<b>36</b>
<b>5.3</b>	<b>Exploratory feature specific segmentation for pre-existing land cover data.....</b>	<b>39</b>
<b>5.4</b>	<b>Multi-resolution segmentation procedure and classification for land use data generation.....</b>	<b>41</b>
<b>5.5</b>	<b>Accuracy analysis .....</b>	<b>46</b>
5.5.1	Classification stability .....	46
5.5.2	Object-oriented, thematic accuracy assessment .....	46
<b>6</b>	<b>METHODOLOGY DEVELOPMENT .....</b>	<b>51</b>
<b>6.1</b>	<b>Analysis of damage influencing indicators.....</b>	<b>51</b>
6.1.1	Damage distribution and soil type.....	51
6.1.2	Damage distribution and bedrock / deposit age .....	53
6.1.3	Damage distribution and sediment thickness .....	55
6.1.4	Damage distribution and ground water level .....	56
6.1.5	Damage distribution and slope.....	57
6.1.6	Damage distribution and distance to epicentre .....	57

<b>6.2</b>	<b>Site specific assessment of earthquake-related hazards .....</b>	<b>59</b>
<b>6.3</b>	<b>Development of liquefaction susceptibility map .....</b>	<b>59</b>
<b>6.4</b>	<b>Development of amplification susceptibility map .....</b>	<b>62</b>
<b>6.5</b>	<b>Hotspot analysis.....</b>	<b>65</b>
<b>6.6</b>	<b>Exposure Assessment .....</b>	<b>66</b>
6.6.1	Residential buildings .....	67
6.6.2	Population density .....	67
6.6.3	Exposure Map .....	68
6.6.4	Result for Exposure Assessment .....	69
<b>6.7</b>	<b>Risk Assessment.....</b>	<b>70</b>
<b>7</b>	<b>DISCUSSION AND CONCLUSION.....</b>	<b>73</b>
<b>7.1</b>	<b>Discussion.....</b>	<b>73</b>
<b>7.2</b>	<b>Conclusion and outlook .....</b>	<b>78</b>
<b>8</b>	<b>REFERENCES .....</b>	<b>81</b>

Table of Content

---

# 1 Introduction

The assessment of earthquake risk is an important step towards reducing the impact of future earthquakes. Where extensive databases, models and resources are available, earthquake risk can be estimated; however, in many parts of the world earthquake risk is still poorly assessed and detailed risk assessment studies are not available. This is particularly true for remote, rural areas. Lacking valuable economic assets and infrastructural importance, rural areas seem to be of minor importance in seismic risk assessment studies.

Earthquake risk is a combination of three main elements – the seismic hazard, the assets at risk, and the vulnerability of the assets. On a small scale (10 km \* 10 km), the seismic hazard can be assumed to be quite uniform, if the site effects are not taken in account and no local faults can be considered to be capable of larger seismic events. This uniform seismic hazard is differentiated by site effects and collateral hazards induced by ground shaking such as liquefaction and soil amplification. In the hazard assessment part of this study, liquefaction and ground amplification are incorporated as collateral hazards. The assessment of liquefaction and amplification potential is usually based on a range of geotechnical data such as resistance or stress ratios. As field campaigns for data collection are very cost-intensive, in this study the influencing parameters are described by qualitative indicators derived from standard maps which are commonly available. The following parameters are considered: topsoil, bedrock, sediment thickness, slope, ground water depth, and distance to epicentre. In order to determine the influence of each parameter, a correlation analysis is conducted using building damage pattern from a selected earthquake event – the May 26<sup>th</sup> Yogyakarta earthquake. The very-high spatial resolution of the optical Quickbird satellite images enables the extraction of detailed damage distribution. Based on the identified correlations, a weighting scheme is developed and the weighted parameters are combined in an overlay analysis to generate the hazard map.

In general, three types of assets are at risk (Scawthorn, 2003). People can be killed or injured by earthquake effects most commonly by the collapse of man-made structures, particularly domestic dwellings. Money can be lost as for example reparation and recovery costs. Functions can be impaired or lost as for example business interruptions. Within the scope of this study, the assets at risk include residential building and population. Each asset is characterized by certain vulnerability and certain importance which form the basis for weighting the assets in the exposure analysis. The assessment of element at risk strongly depends on data availability. Satellite image provide a valuable source for inventory information and are used to improve pre-existing land use data.

The earthquake risk map is generated by combining the hazard and the exposure map using an overlay analysis. This qualitative approach to assess the loss potential based on ranked indicators is regionally transferable and enables therefore the generation of earthquake risk maps for regions located in the vicinity of the initial study site. In case of an earthquake striking a neighbouring region, the initially determined correlation can be recalibrated to the recent event. In accordance with the principle “the past is the key to the future“, taking into account the effects of past earthquakes on human settlements in rural areas is an important steps towards a methodology to rapidly generate earthquake risk maps.

Earthquake risk maps can be used in many applications in the field of disaster management. Land use planner can use information on locations of high potential loss for risk-sensitive decision making. In emergency planning, the spatial distribution of different risk zones can help to identify areas in the need for large resources to handle a future emergency. Civil protection agencies can use earthquake risk maps to plan the size and location of emergency services. In the aftermath of an earthquake, the risk map can be used to identify areas suitable for establishing temporary shelter or reconstructing destroyed buildings.

### 1.1 Problem statement

Existing earthquake risk assessment techniques rely on plenty of geological, geophysical and other environmental data. But detailed geotechnical surveys are time- and cost intensive and provide only point information. In addition, detailed information on the assets at risk is not readily available for many parts of the world. Qualitative indicators need to be integrated into the risk assessment methodology. The indicators have to be weighted based on their observed influence in past earthquakes.

To date, damage pattern extracted using remote sensing - especially very-high resolution images – have been mostly applied to guide rescue efforts and for rapid loss estimations. The potential of the high resolution of the extracted damage pattern to analyse the regional, damage influencing factors in detail has not been explored.

### 1.2 Goals of the study

The overarching goal of this dissertation research is to demonstrate that **earthquake risk maps can be developed by combining building damage distribution extracted from post-event satellite imagery and qualitative indicators.**

In order to address this overarching goal, the following specific goals are identified:

- 1. Evaluate and adjust methodologies for rapid building damage detection from Quickbird satellite imagery for rural, tropical areas**
- 2. Analyse the extracted damage pattern as a function of different environmental and ground parameters represented by qualitative indicators that influence building damage and develop a weighting scheme for the different indicators**
- 3. Develop a map for earthquake-related collateral hazards (liquefaction and amplification) using the weighting scheme (specific goal 2)**
- 4. Develop an exposure map for residential areas and population**
- 5. Develop an earthquake risk map combining hazard and exposure map**

The analysis of building damage pattern after an event arises from the essential need to increase the knowledge of what influenced the occurred damage and to incorporate this knowledge in the earthquake risk map development. Based on the correlations identified in the analysis, the developed weighting scheme provides a consistent way to index the different influencing factors. For the development of the exposure map, the built-up areas are extracted from the pre-event Quickbird and compared to pre-existing land use data to assure inventory is up-to-date. In addition, a data layer on population density is integrated in the exposure map to consider the influence of population density on the overall vulnerability. The earthquake risk map provides an insight into the spatial distribution of the local damage influencing factors. Considering the determined correlations as regionally valid, the methodology can be transferred to neighbouring regions.

### 1.3 Limitations of the study

While this research is focused on earthquake induced building damage, the image analysis technique cannot be easily transferred to other types of hazard induced building damage. For example, building damage pattern due to storm surge or flooding requires quite different techniques for being detected from satellite images since the water reflectance needs to be considered. Due to limited image data quality, this study is limited to building damage and does not include earthquake induced damage to infrastructure or other assets. However, in case geocoded information on infrastructure and infrastructure damage is available it can be easily integrated in the developed methodology. In addition, the developed methodology is limited to optical satellite imagery and cannot be transferred to other image data types.

In this study, the weighting scheme is developed for the May 2006 Yogyakarta earthquake, and is therefore scenario-based and only regionally valid. In order to transfer the developed methodology to other distant geographic locations, the weighting scheme needs to be recalibrated in case of an earthquake striking this region.

### 1.4 Organization of the study

This study is organized by objective topic. Chapter 2 presents the selected study site, the selected earthquake event, the underlying data and associated uncertainties. Chapter 2.1 introduces the concepts of hazard, vulnerability and risk used in this study. Chapter 3 consists of a literature review on existing damage detection techniques, including an evaluation and comparison of visual image interpretation and semi-automated techniques. In chapter 4, different approaches for building damage detection from Quickbird satellite imagery for the May 2006 Yogyakarta earthquake are compared. Chapter 5 presents an application of pre-event Quickbird images for land use data improvement. In chapter 6, a methodology for using remotely sensed building damage distribution for risk map generation including the analysis of the damage influencing factors is developed. Chapter 7 consists of the summary and an outlook of future work in these topics. The study framework demonstrates the motivation behind each of these chapters. This framework serves as a road map for this study, identifying the aims and objectives, techniques for achieving them and key outputs.

<b>General aim</b>	<b>To demonstrate that earthquake risk maps can be developed by combining building damage distribution extracted from post-event satellite image and qualitative indicators.</b>			
<b>Objective</b>	<b>1.</b> Introduce disaster-related concepts, study site and earthquake event	<b>2.</b> Examine existing literature on building damage detection from VHR image	<b>3.</b> Develop a rapid methodology for building damage detection from Quickbird image for rural, tropical areas	<b>4.</b> Utilize Quickbird images to improve pre-existing land use data
<b>How objective relates to aim</b>	Provides the terminology for the risk map development, location of the study area and the earthquake for which pre- and post-event satellite image are needed	Provides theoretical basis for work on this subject	Provides information on building damage distribution caused by the May 2006 Yogyakarta earthquake	Provides improved information on the spatial distribution of built-up areas
<b>Approach</b>	Investigate definitions of hazard, vulnerability and risk relevant to this study.	Investigate previous work to provide a starting point for the damage detection	Test and compare pixel-based and object-oriented image analysis procedures to detect building damage	Use object-oriented image analysis procedure to extract built-up areas
<b>Data required</b>	Previously published research on this topic; earthquake records, information on earthquake impact (damage, casualties)	Previously published research on damage detection from satellite imagery	Pre- and post event Quickbird images	Pre-event Quickbird image, land use data set
<b>Sources of data</b>	Literature review of previously published research; online databases, reports provided by institutions	Literature review of previously published research	Digital Globe	Geodetic Institute (KIT) Digital Globe

<b>General aim</b>	<b>To demonstrate that building damage risk maps can be developed by combining building damage distribution extracted from post-event satellite image and damage influencing factors.</b>			
<b>Objective</b>	<b>5.</b> Analyse the correlations between the building damage distribution and qualitative indicators	<b>6.</b> Generate map for earthquake-related collateral hazards	<b>7.</b> Develop an exposure map integrating residential areas and population density	<b>8.</b> Develop a risk map for building damage
<b>How objective relates to aim</b>	Provides basis for the weighting scheme used for hazard map generation	Provides information on the spatial distribution of susceptibility to collateral hazard in the study area	Provides information on the spatial distribution and the vulnerability of the exposure in the study area	Provides information on building damage potential in the study area
<b>Approach</b>	Analyse the distribution of building damage as a function of different factors	Combine weighted factors relevant to different collateral hazards	Weight the land use data set and the population density layer according to their vulnerability	Combine collateral hazard and exposure map from objective 5 and 6
<b>Data required</b>	GIS data set including environmental and ground information	Categorical factors weighted based on the building damage distribution	Land use data set, population layer	Collateral hazard and exposure map
<b>Sources of data</b>	Geodetic Institute (KIT)	Objective 4 this study	Geodetic Institute (KIT)	Objective 5 and 6 this study

## 2 Study site and data

The aim of this chapter is threefold: first to provide a consistent terminology for the risk map development, second to introduce the study site and the earthquake selected for this study, and third to provide an overview of the underlying data used in the analysis (objective 1).

### 2.1 Concepts of hazard, vulnerability and risk

The terms **hazard**, **vulnerability** and **risk** are widely used in disaster research terminology. Within in the scope of this study, a split definition of hazard, which is limited to earthquakes, is used. On the one hand, probabilistic hazard is defined as the probability of exceeding a particular level of ground motion (such as a certain value of peak acceleration) at a site during a specific time interval. Standard for a wide range of applications is a time period 475 years corresponding to an exceedance probability of 10 % in 50 years. In contrast to this probabilistic earthquake hazard, the deterministic hazard for a given scenario is defined by ground motion of a particular event with a specific hypocenter and magnitude. On a small scale (10 km \* 10 km), the seismic hazard can be assumed to be quite uniform, if the site effects are not taken in account and no local faults can be considered to be capable of larger seismic events. However, hazard can be differentiated by site effects and collateral hazards induced by ground shaking to display a more realistic picture. In this study, collateral hazard are defined as hazards that are induced by ground shaking such as liquefaction and soil amplification.

In general, three types of assets are at risk (Scawthorn, 2003). People can be killed or injured by earthquake effects most commonly by the collapse of man-made structures, particularly domestic dwellings. Money can be lost such as reparation and recovery costs. Functions can be impaired or lost for example business interruptions. Within the scope of this study, two assets at risk are considered: residential buildings and population. The exposure is defined as the ensemble of the assets at risk that can be disturbed by an earthquake event. So the residential areas of the study site and its population constitute the exposure for the earthquake risk assessment. For the exposure map generation, the assets are weighted by their vulnerability, which is defined as susceptibility to failure or loss of functionality, and by their importance. Risk can be defined as the potential of loss (physical, monetary, human) due to an earthquake for a defined area and a reference time period.

## Study site and data

### 2.2 Earthquake Hazard in the Special Province of Yogyakarta

Due to its geologic setting, Indonesia is prone to earthquakes. The tectonics of Java is dominated by the subduction of the Australia plate north-north-eastward beneath the Sunda plate with a relative velocity of 6 to 15 cm/year (Smyth et al., 2008). The Australian plate dips north-north-eastward attaining depth of approx. 100 - 150 km below Yogyakarta and depths of 600 km north of the island (see Figure 1).

There are historical records of earthquakes in Indonesia from 1900 to 2009. Information on earthquakes earlier than 1900 is really scarce. However, in the last decade the US Geological Survey recorded 48 earthquakes with magnitudes ranging from 6,3 to 7,9. In the recent past, Java was hit by numerous earthquakes. Among the most devastating events is the May 2006 earthquake which struck the south coast of Java (see section 2.3). Figure 2 displays the USGS earthquake hazard map of Indonesia. The Island of Java has a moderate to high hazard with PGA ranging from 1,6 to 3,2  $g/m^2$  for a 10 % exceedance probability in 50 years. The small scale earthquake hazard map shows a uniform moderate hazard for the study area (see Figure 3, study area indicated by rectangle).

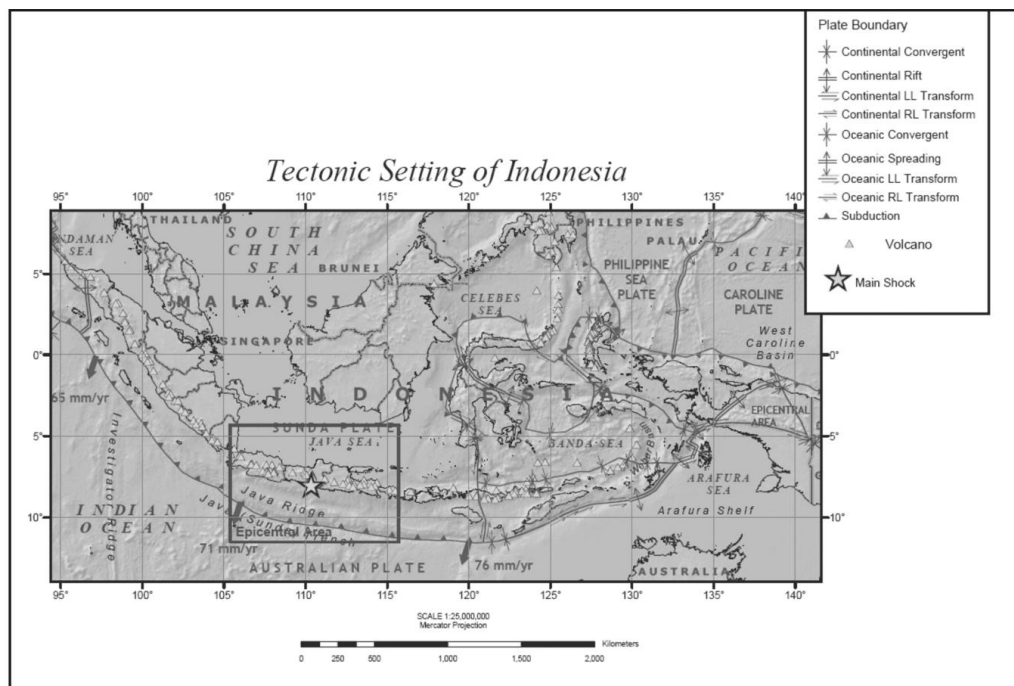


Figure 1 : Tectonic Setting of Indonesia. The Australian plate dips north-north-eastward beneath the Sunda Plate(US Geological Survey, 1997).

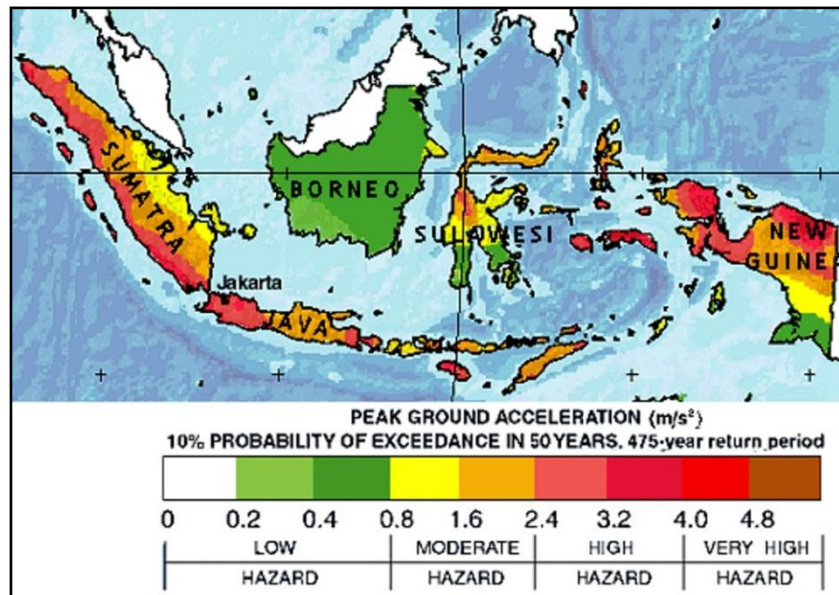


Figure 2: Seismic hazard map for Indonesia. The Island of Java has a moderate to high hazard with PGA ranging from 1,6 to 3,2 g/ m2 for a 10 % exceedance probability in 50 years (US Geological Survey, 1997).

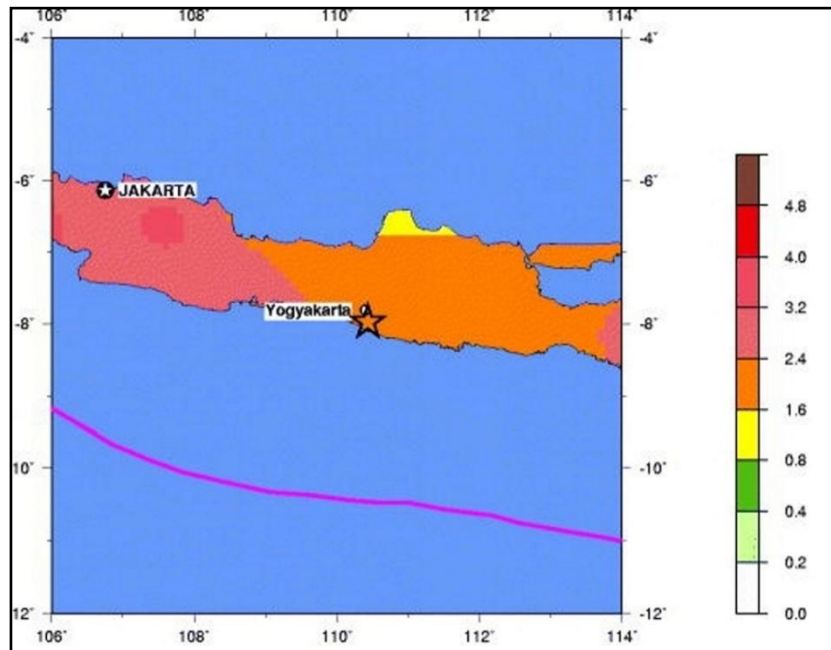


Figure 3: Regional, seismic hazard map for Java. On a small scale the map shows a smooth hazard distribution of the moderate hazard with ranging from 1,6 to 2,4 g/ m2 for a 10 % exceedance probability in 50 years (US Geological Survey, 1997).

### 2.3 The 2006 Yogyakarta earthquake

On May 27th 2006, an  $M_s$  6.3 (USGS) earthquake struck the Special Province of Yogyakarta, Java, at 5:53 local time. The Special Province of Yogyakarta is the smallest province of Indonesia and the last province still governed by a pre-colonial monarchy. It is subdivided into four regencies and one city, the capital of Yogyakarta city. The most hit regions were the districts Bantul and Klaten leaving 6.200 dead, 38.00 injured and over 150.000 displaced (Walter et al., 2007). More over 130.000 houses were destroyed and 450.000 were damaged. The large extent of damage revealed the vulnerability of the built environment to collateral hazards induced by ground shaking. Figure 5 shows the location of the selected 40 km<sup>2</sup> study area in the one of hardest hit provinces Bantul, south of Yogyakarta city.

### 2.4 Underlying data

In this study a range of different data sets are employed. Very-high resolution Quickbird images form the basis for the image analysis part of this study (see chapter 4 and chapter 5). Quickbird is one of the highest resolution, commercial sensors available at present, with a multi-spectral (R,G,B,NIR) resolution of 2,4 m and a panchromatic band of 60 cm. The pre-event image was acquired on July 11<sup>th</sup> 2003 and the post-event image was captured four days after the earthquake. For technical characteristics of the Quickbird sensor, please refer to section 2.4.1 in part I of the dissertation. From the post-event image, the extent of urban damage caused by the May 2006 Yogyakarta earthquake is detected. Figure 4 shows a comparison of the same village on the pre-event (left image) and post-event (right image).

A pre-event image scene is employed to delineate the urban areas of the study site in order to provide an up-to-date inventory for the exposure map development. Table 1 lists the characteristics of the employed Quickbird images. For the development of the building damage risk map presented in chapter 6, a range of data sets are applied. For the analysis of the damage distribution, information on soil and bedrock type, sediment thickness, ground water level, slope, and distance to epicentre is used. The slope is calculated based on a 27 m digital elevation model (DEM) which was kindly provided by Achim Roth from the German Aerospace Centre (DLR). Information on soil and bedrock type is provided by a detailed survey conducted by Sir MacDonald & Partners in 1984. The reports include 14 drilling profiles with detailed description of sediment type and thickness, bedrock formations, and ground water level. For more detailed information on individual drilling profiles see Appendix I. The layer distance to epicentre is generated using the Harvard CMT coordinates of the epicentre and calculating a buffer zone around the epicentre with a 1 km buffer distance. For the exposure map generation, information on the distribution of the urban areas and on population density is used.

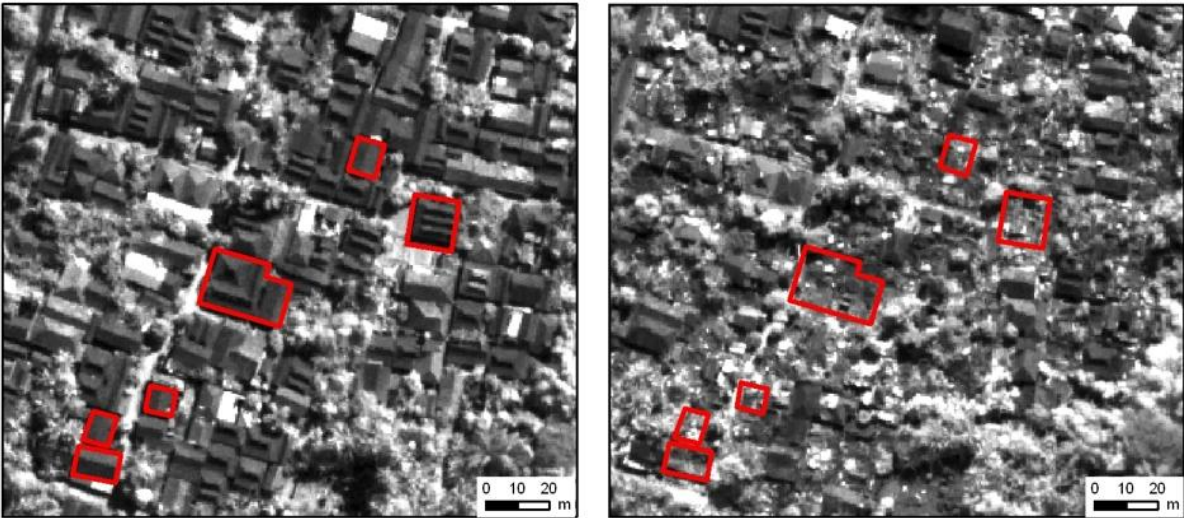


Figure 4: Quickbird panchromatic satellite image. Left: Pre-event image acquired 11.07.2003. Right: Post-event image captured four days after the earthquake (31.05.2006). The red rectangles indicate buildings that were destroyed by the May 2006 earthquake.

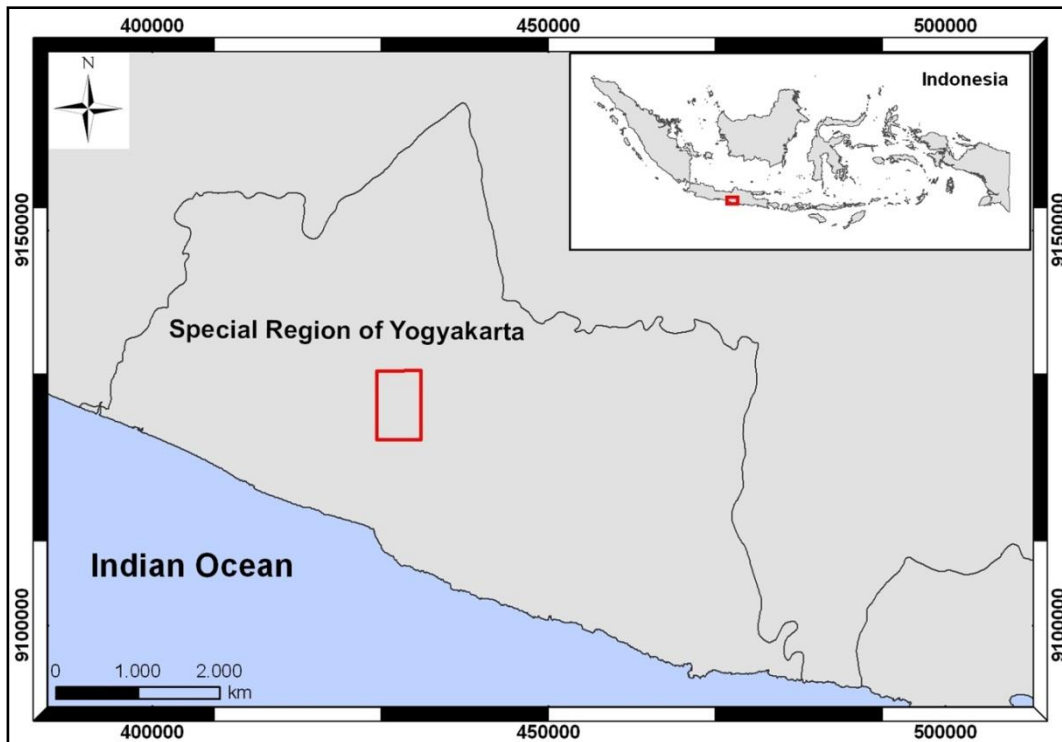


Figure 5: Location of study area in the Special Region of Yogyakarta, south cost of Java.

## Study site and data

---

The urban areas are delineated from pre-event Quickbird images and are available from pre-existing land use data sets. Information on population density on sub-district level is kindly provided by Marco Brenner from Geodetic Institute (KIT). Auxiliary data such as administrative boundaries and thematic maps for the Special Province of Yogyakarta and the district Bantul are also provided by the Geodetic Institute (KIT).

### 2.5 Data uncertainty

In this presented study, no field survey for data collection is conducted and therefore the study completely relies on data collected by other research institutions, companies or working groups. As data are collected through observation and measurements, uncertainty can be introduced in various forms such as mis-calibration of instruments, noisy or missing data (Pang, 2008). In the drilling campaign by Sir MacDonald & Partners (1984), a large group of staff might have been involved, so there is a variability associated with in the interpretation results of the drillings. The variability is caused by the different perception and experience among individuals and also the difference when asked to perform a task repeatedly. The slope calculation is based on a DEM. A DEM is a representation of topography with inherent errors that constitute uncertainty. Although a DEM is a model of the elevation surface; it is often not treated as a model, but accepted as a true representation of the earth's surface (Wechsler & Kroll, 2006). However, information concerning data collection, processing or error distribution is generally unavailable to DEM users (Holmes et al., 2000). The satellite images used in this study were acquired by the Quickbird sensor. Uncertainties associated with the images relate to the resampling and correction in the image generation process. In the acquired image, the pixels values are given in Digital Numbers (DN) and not in the original physical irradiance values in which the physical reflectance is received at the detector. A comprehensive overview of uncertainties of the Quickbird sensor and data processing is given by (Holekamp, 2006).

Table 1: Characteristics of Quickbird images used in this study.

Acquisition date	Resolution (panchromatic)	Resolution (multispectral)	Off-nadir	Cloud cover
11.07.2003	0,61m	2,46 m	6°	0%
31.05.2006	0,64m	2,54 m	13°	49%

## 3 Review of building damage detection using satellite imagery

The detection of building damage from satellite image is feasible because building damage can be identified through the reflective signature of broken bricks and tiles and other forms of damage which is distinctively different from undamaged intact buildings. This chapter provides a review of methodologies and technique used to extract information on earthquake-induced building damage from very high resolution, optical satellite images (objective 2). In general, remotely sensed images are processed using either visual interpretation or semi-automated methods. Previous studies have noted that the results obtained by either method are not always 100 % accurate. In many cases, one method was used to complement the other in order to increase the level of confidence attached to the results. In cases where ground truth data were not available, visual interpretation was used to assess the accuracy of the semi-automated classification. The purpose of this chapter is to identify technical and methodological conditions for using very high resolution, optical satellite images for damage pattern extraction caused by earthquakes in rural, tropical areas.

### 3.1 Visual interpretation

Visual image interpretation can be defined as the examination of images for the purpose of identifying objects and judging their significance. Human beings are well prepared to examine images, as our visual system and experience equip us to discern distinctions in brightness and darkness, to distinguish between various image textures, to perceive depth, and to recognize complex shapes and features (Campell, 2002). Because human beings possess a high level of proficiency in deriving information from images, they experience little difficulty in interpreting even those scenes that are visually complex. Nevertheless, there are three issues that distinguish interpretation of remotely sensed imagery from interpretation conducted in everyday experience: (1) remotely sensed image usually portray an overhead view – an unfamiliar perspective; (2) many remote sensing images use radiation outside the visible portion of the spectrum; (3) remote sensing often portrays the earth's surface at unfamiliar scales and resolutions.

Attempting to replicate these capabilities using computer programs, it becomes obvious how powerful human's abilities are to derive this kind of complex information (Campell, 2002). In most cases, visual interpretation cannot be replaced completely by computer techniques (Schowengerdt, 2007). However, there are certain advantages in on-screen interpretation of digital images such as the ability to modify the contrast level or the brightness of an image (Saito,

2008). Digital data usually have brightness ranges that do not match the capabilities of the human visual system. For example, if the maximum possible range of values is 0 to 255 (8 bit) but the display can only show the range from 0 to 63, then the image will have poor contrast, and important detail will be lost in the values that cannot be shown on the display.

For a number of past earthquakes, very high resolution satellite images have been utilized to detect and quantify the extent of urban damage using visual interpretation. Table 2 lists some examples documented in the literature. Among the first studies that applied these images for post-earthquake damage assessment was a study carried out by Saito et al. (2004) following the 2001 Gujarat (India) earthquake. Saito et al. (2004) used visual interpretation to determine different levels of damage according to the European Macroseismic Scale (EMS 98) from Ikonos image. This study revealed that damage sustained to high-rise building is easier to identify compared to that to low-rise buildings, with the exception of middle to high-rise buildings with soft storey collapse. Single storey buildings that had totally collapsed were clearly visible (Saito et al., 2004). The 2003 Boumerdes (Algeria) earthquake was the first major earthquake for which very-high-resolution satellite imagery has been extensively used for assessing damage severity (Saito & Spence, 2004; Yamazaki et al., 2004). Yamazaki et al. (2004) visually interpret damage level 3 to 5 on EMS 98 using change detection on Quickbird images. Visually interpreted damage survey using satellite images are likely to underestimate rather than overestimate the damage (Saito & Spence, 2004; Yamazaki et al., 2004). Similar studies were conducted following the 2003 Bam earthquake. Yamazaki et al. (2005) used visual inspection to determine different grades of building damage from Quickbird images. In order to assess the accuracy, Yamazaki et al. (2005) employed field data collected by Hisada et al. (2005). The comparison revealed that the best accuracy was achieved for the complete damaged buildings (EMS 98, Grade 5) and for the slightly and moderate damaged buildings (EMS 98, Grade 1 and 2). After the 2006 Yogyakarta Earthquake, the International Charter of 'Space and major disaster' had been activated to provide satellite images of the severely damaged areas. The preliminary maps of damage distribution published on the internet by UNOSAT are a good example for rapid damage estimation by visual inspection (Kerle, 2006).

Table 2: Previous studies on building damage detection from satellite images after earthquakes using visual image interpretation.

Country	Year	Earthquake	Source	Data
Japan	1995	Kobe	Matsuoka & Yamazaki 1998	Landsat TM
Turkey	1999	Kocaeli	Estrada et al. 2000 Olgun 2000 Turker & San 2003 Bitelli et al. 2004	Landsat TM Spot Spot IRS; Landsat
India	2001	Gujarat	Chiroiu & Andre 2001 Yusuf et al. 2001 Saito et al. 2004	Landsat 7 Ikonos Ikonos
Algeria	2003	Boumerdes	Yamazaki et al. 2004 Kouchi & Yamazaki 2005 Bitelli et al. 2004	Quickbird Quickbird Quickbird, IRS
Pakistan	2005	Kashmir and Jamur	Kumar et al. 2006	Cartosat 1
Indonesia	2006	Yogyakarta	Kerle 2006 Miura et al. 2006 Miura et al. 2007	Quickbird Quickbird Formosat 2

### 3.2 Semi-automated image analysis

The applied pixel-based techniques include change detection, image classification and texture analysis. A relatively new approach for building damage detection is object-oriented image analysis. The basic principle of using remote sensing data for change detection was defined by Singh (1989): “changes in land cover must result in changes in radiance values which must be large with respect to radiance changes from other factors”. In the case of building damage detection from pre- and post-event images, the “change” the applied techniques aim to detect refers to the transformation of intact buildings into damaged or destroyed buildings with corresponding rubble piles.

The spectral and textural characteristics of rubble piles or damaged buildings vary significantly from intact building roofs and can therefore be detected from optical satellite images. Most change detection algorithms operate pixel-wise. Image differencing and image rationing are the most applied algorithms for post-earthquake damage assessment (Ozisik, 2004). Using image differencing, co-registered images are subtracted. The co-registration of the images is an essential pre-processing step in order to avoid misaligned pixels. The decision whether a pixel has changed or not is based on a threshold value. The accuracy of this technique strongly depends on the setting of this threshold (Yuan et al. 1999). With the technique of image rationing, it is assumed that without a significant change of the spectral value of a pixel the ratio between two images will

be close to 1. This technique also requires co-registered images. Pixel based change detection techniques have been employed for building damage detection in various studies. Olgun (2000) detected building damage from SPOT images after the 1999 Kocaeli earthquake using image differencing, image rationing and the normalized differenced vegetation index (NDVI). Another study was conducted by Turker & San (2003) who used image differencing techniques on SPOT images. Building damage caused by the 2001 Gujarat earthquake was detected from Landsat by using image differencing and NDVI thresholds. A limited number of studies are documented using traditional, pixel-based supervised and unsupervised image classification techniques for building damage detection. An automated method for damage detection using maximum likelihood classifier applied after the 1995 Hyogoken-Nanbu earthquake were presented by Mitomi et al. (2001a).

The “change” from an intact building to rubble piles does not only lead to change in the spectral values; the textural characteristic changes as well. A number of studies include textural information in the damage detection techniques. Rathje et al. (2005a) used a combination of spectral and textural information to detect building damage after the 2001 Gujarat earthquake. After the 2003 Boumerdes earthquake, Rathje et al. (2005b) detected building damage from Quickbird pre- and post event images using the same combination. Woo et al. (2005) also utilize textural variations within Bam, in this instance combined with a correlation change detection function. Shirzaei et al. (2006) evaluate a multi-resolution wavelet transform technique for change detection in Bam, noting promising results compared with manual counts of building collapse. Following the 2003 Boumerdes earthquake, Adams et al. (2004) and Huyck et al. (2005) investigate semi-automated analytical approaches, mapping neighbourhoods sustaining building collapse as a function of textural changes between the pre- and post-event coverage. Also employing very high and high resolution satellite images, Vu et al. (2005) detected damaged buildings after the Bam 2003 earthquake from Quickbird and Ikonos images using edge information. In their study, they classified more than 80 % of the buildings as Grade 4 (very heavy damage) and Grade 5 (destroyed) on the EMS 98. The damage distribution they detected from Ikonos imagery was consistent with the results from Quickbird imagery. Testing different resampled spatial resolutions, Vu et al. (2005) conclude that in case of high versus very high resolution satellite imagery the spatial resolution does not affect the extraction results.

In contrast to the large number of previous studies on pixel-based, semi-automated building damage detection, the number of previous studies using object-oriented image analysis techniques is rather limited. Kouchi and Yamazaki (2005) used a mono-temporal, object-oriented approach to detect damage caused by the Bourmedes earthquake in 2003. Bitelli et al. (2004) applied multi-resolution segmentation by eCognition to determine image objects representing buildings, followed by a visual inspection of the after image to identify damaged buildings for the 2003 Boumerdes earthquake. In this study, Bitelli et al. (2004) also investigated the suitability of different spatial image resolution to detect building damage. Using moderate resolution satellite images (Landsat 7), high resolution image (IRS) and very-high-resolution images (Quickbird),

they tested pixel-based and object-oriented methods to detect building damage caused by the 1999 Kocaeli and the 2003 Boumerdes earthquake. After the May 2006 Yogyakarta earthquake, Matsumoto et al. (2006) conducted a pixel-based and object-oriented analysis for pre- and post-event images to detect building damage. A maximum-likelihood classification was applied to the pre- and post-event image and the extracted building areas were compared. Using ecognition Matsumoto et al. (2006) conducted an object-oriented analysis to extract different land cover classes including rubble as a separate class. Both results were compared using visual inspection, for the object-oriented analysis a producer accuracy of 67,4 % was achieved. Chiroiu et al. (2002) emphasize that object-oriented image analysis is most effective for extreme damage estates, where buildings have collapsed or are severely damaged.

In this study, a multi-temporal, pixel-based and a mono-temporal, object-oriented approach are used to detect building damage from Quickbird imagery. The results of both procedures are compared regarding their suitability to detect damage from Quickbird image in tropical, rural areas. In the following section, an overview on the fundamentals of object-oriented image analysis is provided.

### 3.3 Fundamentals of object-oriented image analysis

A number of different software exist for conducting object-oriented analysis (for examples and details see Baltsavias, 2004 and Gusella, 2006). But the number of off-the-shelf software solutions available to the research community is limited. E-cognition (now called Definiens Professional or Definiens Developer) was the first commercially available object-oriented image processing software (Benz et al., 2004). As Definiens Developer is used in this study, the background information is focussed on this particular software. Object-oriented image analysis can be subdivided into two major analytical procedures – segmentation and classification.

#### 3.3.1 Segmentation

Segmentation can be defined as an operation that splits a scene into objects. In Definiens Developer, object primitives are generated as a first step for further classification and other processing procedures (Baatz & Schäpe, 2000). The segmentation procedure uses a region growing approach combining spectral and shape information (Weidner, 2006). Since image object attributes such as colour, form and texture can be scale dependent, Baatz and Schäpe (2000) introduced the concept of multi-resolution segmentation which operates on the premise that objects of different sizes are present within an image. The multi-resolution region growing technique starts with single pixel objects which are iteratively merged into bigger objects. Definiens Developer uses a local mutual best fitting algorithm as a merging algorithm. Single image objects of 1 pixel size are used as so called seeds. These seeds are then merged into large

image objects, so called segments. When the best fitting is mutual, the image objects are merged. Otherwise the neighbour candidate becomes a new seed and looks in turn for its best fitting neighbour (Definiens, 2007). Each segment is considered once in one merging cycle, in order to maintain image objects of similar size (distributed treatment order of image objects) (Weidner, 2005). In this region growing procedure, the merging decision is based on local homogeneity criteria describing the similarity of image objects (Definiens, 2007; Baatz & Schäpe, 2000; Frauman & Wolff, 2005). For each possible merge, the degree of homogeneity is evaluated. The maximum deviation of the homogeneity is defined by the scale parameter (see equation 1).

$$\text{Homogeneity} = \text{scaleparameter} \cdot (h_{\text{shape}} \cdot w_{\text{shape}} + (1 - w_{\text{shape}}) \cdot h_{\text{spec}}) \quad \text{Equation 1}$$

Where  $h_{\text{spec}}$  relates to the spectral homogeneity criteria,  $w_{\text{spec}}$  is the spectral weight and  $h_{\text{shape}}$  is the shape homogeneity.

The homogeneity is defined by four internal criteria: compactness, smoothness, colour and shape (Definiens, 2007). The weights in percentage are equalized to the value of 1. For example, the spectral criterion defines the degree of change in spectral values within an image object and can be expressed as  $1 - \text{shape}$ . Thus by assigning a value to the shape field, the colour criteria is indirectly defined. The colour weight determines to what percentage the spectral values of the image layer will contribute to the entire homogeneity criterion. The shape criterion is used to optimize the shape of the image object's borders. The shape is determined by two parameters: smoothness and compactness. With Definiens Developer, each criterion can be adjusted by the user and the balance at which these criteria are applied depends on the desired output (Thomas, 2003). In addition to the above criteria, the segment-based approach allows for introducing relations to neighbour segments and context information (Weidner, 2006). This way user knowledge about the image scene can be integrated in the image analysis.

### 3.3.2 Classification

The objective of image classification is to substitute visual image interpretation with quantitative techniques for automating the identification of elements in a scene (Lillesand et al., 2008). Elements identified in the image are compared to characteristics of predefined classes. In classic classification methods, the assignment is based on a binary decision rule: An element belongs to a certain class (= 1) or an element does not belong to a certain class (= 0). Example for classic classification methods are maximum-likelihood or minimum-distance. Because of the binary decision process, these methods are called hard classifiers.

In contrast, with soft classifiers the degree of membership of an element to certain class is defined by fuzzy decision rules. This way a membership degree of 1 describes an explicit membership of an element to a class. The fuzzy system allows for dealing with uncertainties related to human assignment and is thus, closer to human perception (Baatz et al., 2004).

The “element” in an image scene mentioned in the preceding paragraph can refer to single pixels or to a group of assembled pixels i.e. objects. Pixel-based classification uses single pixels as a unit of analysis and the classification is based on the reflectance properties of the pixels. In addition to spectral properties, object-oriented classification also employs information on context, geometry and neighbourhood relations of the objects or relating to Definiens Developer, the segments. Two main classification methods are “supervised” and “unsupervised” classification (Lillesand et al., 2008). With supervised classification, examples of the class of interest are identified in the image. From these samples, the software develops a statistical characterization of the reflectance for each class. Once a statistical characterization has been generated for each class, the image is classified by examining the reflectance for each pixel and making a decision about which of the signatures it resembles most (Eastman et al., 1995). With unsupervised classification, clusters of the pixels are built automatically by the classification algorithm. The image analyst decides to which class the particular cluster belongs to.

Definiens Developer offers two kinds of supervised classifications: 1) nearest-neighbour classifier using samples and 2) membership functions which offer a transparent relationship between the object feature in the class description and the membership degree to a class (Definiens, 2007). Within the “process-based classification” tool set which includes different classification algorithms, the simplest algorithm allows for setting a threshold conditions and subsequent classification is based on a binary decision rule. The further advanced classification algorithm uses class descriptions to classify image objects. Based on the class description, the class membership value for each image object is calculated, where image objects with no class description are supposed to have membership value of 1. A range of expressions can be utilized for describing the characteristics of a certain class, for example thresholds, membership functions and similarities. For each object, a variety of features can be calculated. Among others, these features can be related to object properties such as area or length, to the position of an object within the segmentation hierarchy or to the class relation to the class relation of the object. The identification of suitable feature for describing classes is a time-consuming process. In order to avoid many cycles of “trial and error”, a preliminary analysis to evaluate the suitability of available features to describe image classes and to assure the class separability is an advisable step in the image classification process.

### 3.4 Findings

In this study, visual image interpretation is applied to delineate building outlines from the pre-event Quickbird image. Semi-automated image analysis procedures are used to extract building damage after the May 2006 Yogyakarta earthquake. Visual image interpretation is always subjective and the accuracy of the results depends on the interpreter's experience in image analysis and the background knowledge on the local conditions of the study site. A weakness associated with visual image interpretation is the missing comparability of the results by different interpreters. Semi-automated image analysis is also to some extent subjective as the thresholds and weights can be defined by the image interpreter. However, as the same algorithms are applied by all users and options for setting thresholds and weighting criteria are identical, the results can be easier compared. This is important because the subjective error in image analysis needs to be considered in the overall accuracy analysis of the results.

For the image analysis Quickbird images are employed with a off-nadir angle of  $6^\circ$  for the pre-event and  $13^\circ$  for the post-event image. Nadir image with  $0^\circ$  off-nadir angles are not available for the test site. The advantage of nadir images is that widespread shadowing is avoided. But nadir or near-nadir images do not provide information on building facades and are therefore not suitable for detecting wall cracks or other minor forms of building damage. The same applies to the detection of soft-storey collapse of buildings because the collapse of a soft story in a multi-story building does not necessarily lead to wide spread rubble or roof damage that could be detected from nearly nadir satellite images. Looking on a nadir images, a building that experienced soft story collapse due to ground shaking might look intact.

Quickbird images are satellite images with four spectral bands (R,G,B, and NIR). The spectral resolution of optical data for damage detection has a number of advantages. First, the spectral characteristics of imagery are comparable to human vision, making it easy to understand and interpret (Huyck et al., 2005). Second, the multi-band sensing capabilities in combination with very-high spatial resolution enable a very detailed distinction of different surface material, although not as detailed as hyper-spectral data. Another advantage is the large area coverage by optical image. For example at nadir, a basic Quickbird scene covers 16 by 16km – in total an area of  $256 \text{ km}^2$ . As the spatial resolution increases, the data volume and thus the computer system requirements for image analysis are also increasing. For example, the minimum order for standard, pan-sharpened Quickbird image from the archive is  $25 \text{ km}^2$ . With pan-sharpened pixel area of  $0,36 \text{ m}^2$ , the minimum order area of  $25 \text{ km}^2$  is consists of approx. 70.000.000 pixels per band.

The feasibility of the proposed methodology depends on the availability of the satellite image. The time gap between the actual event and the acquisition of the post-event image should be as small as possible. If change detection is applied, the time gap between the acquisition of the pre-event image and the event should be small as well. The availability of images depends on the

revisit time of the satellites. Due to increasing overlap in adjacent swaths, the revisit time – the time elapsing between two observations of a specific target area – is decreasing with higher latitudes, thus equatorial zones are less frequent imaged than near-pole areas. The revisit time for the Quickbird satellite sensor is 1 to 3.5 day, depending on latitude. Another factor influencing the revisit time is the altitude at which the satellite operates. The WorldView2 sensor operates at an altitude of 770 km and its revisit time is “typically 1.1 days” (Satellite Imaging Cooperation, 2010), whereas the Quickbird sensor operates at 450 km altitude. However, the technical revisit time does not necessarily mean the images are acquired at the same angle. Another issue regarding image availability is the passive acquisition system of the Quickbird sensor. Driven by solar radiation, optical systems are limited to daylight hours (Huyck et al. 2005). In addition for optical images, cloud cover is a constraint with optical images, especially in humid climate zones. Also dense vegetation cover is problematic when detecting damage since trees can cover collapsed buildings or rubble.

From an image purchasing perspective, initiatives such as the International Charter: Space and Major Disasters have made significant headway in making satellite images available. The Disaster Charter aims to provide satellite images and other remotely sensed data of a natural or man-made disaster free of charge to help to mitigate the effects on human lives and property and has been in place since 2000 (International Charter, 2009). The number of data providers is continuously increasing and most of the major satellite operators have now joined the charter which means that the common, remotely sensed data is now obtainable through the charter for organizations involved in relief efforts (Ozisik, 2004). Table 3 lists the members of the International Charter.

The free availability of satellite imagery by the International Charter points at an important issue regarding the use of commercial satellite imagery – the associated costs. The minimum order for standard, pan-sharpened Quickbird image from the archive is 25 km<sup>2</sup>, at a cost of 12,02€ (17\$) per 1 km<sup>2</sup>, giving a total of 300,50€ (425\$) (eurimage, 2010). In case the image scene needed is not available from the archive, image shots can be individually ordered from Digital Globe. This however is a very expensive option with prices ranging between 30 and 85€ per 1 km<sup>2</sup>. Regarding the costs associated with image analysis, the license fee for software packages has also to be taken into account. To date a number of off-the-shelf software solutions are available to the research community. Although companies offer educational discount for conducting research, the costs remain substantial. For example, the market leader for object-oriented image analysis software Definiens charges approximately 6000€ for their software package Definiens Developer. In the field of pixel-based image analysis and image processing, Creaso charges approximately 4400€ for their software package ENVI and PCI about 2000€ for PCI Geomatica.

## Review of building damage detection using satellite imagery

---

Table 3: Members and data providers of the International Charter. (International Charter, 2009)

<b>Member</b>	<b>Space Resources</b>
European Space Agency (ESA)	ERS, ENVISAT
Centre national d'études spatiales (CNES)	
Spotimage	SPOT
NSPO	Formosat
Canadian Space Agency (CSA)	RADARSAT
Indian Space Research Organisation (ISRO)	IRS
National Oceanic and Atmospheric Administration (NOAA)	POES, GOES
Argentina's Comisión Nacional de Actividades Especiales (CONAE)	SAC - C
Japan Aerospace Exploration Agency (Jaxa)	ALOS
United States Geological Survey (USGS)	Landsat
Digital Globe	Quickbird
GeoEye	GeoEye - 1
DMC International Imaging (DCM)	
Centre National des Techniques Spatiales	ALSAT - 1
National Space Research and Development	NigeriaSat
Tübitak - Bilten	BILSAT - 1
BNSC / Survey Satellite Technology Limited	UK - DMC
BNSC / Qinetiq	TopSat
China National Space Administration (CNSA)	FY, SJ, ZYsatellite series

## Review of building damage detection using satellite imagery

Table 4: Advantages and limitations of optical satellite imagery used for building damage detection after earthquakes

<b>Advantages</b>	<b>Remarks</b>
Large coverage area	The imagery spans a large geographic area, including numerous of affected settlements in a single frame.
Spectral characteristic similar to human vision	The spectral characteristics of optical data are comparable to human vision, making it easier for humans to understand and interpret.
Sub-meter spatial resolution	The sub-meter spatial resolution of optical data allows for identifying individual structures on the ground.
Less time consuming than field survey	Visual image interpretation and especially semi-automated image analysis is much less time consuming than field surveys.
Near global coverage	Earth-orbiting satellites acquire optical images throughout the world, including both developed and lesser developed countries.
Supplement existing maps	The generated damage map can supplement existing maps and databases, in particular in lesser developed countries where data availability is often limited.
Low risk	In the immediate aftermath of an earthquake event, when ground based assessment is extremely dangerous, decision concerning the scale of relief efforts can be safely made.
Independent of usual communication channels	In the immediate aftermath of an earthquake event conventional communication channels like broadcasting channels, telecommunication and computer networks satellite connections remain intact.
Input for initial loss estimation	The damage maps based on information extracted from satellite imagery provide data for initial loss estimation.
Variety of complementary sensors	A number of complementary sensors increase the probability that suitable, pre- and post-event images are rapidly available.
<b>Limitations</b>	<b>Remarks</b>
Damage hidden in shadows	Rubble and damaged buildings may be hidden in shadow areas and cannot be detected from the image. To reduce the shadow effect, nadir image should be used.
Damage to vertical walls	Damage to vertical walls cannot be detected from nadir or near-nadir image. Oblique or off-nadir images, if available, should be used in addition to nadir images to bridge this information gap.
Soft-story collapse	On nadir or near-nadir images, a building that experienced soft story collapse due to ground shaking might look intact.
Identification of non-disaster related differences	In case the time gap between the pre- and post-event image is too large, non-disaster related difference might be detected as damage using change detection methods. Secondary information on changes in land use or building inventory is very useful to exclude non-disaster related change from the damage maps.
Revisit time – time gap	The revisit time elapsing between two observations of a specific target area limits the availability of pre- and post-event images.

## Review of building damage detection using satellite imagery

---

<b>Limitations</b>	<b>Remarks</b>
Cloud cover	Clouds are a major constraint when using optical images as they may cover objects of interests.
Subjective image interpretation	The results of visual image interpretation are strongly depended on the interpreter's experience and prior knowledge of the event.
Image acquisition costs	High resolution satellite images are still very expensive, also initiatives like the International Charter aim at providing data free of charge after a catastrophic event.
Software purchase costs	Licence fees for commercial software package for image analysis remain very high.
Daylight hours	Optical satellite images are mostly collected by passive, solar driven sensors. Therefore, image collection is limited to daylight hours.
Vegetation cover	Vegetation can cover the object of interest and hinder information extraction.
Less accurate then field survey	Fewer details can be detected from satellite image than can be recorded in ground survey.

# 4 Detection of building damage of the 26.05.2006 Yogyakarta earthquake

In this chapter, the building damage caused by the May 26 earthquake south of Yogyakarta city is detected from very-high resolution Quickbird imagery (objective 3). Taken 5 days after the earthquake, the image clearly shows the wide spread destruction to the buildings. A pixel-based and an object-oriented methodology are tested and compared to identify advantages and limitations associated with both methods (see Figure 6). In order to assure that the extracted rubble pattern belong to damaged building, an overlay analysis is conducted using a building footprint data set for the test site which manually digitized from a pre-event image.

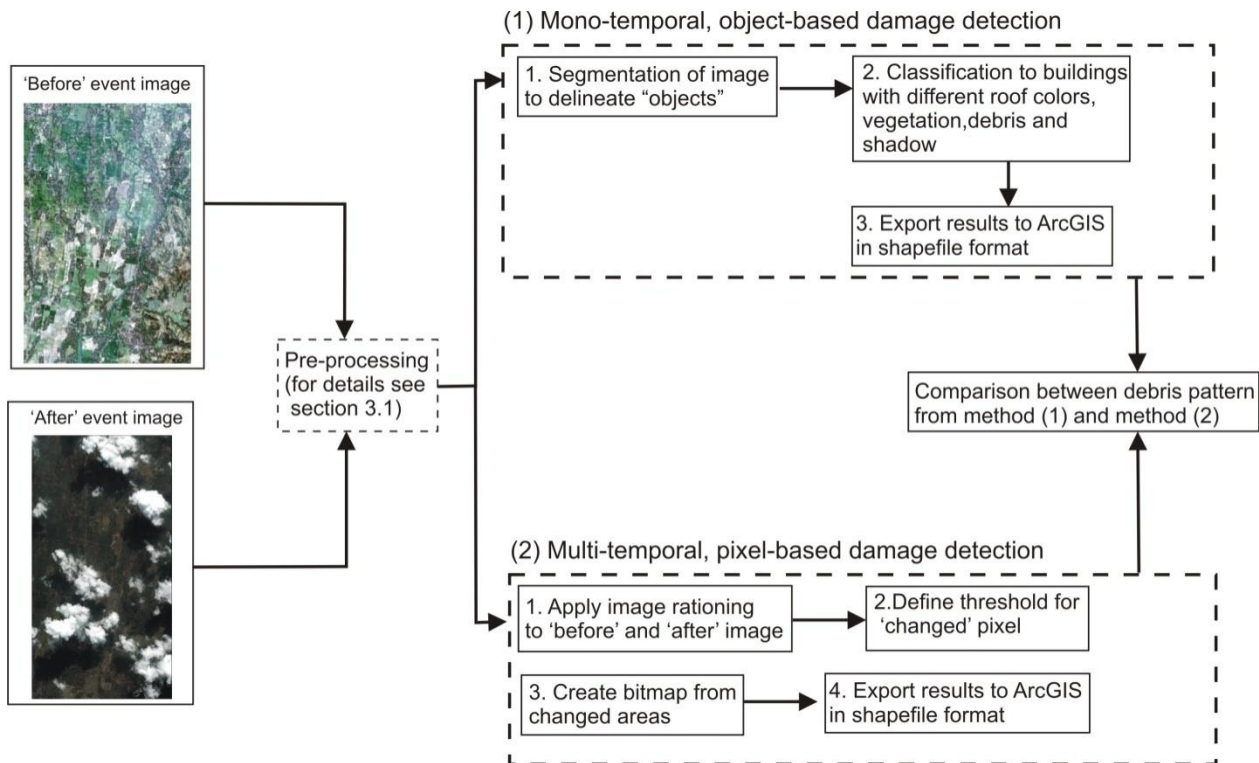


Figure 6: Methodology flow diagram illustrating two different procedures applied for damage detection from Quickbird imagery.

### 4.1 Pre-processing

Before the damage analysis can be undertaken, pre-processing of the available data set is required

#### 4.1.1 Co-registration Rectification of ground control points

One of the most important aspects of remote sensing-based change detection methodology is the exact overlay of the ground surface features. In theory, geographic locations within the two Yogyakarta images should correspond, since they have been geometrically corrected and georeferenced to a common projections and datum. However, initial visual inspection indicated that ground surface features remain slightly offset. To improve the geographic offset a co-registration process is undertaken. The Quickbird 2003 image is used as a master image. A set of 7 ground control points (GCPs) defined such as road junctions and building points is selected. The calculated spatial off-set values are listed in Appendix II with a mean easting off-set of 31,89 m. With respect to the pixel size of 2,4 m, the 2006 image is shifted 31,2 m in westward direction.

#### 4.1.2 Non-residential and cloud exclusion mask

A mask is created to eliminate the non-residential area is created using the improved land use data set (see chapter 5). This is used to limit the change detection to the urban area and minimize the effects of vegetation as a source of multi-temporal change. Since rubble detection for the clouded areas is not feasible based on optical images, a cloud exclusion mask is created from the 2006 post-event image. Due to a cloud cover of 49 %, the masked image covers only 23, 8 % of the original image.

#### 4.1.3 Pansharpening

As pan-sharpening technique offered by PCI Geomatica software is not available, a bilinear interpolation data merging function is used to merge the multispectral and panchromatic layers. This process also optimizes visual interpretation by combining the detail of the higher resolution panchromatic band with the information content of the red, green, blue and NIR spectral bands.

## 4.2 Pixel-based building damage detection using PCI Geomatica

In this section, a procedure for pixel-based urban damage detection from Quickbird imagery based on a direct, multi-temporal approach using *PCI Geomatica* software is presented (objective 4). The approach is based on the hypotheses that the building damage in the study area lead to an increase in reflectance within the optical bands of the spectrum, where dark roofs of intact buildings were replaced by lighter piles of rubble comprising the constituent materials. Most buildings in the study area are non-engineered, mixed constructions of reinforced concrete, masonry and wooden roof construction (for more information on the building types see section 6.6.1).

To examine the changes between pre- and post-disaster spectral building characteristics, a ratio image is computed. Using an *image rationing* procedure, areas of change between pre- and post-disaster images are identified. For this procedure, the *ARI* algorithm (image arithmetics) offered by *PCI Geomatica* is used. Only the red, green and blue bands are considered since urban structures generally show low reflection in the NIR spectrum. Technically, the images are divided and the spectral changes will be expressed as a quotient. It is assumed that for pixel which did not experience any change i.e. no damage the resulting quotient is approximately equal to 1. To classify a pixel as ‘changed’, a threshold for the quotient is defined using the mean values of the ratio – images and the standard deviation which is obtained using the ratio-image histograms (see Table 5). Finally a dataset of the changed areas is created. In order to allow a GIS analysis of the results, the bitmaps are converted into gis-compatible polygons and exported to a vector format (shapefile). Since a spectral reflectance increase is not necessarily caused by building collapse, an overlay analysis is conducted to identify the spectral changes related to buildings.

Table 5: Mean and standard deviation for defining the threshold for "changed" pixel

<b>Parameter</b>	<b>Red</b>	<b>Blue</b>	<b>Green</b>
Mean	1,28	1,29	1,28
Standard Deviation	0,19	0,23	0,35
Sum	1,48	1,52	1,63

### 4.3 Object-oriented building damage detection using Definiens Developer 7

In this section, a procedure for object-oriented building damage detection from Quickbird imagery based on a direct, mono-temporal approach will be presented (objective 4). An overview of the fundamentals of object-oriented image analysis as well as previous studies is presented in section 3.3. The damage is detected from imagery collected at a single time after the event (31.05.2006). In this procedure, damage is quantified in terms of extent of rubble piles.

In the first step, the pre-processed ‘after’-image is segmented using a very small scale parameter of 10. The very small scale parameter allows generating small segments and thus, to capture also small rubble piles. A very high compactness criterion of 0,9 and a shape criteria of 0,4 are used. In the second step, the segmented objects are divided into physically-based classes of buildings with different roof colours, building rubble, vegetation and shadow (see Figure 7). For each class, a class description is developed including spectral, textural and shape features (see Figure 8). In Definiens Developer a range of features is available. In this study, new features are developed which represent the percentage of each band for the brightness of a scene. For this sensor specific indices are employed (Kauth & Thomas, 1976; Ivits, 2005). For each feature a class specific function is developed.



Figure 7: Segmentation and Classification applied on Quickbird imagery. Figure A shows an image object representing a single house. Figure B shows the same Image Object classified as a House with a red roof.



Figure 8: Classes hierarchy used for the image classification and features applied in the class description.



Figure 9: Rubble classified using object-oriented image classification; the colour code corresponds to the classes in figure 6.

#### 4.4 Validation

In this section, the object-oriented and pixel-based procedures for damage detection are compared with respect to the accuracy of the detected debris pattern. The validation of the results is difficult as no detailed damage surveys are available from the May 2006 Yogyakarta earthquake. Available information on damage distribution is either very coarse like the preliminary damage maps by UNOSAT or very detailed providing only information about single damaged structures in Yogyakarta. Extensive surveys were only conducted in the urban areas of Yogyakarta, but not in the rural areas south of the city. So no validation information is available in a suitable

resolution. In order to at least undertake a minimum validation, an overlay analysis of the detected debris piles and the building outlines is conducted. This way the percentage of detected building debris piles is determined which serves as a criteria of the accuracy for the damage detection.

The pixel-based methodology is based on reflectance change of between intact and destroyed or damaged buildings identified in the 'before' and 'after' image. The extent of the detected rubble pattern showed minor variations for the different bands: 0,61 km<sup>2</sup> for the red band, 0,64 km<sup>2</sup> for the green band, and 0,63 km<sup>2</sup> for the blue band. The overlay analysis with the building outlines shows that only 33 % of the changes are related to buildings. For the object-oriented approach, the overlay analysis showed that 80 % of the detected damage pattern match buildings or are located very close to buildings. Interestingly, both methodologies detected about the same extent of rubble piles (approx. 0,62 km<sup>2</sup>).

The major source of error for the multi-temporal, pixel based approach is the time gap of three years between the pre- and post event image due to limited image availability. This large time gap results in the detecting a variety of changes not related to earthquake induced damage. Another source of error constitutes the manually digitized buildings from panchromatic pre-event image. Apart from the likelihood of not capturing all buildings in the image scene, only buildings built before 11.07.2003 (image acquisition date) are considered. From these findings, it can be concluded that the mono-temporal, object-oriented methodology is found to be more suitable for rapid building damage detection. The advantages and limitation of the methodology are summarized below.

### **Advantages of mono-temporal, object-oriented damage detection**

- The methodology does not rely on existing image acquired shortly before the event.
- No pre-processing to overlay the pre- and post event images is necessary.
- The rubble class can be explicitly defined. Neighbourhood relations allow for spatially relating the rubble class to buildings already in the image analysis.
- The large variety of available feature which allow for defining explicit image classes.
- In case the image quality is sufficient and the study area is suitable, single buildings can be detected.

### **Limitations of mono-temporal, object-oriented damage detection**

- The image classification is time- and computation-intensive
- The class descriptions have to manually defined and adjusted which requires experience from the image interpreter.
- The optimisation is a time-consuming, iterative process.

# 5 Land use detection from pre-event Quickbird image

The terms land use and land cover are often synonymously used throughout the literature. However in image analysis, it is essential to distinguish between land use (LU) and land cover (LC). Di Gregorio and Jansen (1997) define land cover as the physical description of space. This includes several bio-physical categories such as trees, grass land and paddy fields. The term land use involves the functional dimension of space for different human purposes or economic activities (Geist & Lambin, 2002). Typical categories for land use are dwellings, industrial or commercial use, transportation or recreational use. Land cover and land use are closely related, land use links land cover to the human activities that transform the landscape (NRC, 1999). Thus, grassland would be an example for land cover while grazing could be the corresponding land use.

Very-high resolution satellite imagery such as Quickbird is increasingly used for land cover detection. The very high spatial resolution allows for the identification of land cover details on a local scale. The disadvantage with very high spatial resolution satellite imagery is their relatively poor spectral resolution which is limited to four bands (B,G,R,NIR) for Quickbird. In this chapter, a methodology for improving the pre-existing land use data sets using Quickbird images is presented (objective 4).

## 5.1 Analysis of pre-existing land use / land cover data sets

In this section, the pre-existing land use data are analysed to determine the suitability of the pre-defined classes for image analysis. The analysis consists of two parts: (1) exploration of spectral separability of the predefined classes using a correlation analysis and (2) evaluation of applicability of the classes for image segmentation.

The data set encompasses the following land use classes: secondary forest, grassland, riverside, river, residential area and paddy field. This data set exhibits a number of inconsistencies and deficiencies: 1) the data set comprises a mixture of land use and land cover; 2) From a remote sensing perspective, the classes are defined by an unnecessary complex set of spectral, spatial and relational properties; 3) Some classes encompass a composition of land cover classes instead of a single class. This is problematic since different hierarchical levels are displayed on a single level. In order to avoid many cycles of “trial and error”, a preliminary analysis is conducted in order to evaluate the suitability of available features to describe pre-existing classes and to assure the class separability.

## 5.2 Analysis of class separability

For these pre-existing land use classes being utilized for image classification (not as a thematic layer but in as descriptive classes), it is crucial that the classes can be separated according to spectral, shape or textural criteria. An exemplary correlation analysis is presented here using the Pearson's correlation coefficient to determine the strength of linear association between NIR-Band , R-band and the NDVI which could be used for a class description.

In Definiens Developer, the *2 D Feature Space Plot* function is used to analyse the correlation between features which could be potentially used for the class description. It allows acquiring information of where the samples i.e. the given classes are situated in a two-dimensional feature space (Definiens, 2007). With the *2 D Feature Space Plot* the Pearson's correlation coefficient is calculated between the values of the selected features and the selected classes (see Figure 10). It allows for examining the distribution of feature values plotted on x-y axes of two different assigned features. Here a feature commonly used to distinguish vegetation from non-vegetation, the Normalized Difference Vegetation Index is explored. Due to the fact that living plants reflect more in the NIR and R range than non living surfaces, the degree of photosynthetically active vegetation within each pixel can be estimated using the NDVI . Two bands are needed to calculate this index: one containing reflectance values for the visible red (R) spectrum, and the second containing reflectance values for the near infrared (NIR) portion of the spectrum. The NDVI is the quotient of the difference and sum of these two datasets.

$$NDVI = \frac{NIR - R}{NIR + R} \quad \text{Equation 2}$$

The values vary in relation to the absorption of red light by plant chlorophyll and the reflection of infrared radiation by water-filled leaf cells. NDVI values range between -1 and 1, with values of 0,5 dense vegetation and values < 0 indicate no vegetation. In a first step, the NDVI value ranges for vegetation classes are explored (see Table 6). The NDVI for secondary forest covers a wide value range, because the secondary forest encompasses not only trees but also bush and other vegetation which allows for more reflectance of the bare soil and therefore leads to lower NDVI values and thus increase the value range. The class riverside includes the wooded areas next to the river and shows a smaller range of NDVI higher values due to the high tree ratio. Grassland has lower NDVI values because the ratio of chlorophyll and the leaf's water content is much lower than for other vegetation types. The most complex class is paddy field. The periodic cultivation and the high water level on paddy fields make it difficult to determine a NDVI range.

Table 6: NDVI ranges and Pearson's correlation coefficient for the NIR- and R-bands

Land use class	NDVI	Pearson's correlation coefficient for the NIR- and R-band
Secondary forest	0,18 – 0,70	0,31
Grassland	0,23 – 0,56	0,04
Paddy field	0,04 – 0,69	-0,12
Riverside	0,32 – 0,74	0,36
Residential areas	0,07 – 0,72	0,07
River	-0,07 – 0,20	0,81

From this, it becomes obvious that there is no significant correlation between the near-infrared and the red band for the selected vegetation classes (see Figure 10). In order to distinguish these classes using image classification, different features have to be employed. As expected, the high correlation coefficient for the river class indicated that the NDVI can be used to separate the water class from other land use classes. This exemplary correlation analysis for a vegetation index reveals that not all predefined land use classes are suitable for image analysis. The analysis also shows that the categories residential areas and secondary forest are of comparable scale and both are of high semantic abstraction. Both cover a range of objects which can be recognized from a close distance: residential areas covers houses, streets and other urban objects, secondary forest covers single trees, bushes and other vegetation species. The residential area class is defined by its occupancy rather than by its land cover. The riverside class refers to a spatial proximity to the river and not to the actual land cover. Both, residential area and riverside are generic classes which can be applied at a later stage of the classification process to aggregate semantic subclasses. Secondary forest is a forest which regenerates on native forest which has been cleared by swidden agriculture or logging. Chokkalingam, et al. (2000) point out that the crown cover of secondary forest in Java can range from < 40 % up to 80 %. It is important to note that this heterogeneity is difficult to cover by a single class. Strictly speaking, secondary forest and paddy field are land use classes rather than land cover classes because their functional dimension. In Table 7, a summary of the classes, their definition and suitability is given.

From this analysis it becomes obvious that classes previously defined for different purposes cannot be simply applied for image analysis. Problems arise from missing spectral separability and different abstraction levels. Thus, a new set of classes has to be defined for the image classification. The findings also apply to image segmentation, since the generation of meaningful segments is based on the separability of the classes which they represent. In order to create such segments for each class, the optimal scale parameter has to be defined. But the relation between the parameter values and the corresponding segmentation results is not very apparent. The time-consuming testing of a range of different permutations of colour, shape and scale segmentation parameters should be avoided.

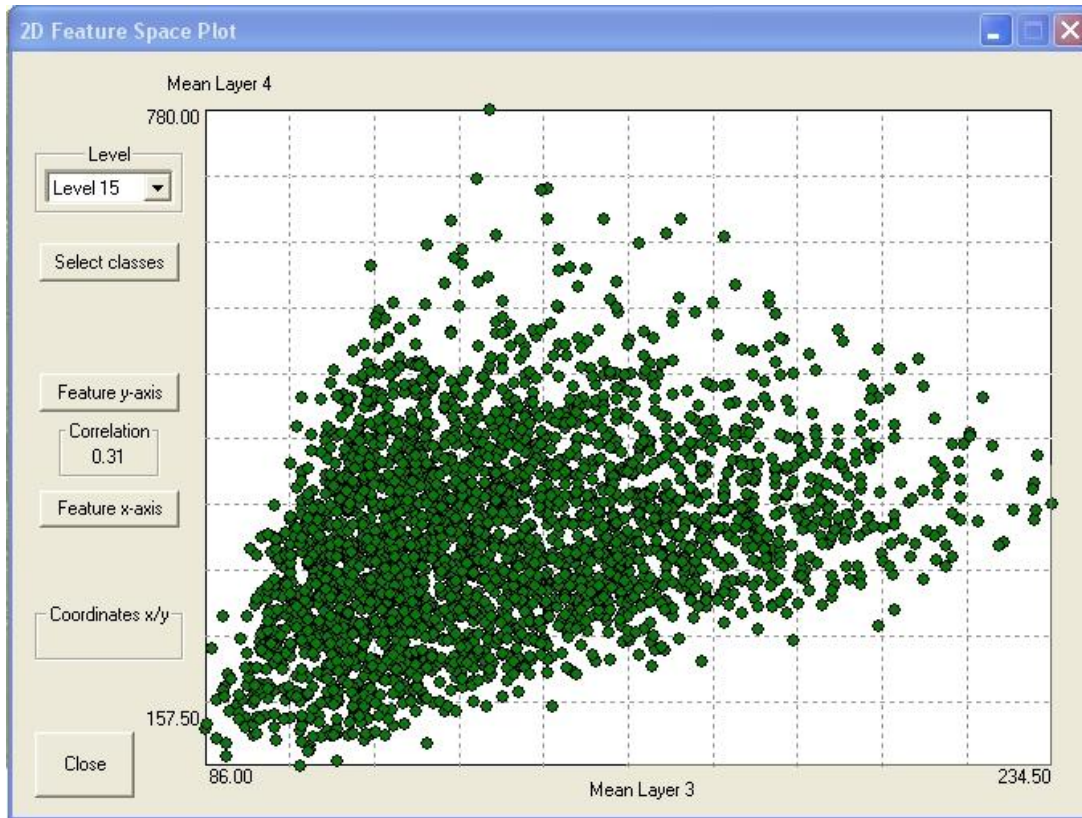


Figure 10: Snapshot of 2D Feature Space Plot. The plot displays the correlation between the red and the NIR band.

Table 7: Pre-existing classes and results of suitability analysis

Class	Definition	Land use / Land cover	Suitable for image analysis
Secondary forest	Definition by swidden or logging agriculture not by vegetation cover.	Land use	No
Grassland	Definition by vegetation cover and non-existing trees and bush vegetation	Land cover	Yes
Paddy field	Definition by cultivation and agriculture	Land use	No
Riverside	Definition by spatial proximity to river	Land use	No
Residential areas	Definition by habitat	Land use	No
River	Definition by existence of water body	Land cover	Yes

### 5.3 Exploratory feature specific segmentation for pre-existing land cover data

In a first step, for each land cover type an image subset is created. Each subset is segmented using the panchromatic and the multi-spectral channels by incrementally increasing the scale parameter until the resulting segments are representative for a specific land use class. In the segmentation process, it is assumed that the homogeneity of meaningful segments relies on the reflectance properties of the land cover rather than on its geometry. Therefore a very low shape criteria 0,1 is used, meaning the corresponding the colour criteria is weighted 0,9. From visual image inspection, it is seen that the desired land cover classes do not show specific degree of compactness. Additionally, the outline boundaries vary in their irregularity. Therefore the compactness and smoothness are equally weighted. Throughout the segmentation process the scale parameter is iteratively increased, starting with a very small scale parameter of 10. For each segmentation run, the number of generated segments and the scale parameter is recorded. Afterwards the results are displayed as correlation curves to determine a range of scale parameters which are suitable to generate meaningful segments for each specific land cover class. Regardless to the number of pixels, all curves are characterized by an initial, steep decrease in the number of image objects between a scale parameter of 10 and 30 (see Figure 11). This is due to the small increase in heterogeneity allowed for each merge. This results in a high number of homogeneous segments and thus, to a large number of potential merging partners for the following segmentation run. Since the overall increase in heterogeneity remains rather small when merging these homogeneous segments, a large number of merges is conducted and the number of segments decreases rapidly. Since the resulting segments become more heterogeneous with every merge, the number of generated segments decreases gradually until it reaches a quasi - consistent scale.

Utilizing these correlation curves, a scale parameter range which allows for the generating of meaningful segments for each land cover type is identified. The optimal scale parameter which generates meaningful, consistent image objects is assumed to lie within this range. For each land cover class, the determined value ranges show significant differences (see Table 8). For classes which are spectrally rather homogeneous meaningful segments are generated with smaller scale parameters than for heterogeneous classes. This is due to the fact that representative segments for fields have to encompass a higher degree of spectral variability than segments representing grass land. The field class covers paddy fields with different cropping periods from bare soil to flooded paddy fields. Segmentation with a very high scale parameter would create segments which encompasses the different fields but would also include other neighbouring land cover types thus lead to under-segmentation. Further difficulties are encountered with residential areas. Residential areas are defined as area predominantly used for housing, but it can also include parks, gardens etc. From this it becomes obvious that residential area is by no means a land cover type which can be described by simple spectral characteristics. Therefore a high scale parameter is necessary to create representative segments. The class river side is defined by its spatial proximity to the river. There for the generation of segments based on spectral properties is not

## Land use detection from pre-event Quickbird image

feasible. The findings of this exploratory study proof that land use classes which are defined by visual image interpretation and thus, meaningful with respect to human perception are not automatically suitable for a physically driven segmentation procedure. Due to the high spectral heterogeneity of the classes, a very high scale parameter is necessary to generated meaningful segments. But this kind of segmentation covers also neighbouring areas with different land cover. The defined classes have to be rather homogeneous from a spectral perspective to be suitable for segmentation. This leads to the importance to clearly distinguish between land use and land cover. A land cover class should not include a functional or spatial dimension. Land use classes on the other hand can be useful for aggregating land cover classes at a later stage of classification for example trees, grass land and houses might be aggregated to residential areas.

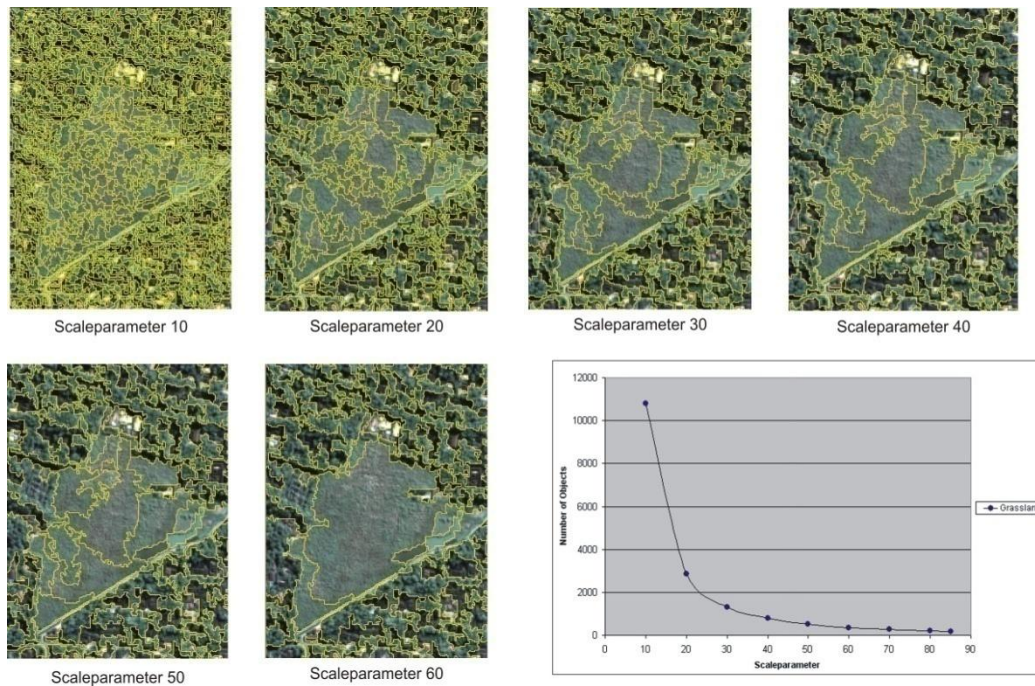


Figure 11: Segmentation with incrementally increasing scale parameter for the land cover class grass land. The correlation curve displays an initial, steep decrease in the number of image objects between a scale parameter of 10 and 30.

Table 8: Scale parameter ranges determined from the exploratory feature specific segmentation.

Land Use	Scale Parameter
Grassland	70 - 80
Riverside	105 – 110
Forest	134 – 140
Field	140 – 160
Residential Area	120 – 130

#### 5.4 Multi-resolution segmentation procedure and classification for land use data generation

In this section, a multi-resolution segmentation and classification methodology procedure is applied to extract an up-to-date land use inventory from the pre-event Quickbird image (see methodology flow diagram Figure 12).

##### **Multi-resolution segmentation**

The Quickbird image was acquired at an almost vertical angle (6° off-nadir). Therefore, the imagery shows rather small shadow areas. In order to detect these small shadow areas, a very small scale parameter is initially utilized. For example, To distinguish between the overhanging trees on the Opak riverbank and the river itself a scale parameter of 15 is applied. For the generation of small scale segments the shape and colour criteria are equally weighted. The irregularities of the shoreline caused by the overhanging trees is considered using a compactness criteria of 0,7 and thus a smoothness criteria of 0,3. In order to assess the quality of the segments, a visual comparison is conducted. Since the geometry of the segments is used later in the class description, it is important that the segments represent the river class correctly (Weidner & Bähr, 2007). The generated level of segmented object will be referred to as “Level 15” in the following sections. Although the classes in the pre-existing data set cannot be directly applied for image analysis, they can constitute valuable secondary information. Here the outlines of residential areas are initially used as a thematic layer to divide *Level 15* into residential and non-residential areas. For further classification, the Definiens ‘fuzzy’ classification methodology is utilized. For a comprehensive theoretical overview of fuzzy classification see (Shackelford & Davis, 2003).

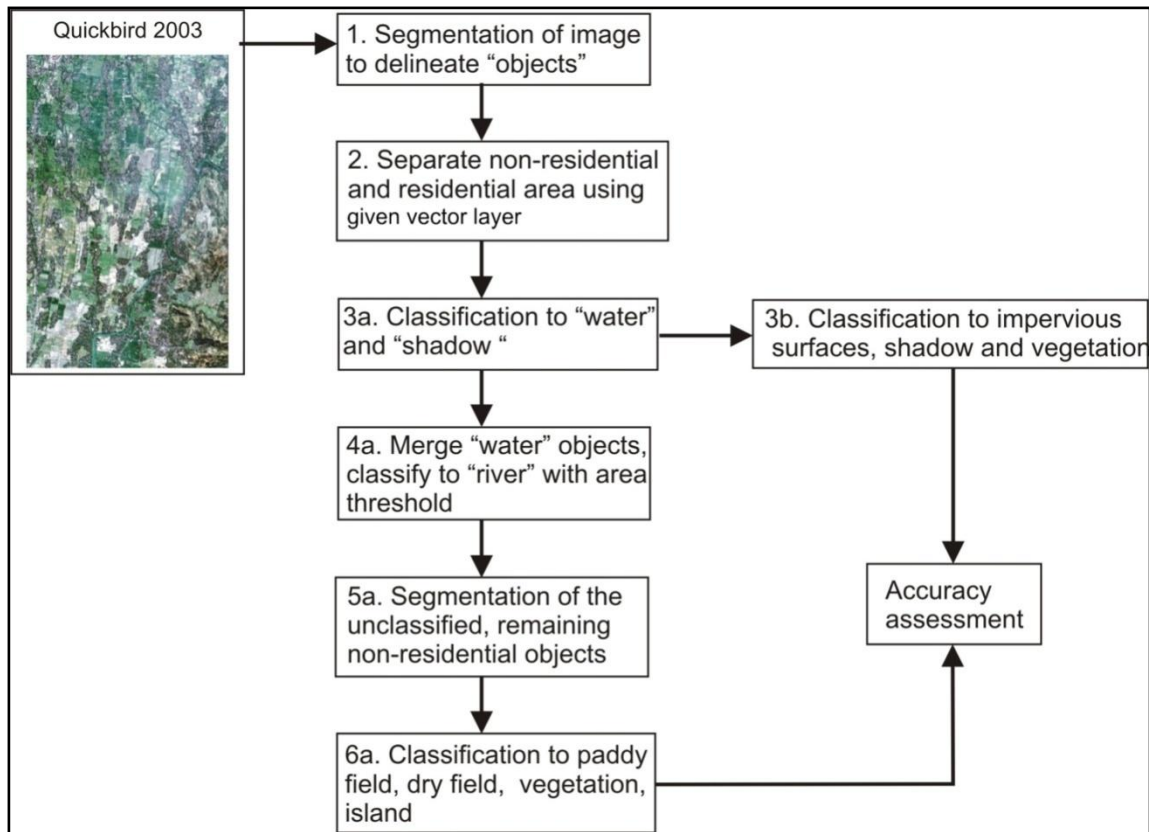


Figure 12: Methodology flow diagram for multi-resolution segmentation and classification of pre-event Quickbird imagery to determine an up-to-date land use inventory.

The implemented algorithm enables a broad range of variables relating to shape, texture, hierarchical and neighbourhood properties and features including spectral signatures. For each class, a class description is designed based on these variables, features and neighbourhood relationships. For each class and feature to be used, membership functions have to be defined (see Figure 13). At first, the non-residential image objects of *Level 15* are divided into physically-based and semantic-based classes of: water and shadow. The water class is described by the NDVI and the mean layer value of the NIR. These features are commonly used to identify water from imagery since water yield very low NIR and NDVI values. In a next step, the water objects are merged and the threshold for separating the river from other water bodies is defined as area > 1700 m<sup>2</sup>. The residual water objects are assigned to the non-residential class. To distinguish the shadows from other image objects, the features brightness and contrast to neighbour pixel in layer 4 (NIR) are applied.

## Land use detection from pre-event Quickbird image

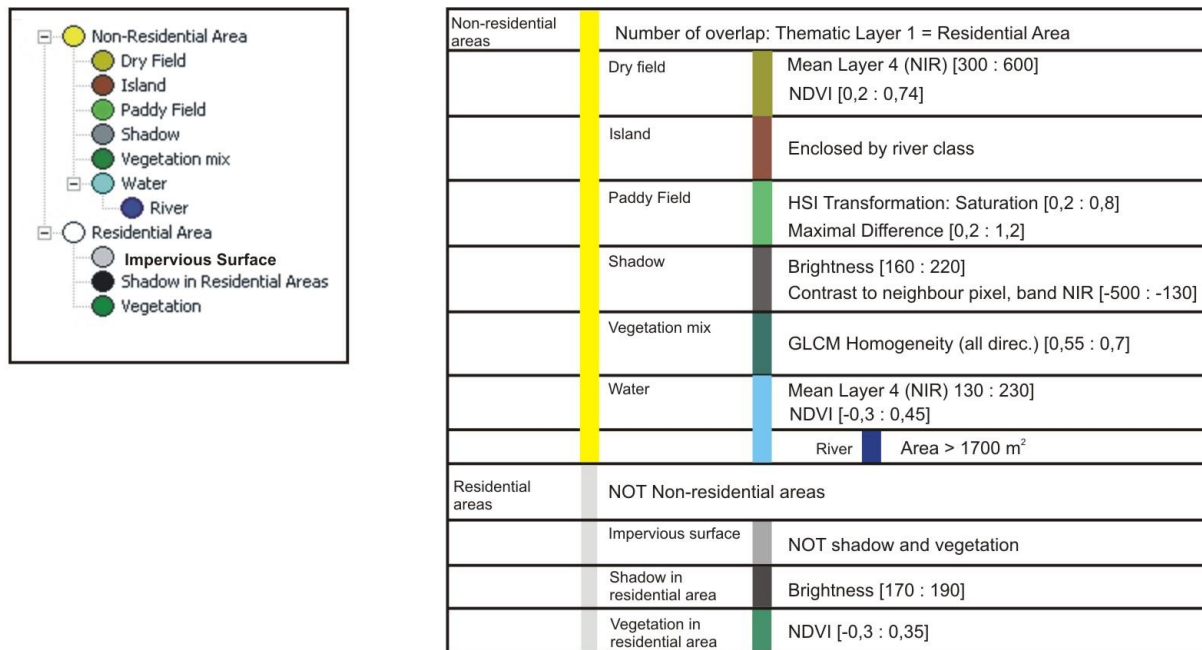


Figure 13: Classes hierarchy used for image classification and features applied in the class description for the different land use / land cover classes.

In order to create meaningful objects for the land use classes paddy field, dry field and vegetation mix, segmentation is conducted utilizing an iteratively increasing scale parameter from 15 to 80, with increments of 10 on the remaining, non-residential objects. The homogeneity criteria are defined as compactness 0,7 and shape 0,5 with equally weighted the spectral and shape properties. The regular form of the fields warrants the high values of compactness. For the classification of the paddy field, the features maximum difference and saturation are used. The maximum difference is calculated by subtracting the minimum mean values of an image object from its maximum value. The maximum and the minimum values of an object are determined by comparing all contributing layers. The saturation is calculated by a transformation of the values of the RGB (red, green, blue) colour space to the values of the HSI (hue, saturation, intensity) colour space. The saturation value is representing the intensity of a specific hue. The mixed vegetation areas including forest and riverbank trees show a significant lower textural homogeneity than agricultural used fields. So for their classification, the feature GLCM homogeneity (grey level co-occurrence matrix) is used. The class description of the dry fields includes the NDVI and the mean layer value of the NIR. In the next step, all image objects enclosed by the river class are assigned to the island class. The very last analysis step includes the classification of the residential areas. Here the initial segments generated with a scale parameter

## Land use detection from pre-event Quickbird image

---

of 15 are used due the small real world objects such as single buildings and trees within the residential area. First, the shadow within the residential areas is classified using the brightness values. Classes for vegetation in residential areas and sealed surface representing houses, streets and partly bare soil are defined. For vegetation detection the NDVI is used. The impervious surfaces are extracted using logical conditions, so that all unclassified image objects within a residential area are assigned to this class. Figure 14 displays the resulting land use / land cover map generated from the pre-event Quickbird image.

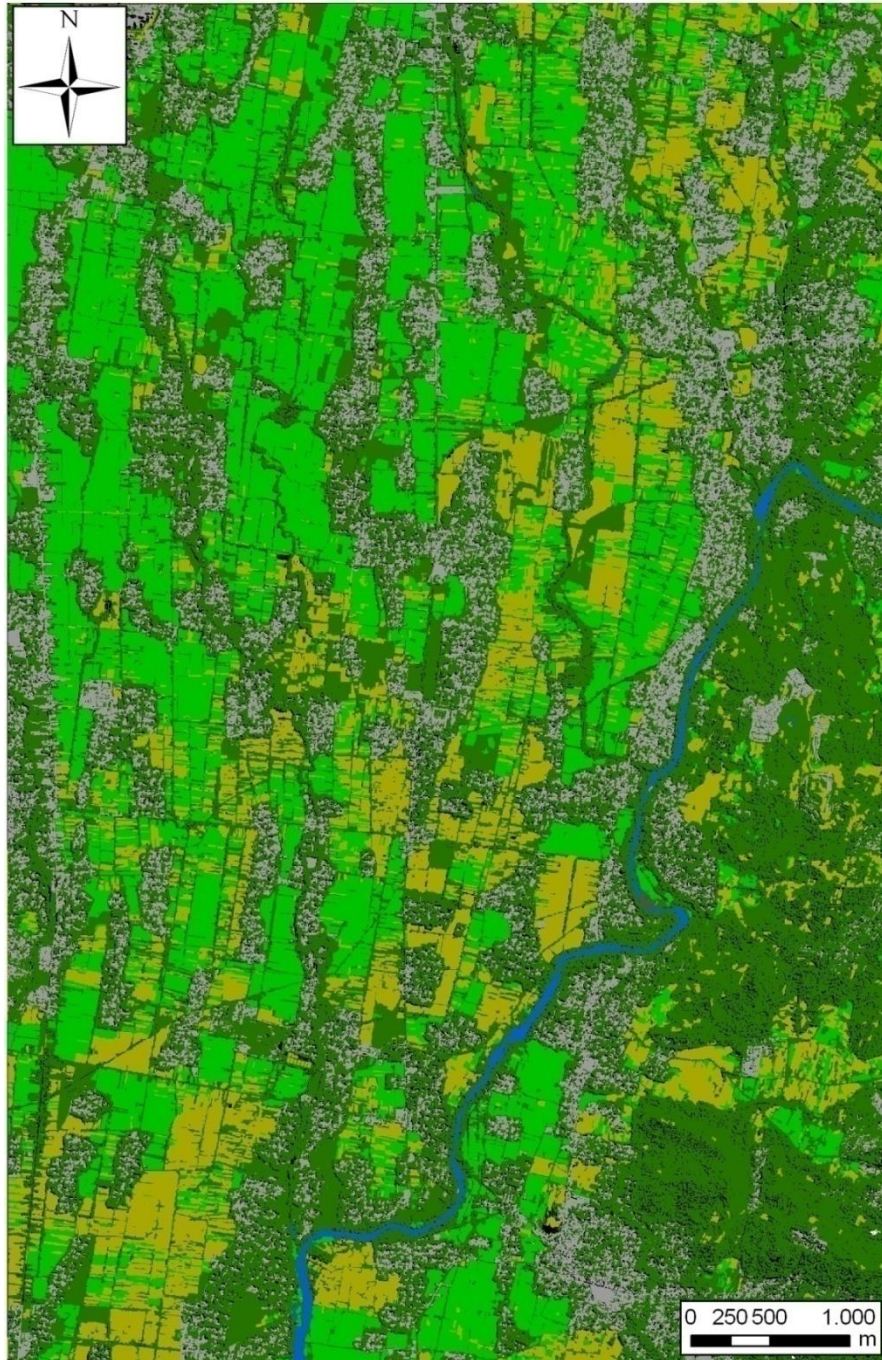


Figure 14: Land use / land cover map generated from pre-event Quickbird Imagery using an object-oriented, multi-resolution approach. The colour scheme corresponds to the class hierarchy in Figure 13.

### 5.5 Accuracy analysis

In this section, the performance of the fuzzy classification with the defined rule sets and class descriptions is investigated. Definiens Developer 7 offers different tools to evaluate the quality of image analysis results including statistical tools and error matrix. In addition, a methodology for thematic, GIS-based accuracy assessment based on a comparison of the automatic classified land use and a reference data set is developed.

#### 5.5.1 Classification stability

The classification stability is a statistic tool for evaluating the plausibility of rule sets. It is based on the difference between the best and the second best class membership of an image object. Classes with an explicit description without fuzzy conditions e.g. island or classes that are defined using thematic layer e.g. non-residential areas naturally achieved the best classification stability. The rather low stabilities for the shadow in non-residential areas can be explained by the high, spectral similarity to the surroundings such as partially flooded paddy fields and trees (see Figure 15).

#### 5.5.2 Object-oriented, thematic accuracy assessment

In this section, a thematic, object-oriented procedure for accuracy assessment is developed. In a first step, 10 reference areas are selected and the land cover types are manually digitized using the pre-event, panchromatic Quickbird image acquired in 2003 (see Figure 16). In order to be representative, each reference data set has to cover the major classes. For the resulting vector data set, the area for each land cover type is calculated. The results of the image classification is exported from Definiens into a vector format and then imported to ArcGIS. To cross tabulate the two data sets, the ArcGIS function tabulate areas is employed using the remotely-sensed classes as zones. For each zone, the surface ration of reference data set is calculated. The findings are inserted into a confusion matrix which is realized in an excel spread sheet. For each reference area, the user's and producer's accuracy, the overall accuracy and the kappa coefficient are calculated. The reference data sets cover a total of 103,7 ha. The accompanying confusion matrix shows the degree of correspondence between the classified and the digitized land use classes for the reference data sets (see Table 9). The accuracy of the whole classification is 76,66 %. In case of the river class less than 10 % of the reference data sets are misclassified. This corresponds with a 'User accuracy' of 91,21 % and a 'Producer accuracy' of 88,62 %. Figure 17 shows the surface percentage of all reference data sets compared to the land use classification. It is seen that in some instances the building roofs and other impervious surfaces and their surroundings can cause confusion if spectral properties are too similar.

In this study for instance, confusion arose between some buildings and overhanging trees because of the spectral similarities between the dark roofs and the leaves. The similarity of green vegetation and sprouting rice seedling on paddy fields also resulted in some confusion. This results in a lower accuracy producer accuracy of 68,73 % and user accuracy of 59,83 %.

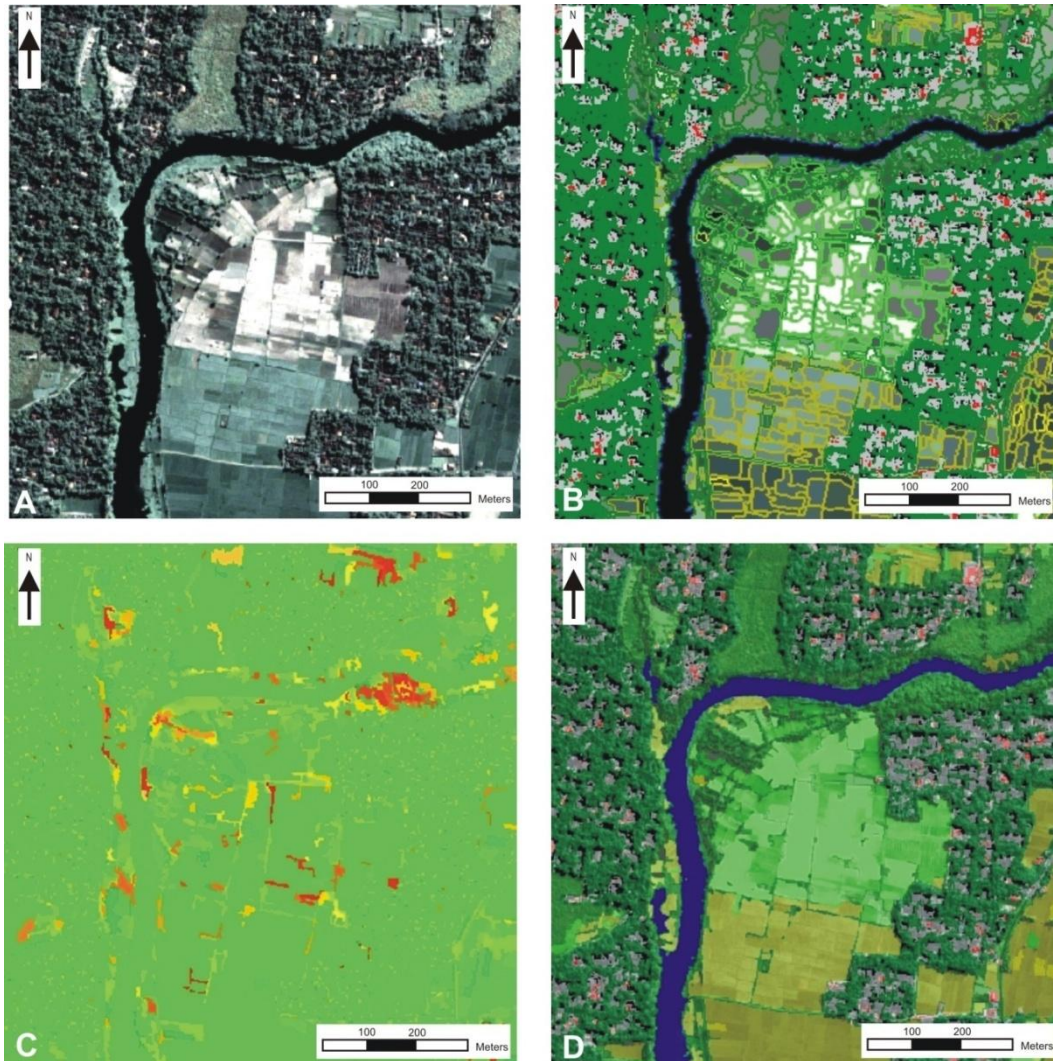


Figure 15: (A) Original Quickbird image (true colour), (B) Segmentation for Quickbird image (C) Classification Stability: The smaller Segments show lower Classification Stability (red segments), (D) Classification for Quickbird image.

## Land use detection from pre-event Quickbird image



Figure 16: Location of reference data sets for object-oriented accuracy assessment and manually digitized classes from pre-event, panchromatic Quickbird Imagery acquired 2003.

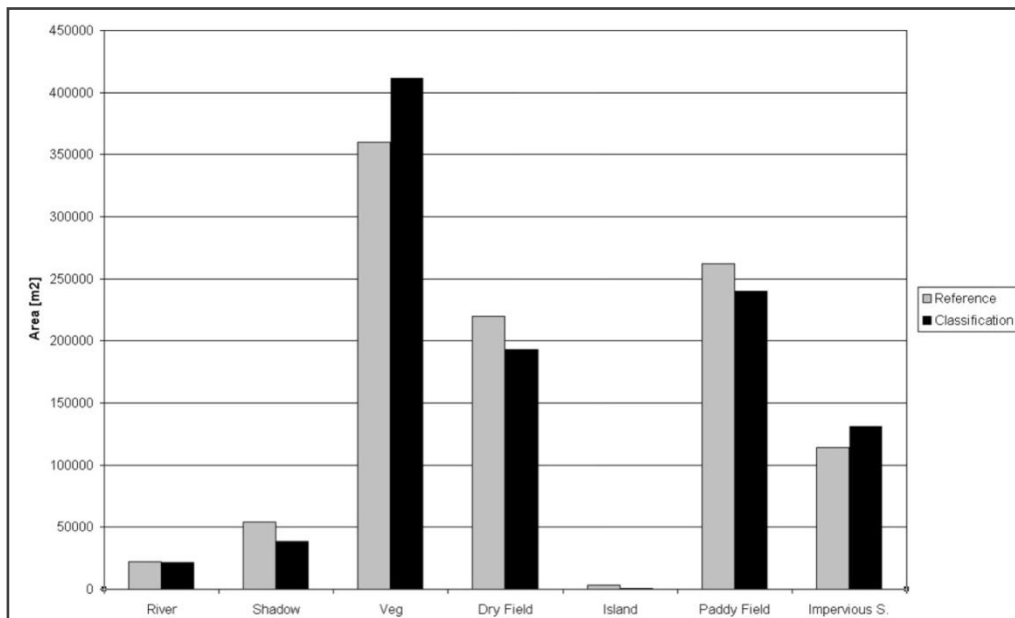


Figure 17: Diagram with surface percentage of all reference data sets compared to the classification results

Land use detection from pre-event Quickbird image

Table 9: Confusion matrix for land user / land cover classification using Quickbird images (2003) based on 10 reference datasets. The area of each land use class is shown in ha.

Reference / Classification	River	Shadow	Vegetation	Dry Field	Island	Paddy Field	Impervious surfaces	Total	User Accuracy
<b>River</b>	<b>19927,88</b>	231,59	292,47	0	282,93	0	1112,67	21847,54	0,91 %
<b>Shadow</b>	605,14	<b>22860,39</b>	7429,11	1603,26	44,64	148,35	5714,87	38405,76	0,59 %
<b>Vegetation</b>	1850,56	19063,06	<b>294166,04</b>	45456,56	2193,45	23317,44	25705,37	411752,48	0,71 %
<b>Dry Field</b>	29,75	1877,02	11567,37	<b>158349,14</b>	455,59	17860,76	2822	192961,631	0,82 %
<b>Island</b>	72,52	0	0	0	<b>195,67</b>	0	152,29	420,48	0,46 %
<b>Paddy Field</b>	0,15	910,68	9420,36	8800,02	0	<b>220595,65</b>	183,28	239910,14	0,92 %
<b>Built-up area</b>	0	9421,28	37176,46	5728,45	0	332,43	<b>78431,79</b>	131090,41	0,60 %
<b>Total</b>	22486	54364,02	360051,81	219937,43	3172,28	262254,63	114122,27	<b>1036389,44</b>	
<b>Producer Accuracy</b>	0,89 %	0,42 %	0,82 %	0,72 %	0,06 %	0,84 %	0,69 %		



## 6 Methodology Development

In this chapter, a methodology for developing earthquake risk maps based on correlations between building damage pattern and damage controlling parameters is presented. The proposed methodology is based on a non-quantitative approach using indicators to represent the considered parameters. The generated maps provide qualitative information on the spatial distribution of zones of high loss potential.

Preliminary to the risk map development, an analysis of the building damage distribution for different ground parameters is conducted to determine the correlations which form the basis for the weighting scheme of the indicators used in the hazard map generation. The risk map development methodology proposed in this study encompasses three steps: (1) Site specific assessment of earthquake-related hazards, (2) Assessment of buildings and population at risk, and (3) Assessment of earthquake risk.

### 6.1 Analysis of damage influencing indicators

In this section, the analysis of the building damage distribution and different ground parameters is presented (objective 5). The ground parameters used in this study are presented by the following indicators: (1) topsoil, (2) bedrock, (3) sediment thickness, (4) slope, (5) ground water depth, and (6) distance to epicentre. For each of the indicators, subcategories are defined and the normalized percentage of damaged buildings is calculated through the following steps: First, the urban area in each category is calculated based on the urban areas delineated from pre-event Quickbird image. Second, using the damage pattern extracted from the post-event image the percentage of urban damage within the urban areas is calculated. In addition to the individual analysis of the indicators, possible correlations between the indicators are analysed. In the final step, the categories of each indicator are weighted depending on the percentage of the urban damage.

#### 6.1.1 Damage distribution and soil type

In order to determine different topsoil categories for the study site, information available from 31 drilling profiles (Sir MacDonald & Partners, 1984) and from soil maps are combined (see Appendix I). From the drilling profile interpretation, four topsoil categories are defined: (1) No topsoil, (2) clayey topsoil, (3) sandy topsoil, and (4) sand and gravel. With an extent of 25,81 km<sup>2</sup>, sandy topsoil covers approx. 65 % of the study area and is quite uniformly distributed in the study area, whereas sand and gravel as recent fluvial deposits are mainly concentrated along river beds (see Figure 18). The analysis of the urban damage distribution within the different soil

## Methodology Development

categories reveals that most urban damage (11,85%) occurred in areas with clayey soil. It is interesting to observe that similar values were calculated for sandy soil (8,07 %) and sand and gravel (6,12 %). No urban damage was detected in areas with no topsoil. In the next step, the correlations between soil type and other indicators are analysed. For topsoil and ground water depth, the most damage is observed in areas with clayey topsoil and shallow ground water level (0 – 2,8 m). For a ground water depth range between 0 – 5,6 m, the percentage of urban damage is similar for clayey and sandy soil. For topsoil and slope the analysis reveals that 80,48 % of the urban areas located in flat areas (slope < 5°) with sandy topsoil are damaged in contrast to 11,71 % of the urban areas on clayey topsoil. The same can be observed for topsoil and bedrock (83,50 % for sandy topsoil and 12,18 % for clayey topsoil). For topsoil and sediment thickness, no distinct correlation can be determined. Based on these results, an index is assigned to each category. The categories for which the most urban damage was observed were assigned the highest index (see Table 10).

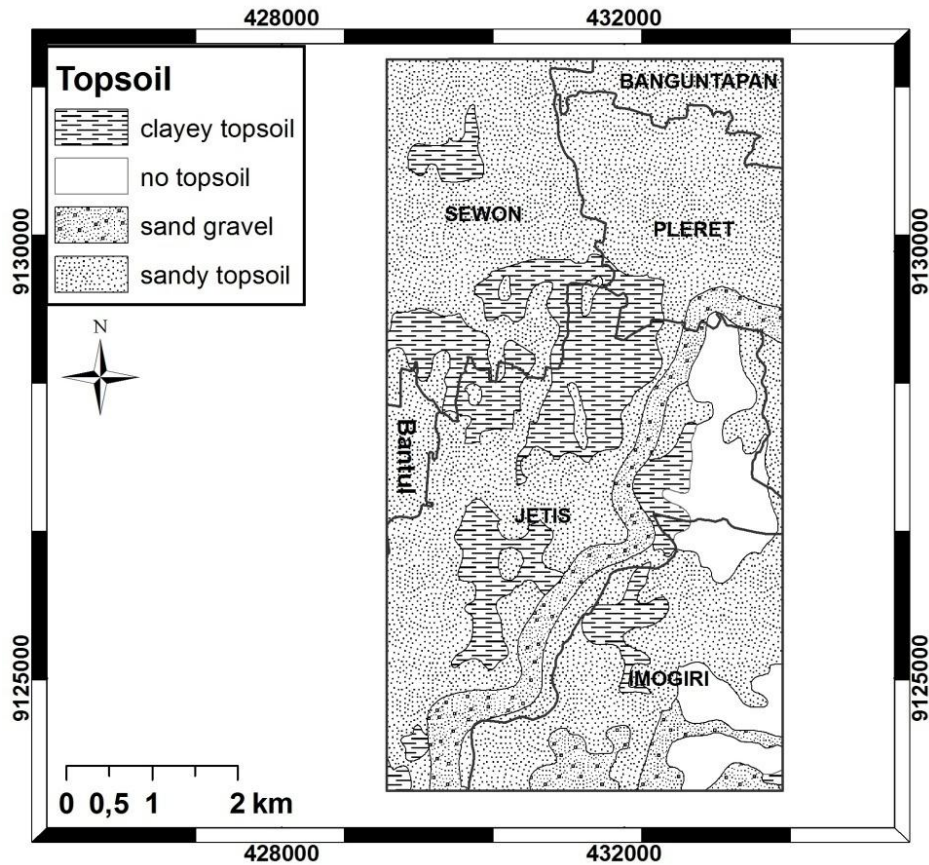


Figure 18: Soil map for the study area. The majority of the study area is covered by sandy topsoil

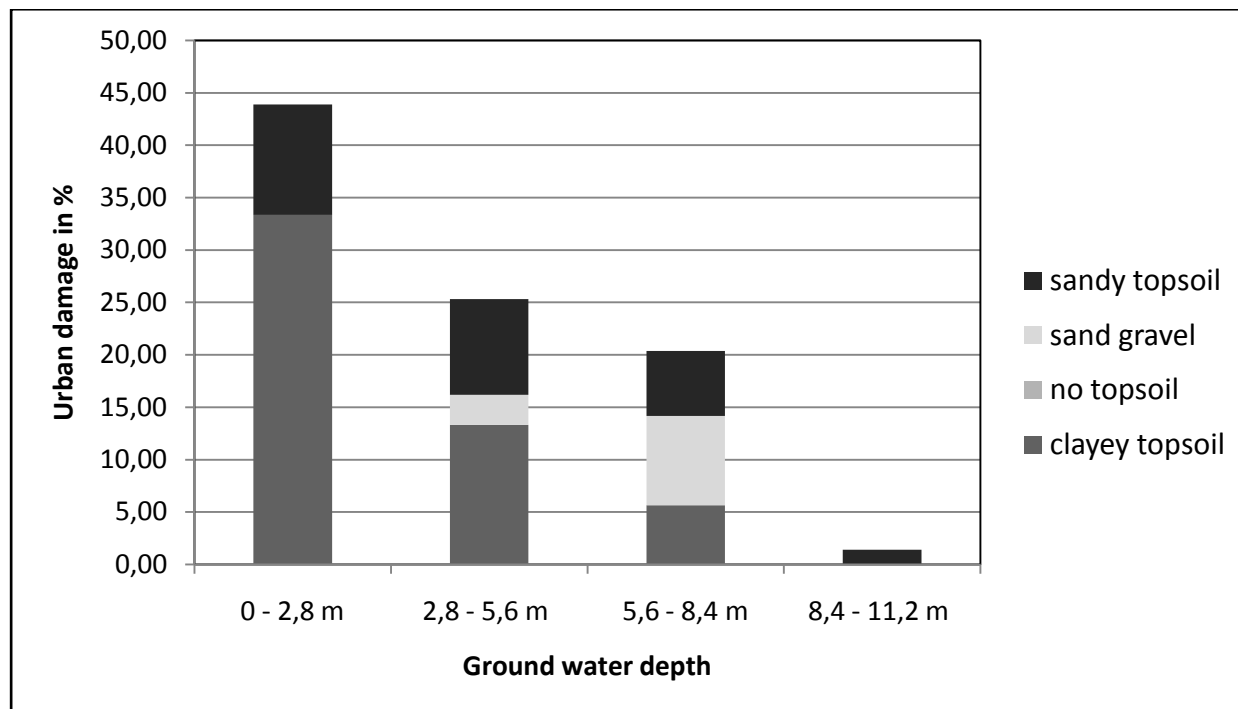


Figure 19: Distribution of urban damage as a function of topsoil and ground water depth. The most damage is observed in areas with clayey topsoil and shallow ground water depth. No damage was observed in areas with no topsoil and outcropping bedrock.

Table 10: Results of the analysis of urban damage distribution as a function of topsoil and index assigned to each topsoil category.

Topsoil category	Index
No topsoil	0,00
Sandy topsoil	0,31
Clayey topsoil	0,46
Sand and gravel	0,24

### 6.1.2 Damage distribution and bedrock / deposit age

The deposit age of the formation in the study area is determined from the geological map of Yogyakarta (Rahardjo et al., 1997). The oldest geological unit is formed of the deposits of the early Miocene Semilir Formation, followed by the middle Miocene Nglanggran Formation. The Semilir Formation is build up of interbedded breccias, shales and tuffs with a thickness up to 1200 m. The Nglanggran Formation consists of agglomerates and tuffs, which exceed 750 m in the

## Methodology Development

---

Kali Oyo catchment. The youngest, Tertiary formation consists of Wonosari limestones which covers a very small areal in the south of the study areas. Quaternary deposits encompass the widespread, unconsolidated sediments deposited south of the foothills of Mount Merapi (Yogyakarta and Sleman Formation) and fluvial sand and gravel deposits along small rivers of the surrounding mountains flow into an anabranch of the Oyo River. For the study area bore hole data are available from a drilling campaign carried out by Sir MacDonald and Partners in 1984. Using the drilling profile, the following categories are defined based on the geotechnical properties of the formations: (1) Tertiary volcanoclastic rocks, (2) Quaternary sediments, and (3) Quaternary alluvium (see Figure 20 for a geological map of the study area).

The analysis shows that the most buildings were damaged in areas with Quaternary sediments. This is comprehensible as damaging soil amplification and liquefaction effects are more likely to occur in unconsolidated sediments than in stiff, volcanoclastic rocks. From the analysis it becomes obvious that 8,69 % of the urban areas in Quaternary sediments were damaged, whereas almost no damage was observed in Tertiary volcanoclastic rocks and Quaternary alluvium. The small percentage of damage in the tertiary volcanoclastic rocks, less than 1°, can be explained by the advanced consolidation of formations and the shallow terrain which hinders the formation of earthquake induced landslides and rock falls. Among the Tertiary rocks, the high percentage of urban damage occurred in the series of andesitic volcanic breccias and flow deposits of the Nglanggran Formation which is a product of a submarine rubble flow, caused by slumps on early Miocene andesitic volcanoes (Smyth et al., 2008). In contrast, no damage was observed in the limestone of the Wonosari Formation. The next step comprises the analysis of correlations between the individual indicators.

The analysis for bedrock and slope shows that the 8,6 % of the urban areas were damaged in flat (slope < 5°) areas with quaternary sediments and only 0,59 % in areas with moderate slope (> 5°). For bedrock and soil type, the analysis revealed that no damage occurred in areas with no topsoil cover independent from the bedrock type. In areas with topsoil cover, 12,18 % of the urban areas were damaged with clayey soil, followed by 8,33 % in areas with sandy soil. Considering sediment thickness and bedrock, it becomes obvious that the thickness of the sediment had no influence on the damage distribution. The combination of bedrock and ground water depth revealed that the most urban areas were damaged in areas with quaternary sediments and a the ground water depth range between 8,4 – 11,2m. The results of the analysis form the basis for the indexing of the categories (see Table 11).

Table 11: Results of analysis of urban damage distribution as a function of bedrock and assigned index to each bedrock category

<b>Bedrock category</b>	<b>Index</b>
Tertiary volcanoclastic rocks	0,11
Quaternary sediments	0,53
Quaternary alluvium	0,36

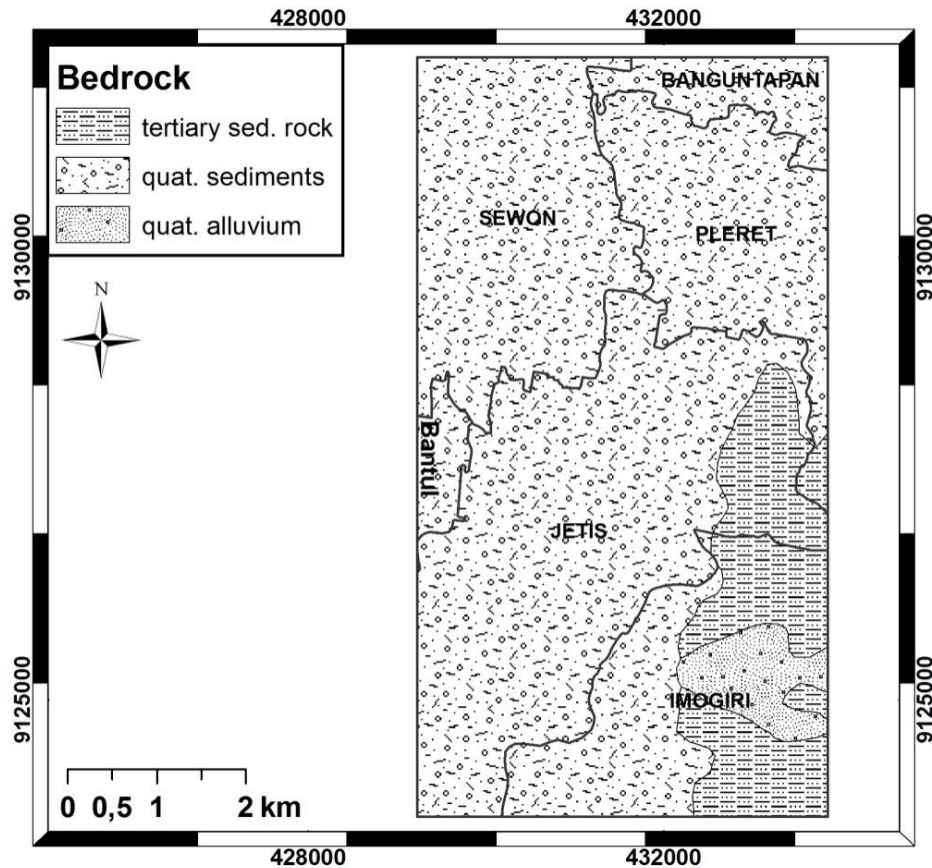


Figure 20: Geological map of the study area. The Quaternary sediments are the dominate bedrock formation.

### 6.1.3 Damage distribution and sediment thickness

The sediment depth or depth to bedrock is interpolated using a krigging algorithm and information on sediment thickness from the 31 drilling profiles (Sir MacDonald & Partners, 1984). Within the study area, the interpolated depth ranges from 24 to 60m. Using an equal interval algorithm, three depth categories are defined (see Table 12). Figure 21 shows the distribution of sediment thickness for urban damage. It is interesting to observe that the percentage of urban damage does not show any explicit correlation with sediment thickness. This is also true for the combination of sediment thickness and bedrock. Combining sediment thickness and slope, it becomes obvious that more than 75% of the urban damage occurred in the flat areas (slope <math> < 5^\circ </math>) and that the sediment thickness has no influence. For the influence of ground water depth it can be observed that in the range between 0 – 2,8m only damage occurred in areas with thickest sediment layer (48 – 60m) whereas no damage occurred in areas with smaller sediment thickness.

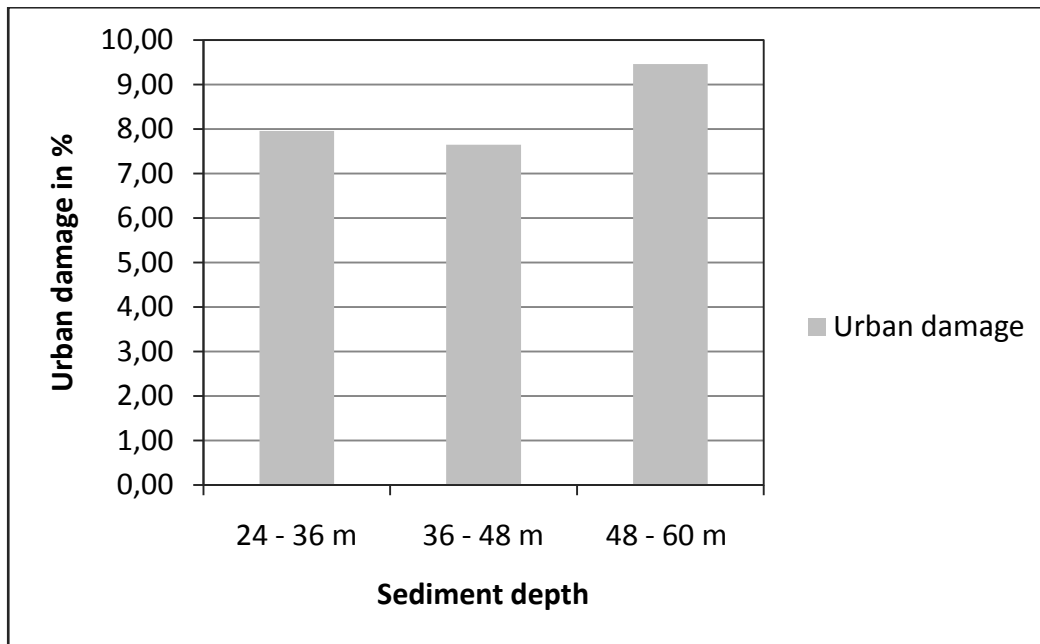


Figure 21: Distribution of urban damage as a function of sediment thickness. No distinct correlation between urban damage and sediment thickness can be observed.

Table 12: Results of analysis of urban damage distribution as a function of sediment depth and index assigned to each category.

Sediment depth (m)	Index
24 – 36	0,32
36 – 48	0,31
48 – 60	0,38

#### 6.1.4 Damage distribution and ground water level

Water table depth information is obtained for 31 drilling profiles available from Sir McDonald and Partners (1984). Using a krigging technique, the water table is interpolated for the study area. The resulting values range from 0,5m to 11,2m and are subdivided using equal breaks into 4 categories: (1) 0 – 2,8 m; (2) 2,8 – 5,6 m; (3) 5,6 – 8,4m; and (4) 8,4 – 11,2 m. The analysis reveals that highest percentage of damaged urban areas correlates with the most shallow ground-water level category. It is obvious that the percentage of urban damage is decreasing with increasing ground water level. In Table 13, the results of the analysis of the urban damage distribution and the assigned indices are listed. The correlations between ground water level and other factors are discussed in the above sections.

Table 13: Results of analysis of urban damage distribution as a function of ground-water level and index assigned to each category.

Ground water level (m)	Index
0,0 – 2,8	0,41
2,8 – 5,6	0,35
5,6 – 8,4	0,22
8,4 – 11,2	0,02

### 6.1.5 Damage distribution and slope

The slope is calculated based on a DEM with a cell size of 27 m (kindly provided by Achim Roth from the German Aerospace Centre). The slope is subdivided into two categories: (1) slope  $> 5^\circ$  and (2) slope  $< 5^\circ$ . The analysis revealed that four times more urban damage occurred in shallow areas than in slope  $< 5^\circ$  areas (see

Figure 22). From the combination of topsoil and slope, it becomes obvious that nine times more damage occurred in flat areas than in areas with moderate slope, independently of the soil type. However, in flat areas 80% of the urban areas were damage in sandy topsoil areas.

Table 14: Results of analysis of urban damage distribution as a function of slope and index assigned to each category.

Slope ( $^\circ$ )	Index
$> 5$	0,20
$< 5$	0,80

### 6.1.6 Damage distribution and distance to epicentre

The damage distribution is analysed as a function of distance from the epicentre. Harvard CMT epicentre coordinates are used as point information. The distance between epicentre and building damage is calculated using a buffer of one kilometre extending outward from the epicentre. No distinct correlation is observed from the urban damage distribution as a function of distance to epicentre. The most urban damage is observed in areas with a distance of 25 – 26 km and 28 – 29km distance from the epicentre. However, a distinct correlation is not observed (see Figure 23). This shows that the occurrence of urban damage is independent of the distance to the epicentre in this very small distance range (19 – 29 km). Table 15 lists the percentage of urban damage is each distance category and the assigned indices.

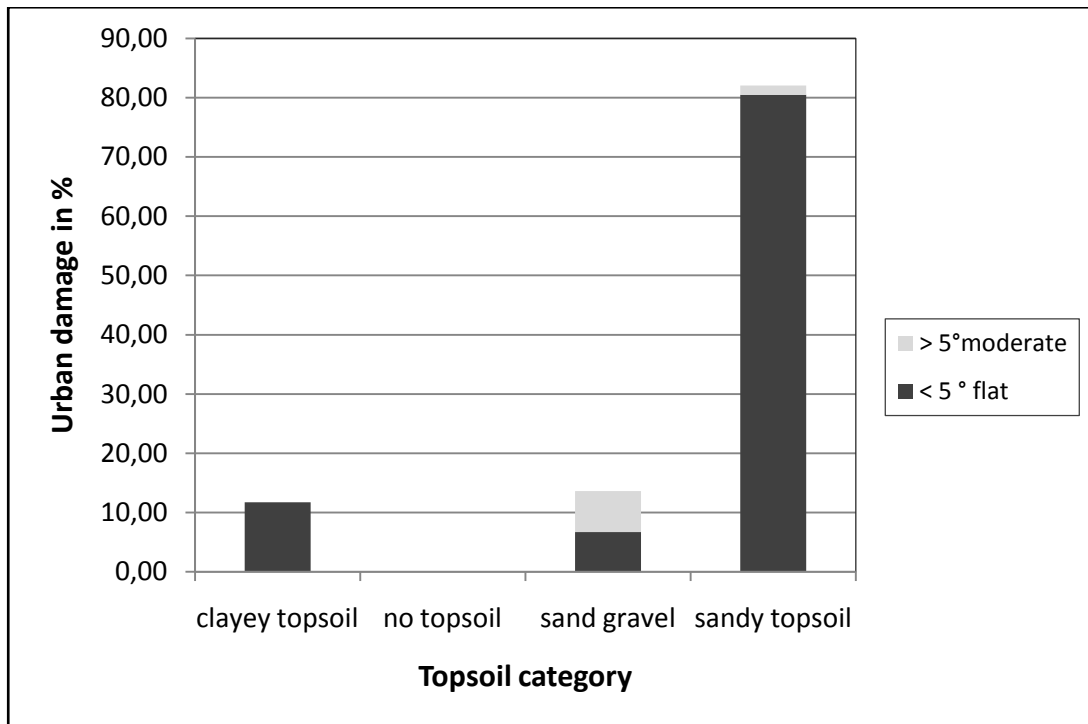


Figure 22: Distribution of urban damage as a function of slope and topsoil. The most damage occurred in areas with slope < 5° and sandy topsoil.

Table 15: Results of analysis of urban damage distribution as a function of distance to epicentre and index assigned to each category.

Distance to epicentre (km)	Index
19 – 20	0,0
20 – 21	0,10
21 – 22	0,10
22 – 23	0,11
23 – 24	0,05
24 – 25	0,05
25 – 26	0,17
26 – 27	0,13
27 – 28	0,11
28 – 29	0,18

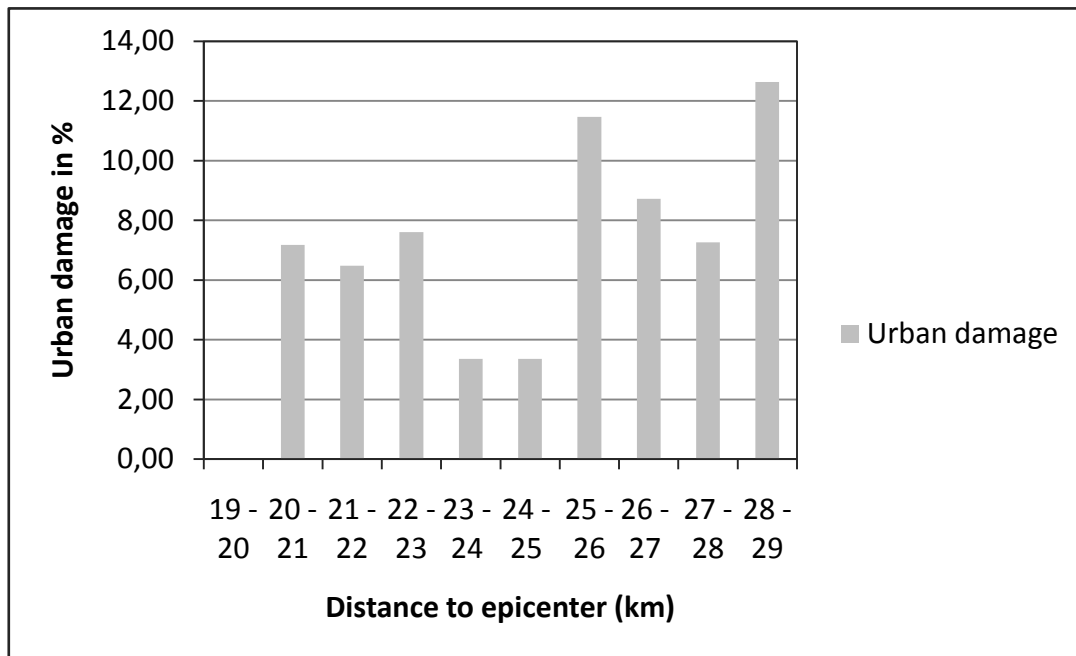


Figure 23: Distribution of urban damage as a function of distance to epicentre. The distribution of urban damage revealed no distinct correlation.

## 6.2 Site specific assessment of earthquake-related hazards

The earthquake-related hazards assessed in this study are selected considering the topography and morphology of the study site. The study area is located south of the foothills of Mount Merapi on plain terrain. Only in the very western part, the foothills of the Wonosari Karst Plateau form moderate slopes. Due to this morphology, landslides and rock falls triggered by ground shaking do not form the most imminent, earthquake-related threat. Instead the wide spread, unconsolidated sediments, the shallow ground water table and plain terrain indicate that liquefaction and ground shaking amplification are the primary earthquake-related hazards. In this section, the factors that influence the susceptibility for liquefaction and ground shaking amplification are combined to develop liquefaction and amplification hazard maps (objective 6).

## 6.3 Development of liquefaction susceptibility map

The devastating effects of earthquake induced liquefaction have been observed in various past earthquakes. In 1964 widespread liquefaction was induced by the Great Alaska earthquake and forced buildings to settle and tilt (Seed & Wilson, 1973). According to Youd and Perkins (1978), more than 50 % of the damage was caused by liquefaction induced ground failure. Another example of the destructive power of liquefaction is the 1964 Niigata (Japan) earthquake. Severe

damage was observed to be limited to buildings that were founded on top of loose, saturated soil deposits, more than 250 highways and bridges were damaged beyond repair (Kawasumi-Hiroshi, 1968). During the more recent 1995 Kobe (Japan) earthquake, liquefaction was one of the major causes for damage to lifeline and pile foundations of buildings and bridge along the Kobe shoreline (Hamada et al., 1995; Matsui & Oda, 1996). Building damage due to liquefaction has also been reported from the 1989 Loma Prieta (USA) and 1994 Northridge earthquake (USA). A comprehensive list of documented case histories of liquefaction induced by earthquake can be found in Bardet (2003). The above examples illustrate the devastating impact of liquefaction during earthquakes. However, liquefaction does not occur randomly but is restricted to certain geologic and hydrologic environments, primarily recently deposited sands and silts in area with high ground water table (Youd, 1992). The liquefaction susceptibility of a material strongly depends on the geological properties, the age of the deposit and the ground water level, thus on the local environment. In general, the younger and looser the sediment and the higher the water table, the more susceptible is a soil to liquefaction (Hays, 1981). Soils deposited prior to the Holocene epoch (more than 10,000 years) are usually not prone to liquefaction (Youd & Perkins, 1978). Liquefaction susceptibility refers to the capacity of the soil to resist liquefaction (EERI, 2006). Unlike liquefaction potential, the probability of earthquake ground shaking is not considered. Ratings for liquefaction susceptibility have been suggested by various authors (Youd & Perkins, 1978; Liao, Veneziano & Whitmann, 1988).

In the following, a methodology for mapping the liquefaction susceptibility based on qualitative indicators is presented. Liquefaction susceptibility maps provide a regional depiction of the hazard using five ratings (very high to very low). As discussed in the above section, there are three main factors controlling the liquefaction susceptibility of an area: (1) Depths to ground water level, (2) Geologic properties of the deposit, and (3) Topsoil type. Table 16 lists the considered factors, the defined categories and the assigned weights. The weighted factors are combined to generate a liquefaction susceptibility map using an overlay function (see Figure 24). The majority of the study area (46,06 %) has a high liquefaction potential due to the wide spread young volcanic deposits and the shallow ground water table (see Table 17). Saturated, sandy soils and recent sediment lead to very high susceptibility in some eastern parts of the study area. The areas of low to very low susceptibility are concentrated in the south-east of the study area with outcropping bedrock and a deeper ground water level.

Table 16: Liquefaction susceptibility controlling factors and weighted categories based on the analysis of urban damage distribution.

<b>Factor</b>	<b>Categories</b>	<b>Weight</b>
Bedrock	Tertiary volcanoclastic rocks	0,11
	Quaternary sediments	0,53
	Quaternary alluvium	0,36
Soil type	No topsoil	0,00
	Sandy topsoil	0,31
	Clayey topsoil	0,46
	Sand & gravel	0,24
Ground-water depth	0,0 – 2,8m	0,41
	2,8 – 5,6m	0,35
	5,6 – 8,4m	0,22
	8,4 – 11,2 m	0,02

Table 17: Liquefaction susceptibility raking with 5 classes.

<b>Susceptibility Class</b>	<b>Area (km<sup>2</sup>)</b>	<b>Area (%)</b>
Very low	3,84	9,69
Low	3,12	7,78
Moderate	18,29	46,06
High	12,37	31,21
Very high	2,05	5,17

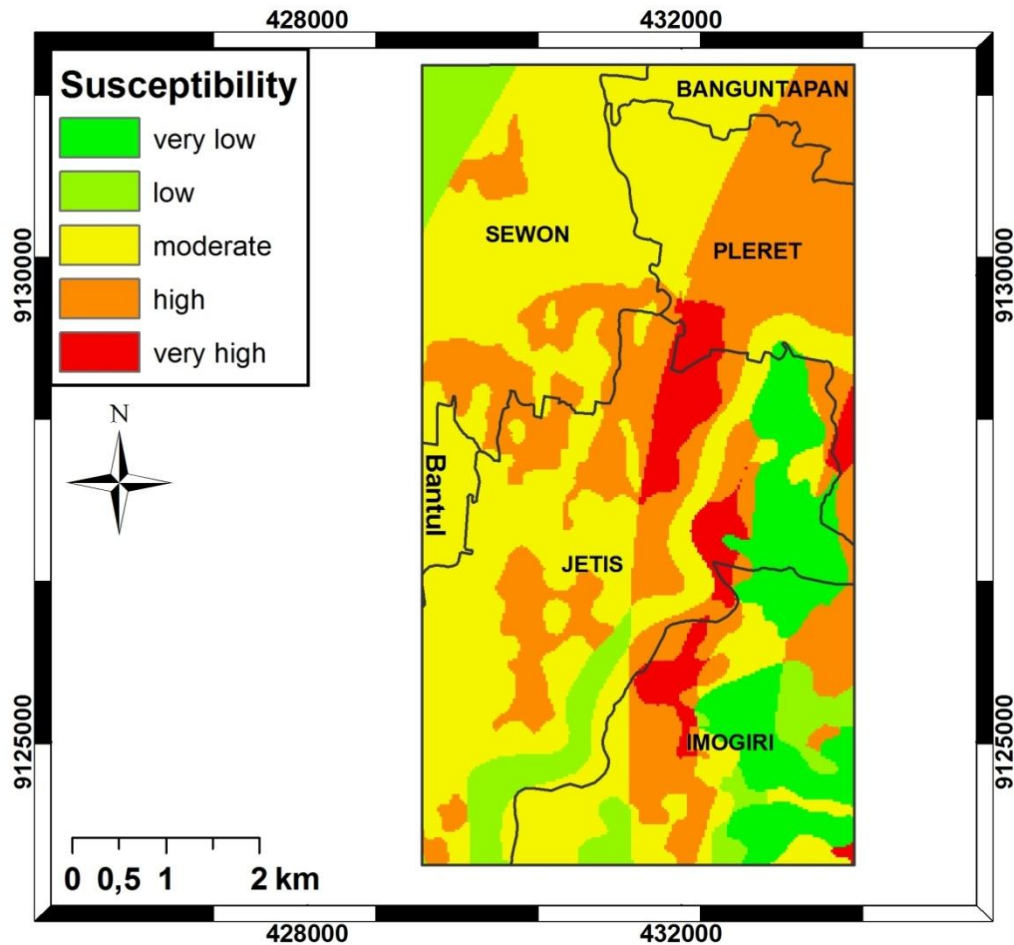


Figure 24: Liquefaction susceptibility map of the study area. With 46,06 % the majority of the study areas exhibits a moderate liquefaction susceptibility. About 31 % of the study areas exhibit high liquefaction susceptibility.

#### 6.4 Development of amplification susceptibility map

It has been frequently observed that earthquake damage is greater in settlements sited on soft soils than in those sited on stiff soils or on rock sites. For example, in 1985 Mexico City was hit by an 8.1M earthquake in which strong amplification due to extremely soft clay layers caused high-rise buildings to collapse despite their long distance from the source (Kawase, 2003). Another striking example of amplification of ground motion at sites with thick soil deposits is the 1989 Loma Prieta earthquake in which much of the damage occurred in the central San Francisco Bay area at sites underlain by thick deposits of soft clayey soils (Stewart, 1997).

As soil types and thickness, and to a lesser extent rock, vary widely from site to site in a region and worldwide, many different ways of classifying sites with respect to amplification exist. Although knowledge of site response to earthquake has grown over the last years, still no common agreement has been reached on how sites should be classified for earthquake hazard purposes. A comprehensive discussion on problems associated with soil classification for site effects can be found in Aki (1988). Usually, site-specific soil conditions are described in crude terms through broad classification such as rock / stiff soil, deep soil, and soft soil. The Unified Building Code (UBC) site classification is a qualitative scheme based on descriptive soil conditions which differentiates four soil types. Campell (1981) presented a geological classification scheme which subdivides the two main categories of soil and rock into 4 soil categories (shallow soil, soft soil, firm soil and very firm soil) and 2 rock categories (primarily sedimentary and primarily crystalline rock). In contrast to qualitative classification schemes, the model of Boore et al. (1997) constitutes an exception to the generalizing classification trend, since it takes into account the average shear wave velocity ( $V_s$ ) to a depth of 30m (Brandes, 2003). Based on different threshold for  $V_s$ , the National Earthquake Hazard Reduction Program (NEHRP) provides a classification system for characterizing sites for purposes of estimation amplification of seismic motions. As  $V_s$  data are not always available, alternative parameters are suggested such as standard penetration resistance for cohesionless soil and average undrained shear strength for clayey soil. In total, the NEHRP classification distinguishes six site classes. The  $V_s$  was adopted as a primary basis for site classification by 2000 International Building Code (IBC), the follower of the original UBC (Campell, 2003). Another important factor is distance to bedrock or sediment depth which is the depth to basement rock beneath the site. Sediment depth has been introduced by Trifunca and Lee (1979) and used in a number of studies by various authors (Field 2000; Lee & Anderson, 2000).

In this study, a soil classification based on qualitative description is applied. Three factors were considered for assessing the soil amplification susceptibility: (1) Sediment depth, (2) Topsoil, and (3) Bedrock. The amplification susceptibility map is developed by conducting an overlay analysis using the factors weighted based on the analysis in section 6.1 (see Table 18). Figure 25 displays the results of the overlay analysis. The areas with low to very low susceptibility for soil amplification are located in the south-eastern part of the study area. The widespread unconsolidated sediments in the north-western part in combination with great sediment thickness lead to a high to very high susceptibility. The analysis of the five susceptibility classes reveals the 45% of the study area is exposed to high soil amplification susceptibility (see Table 19).

## Methodology Development

---

Table 18: Ground amplification susceptibility controlling factors and weighted categories based on the analysis of urban damage distribution.

<b>Factor</b>	<b>Categories</b>	<b>Weight</b>
Bedrock	Tertiary volcanoclastic rocks	0,11
	Quaternary sediments	0,53
	Quaternary alluvium	0,36
Soil Type	No topsoil	0,00
	Sandy topsoil	0,31
	Clayey topsoil	0,46
	Sand & Gravel	0,24
Sediment thickness	24 - 36 (m)	0,32
	36 - 48 (m)	0,31
	48 - 60 (m)	0,38

Table 19: Ground amplification susceptibility raking using 5 classes. The majority of the study area exhibits a high to very high susceptibility.

<b>Susceptibility Class</b>	<b>Area (km<sup>2</sup>)</b>	<b>Area (%)</b>
Very low	4,41	11,13
Low	3,62	9,13
Moderate	5,16	13,02
High	17,95	45,28
Very high	8,50	21,44

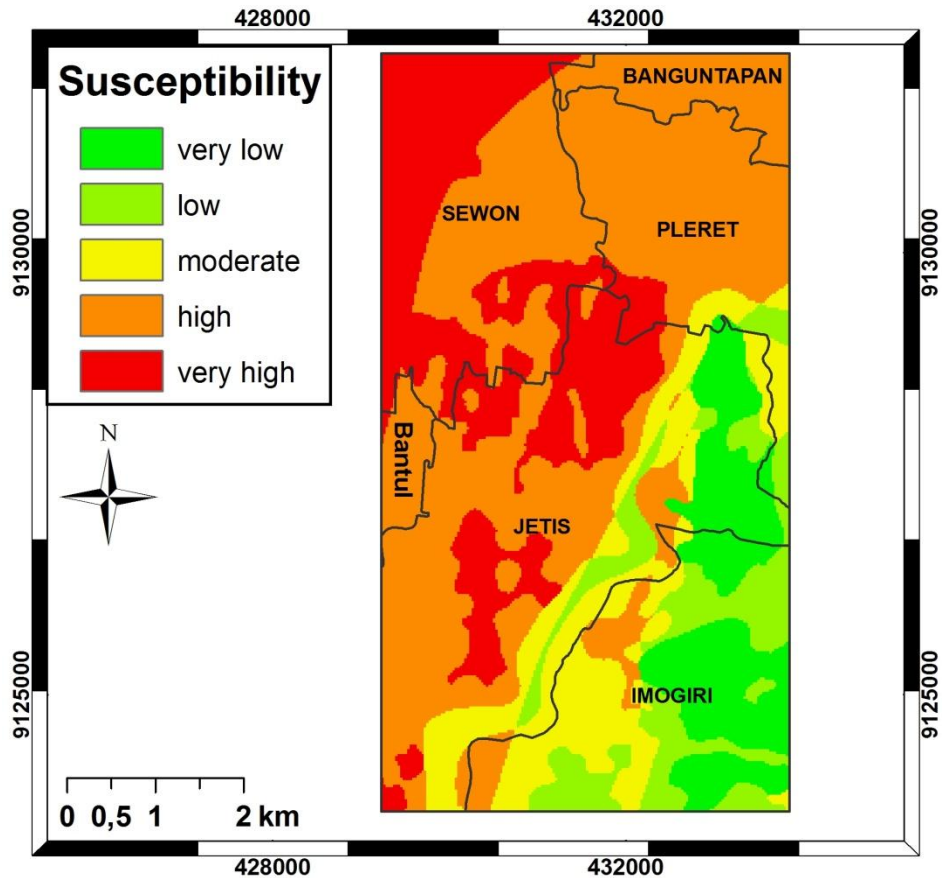


Figure 25: Ground amplification susceptibility map. Large parts of the north-western part of the study area exhibit a high to very high susceptibility.

## 6.5 Hotspot analysis

In this section an overlay analysis is conducted to identify areas prone to liquefaction and soil amplification. Figure 26 displays the resulting hotspot map. In general, the hotspots are concentrated on the north-western part and in the middle of the study area. This is due to the very high liquefaction susceptibility of the young volcanic deposits combined with sandy soil cover and shallow ground water level. The missing top soil cover and the outcropping bedrock in the south-western part – mostly in the district Imogiri - lead to low susceptibility.

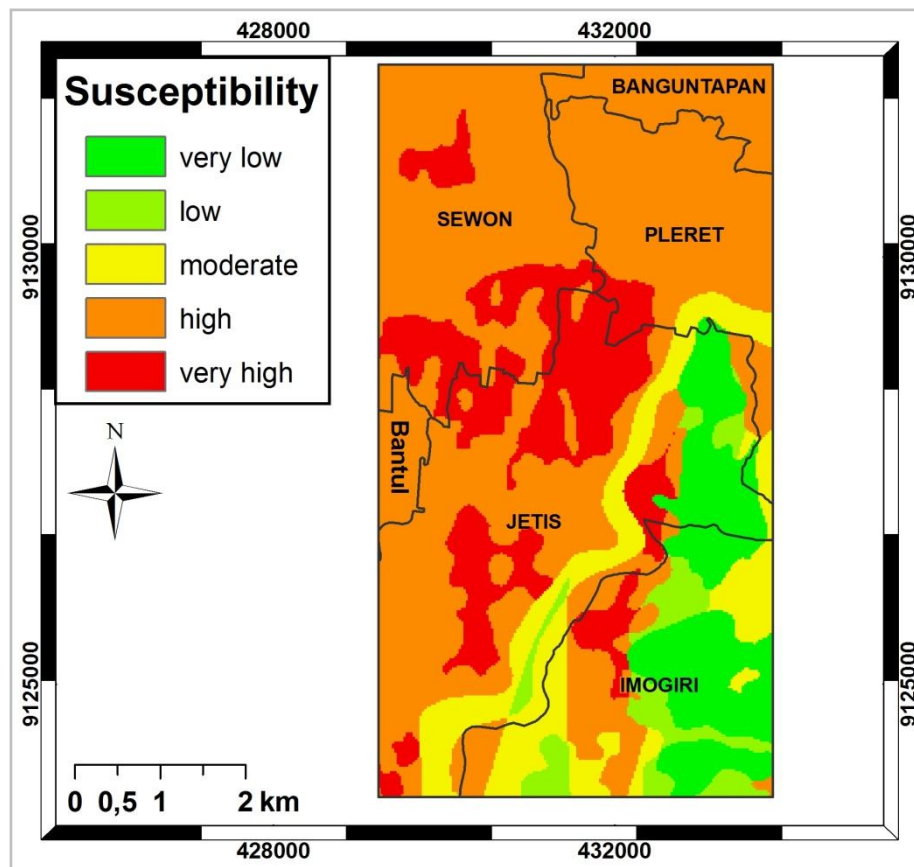


Figure 26: Hotspot map for ground amplification and liquefaction. The areas with the highest susceptibility are located in the north-western part due to the shallow ground water level and unconsolidated sediments.

## 6.6 Exposure Assessment

In this study, the considered assets at risk are limited to residential buildings and population density (objective 7). There are two major reasons for this decision. First, the majority of people are killed or seriously injured due to collapsing buildings. Second, only building damage is extracted from the satellite image. In consequence, only residential buildings identified as built-up areas from Quickbird images are included in the exposure map.

### 6.6.1 Residential buildings

A study published by Blaß and Fellmoser in 2007 on the region of Yogyakarta showed that there are two major building classes in the study area: engineered and non-engineered buildings. Engineered buildings are multi-storey buildings made of reinforced concrete or steel. Engineered buildings are mainly found in municipal areas. For example, many official buildings are engineered buildings. Non-engineered buildings are the dominant building class in rural areas. These buildings normally have one or two storeys. The houses are a mixed forms of reinforced concrete, masonry and wooden roof constructions (see Figure 27). The roof is made of heavy roof tiles and the reinforced concrete columns and masonry are weak compared to the tiles (Blaß & Fellmoser, 2007). Brüstle et al. (2007) point out that poor building material is mostly found in rural areas, whereas higher quality material is used in urban areas. From a visual inspection of the pre-event Quickbird image and from additional information documented on the study area, it is concluded that the majority for residential building in the study area are non-engineered buildings. Geo-coded information on residential buildings available for the study site is of unknown quality and accuracy. Therefore, the built-up areas are extracted from the pre-event satellite image (see chapter 5).



Figure 27: (Left) Destroyed building near Bantul. (Right) Collapsed building (masonry / reinforced concrete) in Bangunharjo. The images were taken by the taskforce of the German Society for Earthquake Engineering and Building Dynamics (DGEB).

### 6.6.2 Population density

The information on population density is provided on district level and ranges between 500 and 3500 inhabitants / km<sup>2</sup>. The highest population density with 2500 to 3500 people is documented

for the district of Sewon, whereas the districts Pleret and Imogiri show the scarcest population. Since there was no information on the population structure available, all inhabitants within a district had to be assumed equally vulnerable but the denser populated districts were assumed to be more vulnerable.

### 6.6.3 Exposure Map

For generating the exposure map, the following assets are incorporated: residential buildings and the population density, which are weighted by their vulnerability. In general, it can be assumed that the vulnerability is increasing with increasing population density. Therefore, the sub-districts with the highest population density are assigned the highest weight. In order to emphasise the potential for improvement of land use data sets using remote sensing, both data sets (pre-existing land use and improved land use) are separately considered in the overlay analysis and the resulting exposure maps are compared. In both data sets, the residential areas are weighted highest (for the generation of the land use data set see chapter 5). The assigned weights for the exposure are listed in Table 20.

Table 20: Assets at risk used for the exposure map development. The residential areas are weighted highest in the land use data set.

<b>Land use classes</b>	<b>Weights</b>
Paddy field	0,6
Dry field	0,5
Vegetation	0,2
River	0,1
Built-up areas	1,0
Shadow	0,1
<b>Population Density (people / km<sup>2</sup>)</b>	
3500 - 2500	1,0
2500 – 1500	0,7
1500 - 500	0,5

#### 6.6.4 Result for Exposure Assessment

In order to compare the exposure maps based on the pre-existing land use and the remotely-generated land use, the spatial distribution of the vulnerability within the study area is shown in Figure 28. Both maps reveal that the elements at risk in the north-west of the study are characterized by a higher vulnerability due to highest population density whereas the south-east is characterized by a lower vulnerability due to the lowest population density and the lower percentage of residential areas respectively. The residential areas are of vital importance for assessing the exposure. Therefore, residential areas extracted from remote sensing and residential areas from the pre-existing data set are compared. It is evident that the remotely-sensed built-up areas give a more realistic picture of the distribution of the built structures and thus, lead to a realistic exposure (see Figure 28). For the study area, 6,3 km<sup>2</sup> were delineated as residential from satellite imagery and 17,58 km<sup>2</sup> were manually digitized. This great difference is caused by the vegetation and bare ground with is included in the residential polygon but not included using remote sensing (see Figure 29).

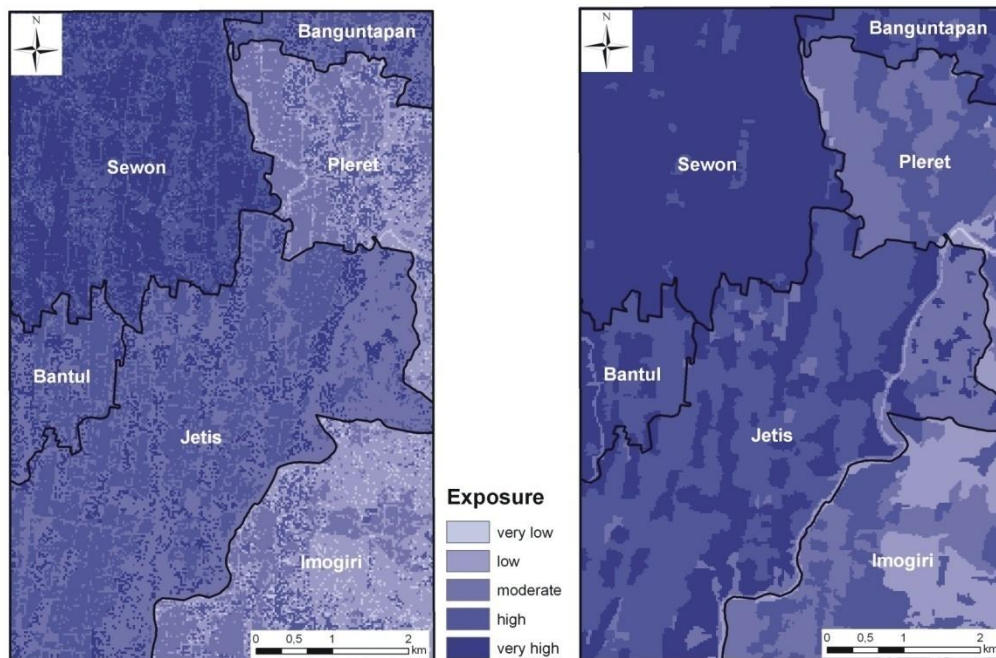


Figure 28: Exposure map of study area including residential areas and population density. (Right) Exposure map based on manually digitized residential areas, (Left) exposure map based on remotely sensed residential areas.

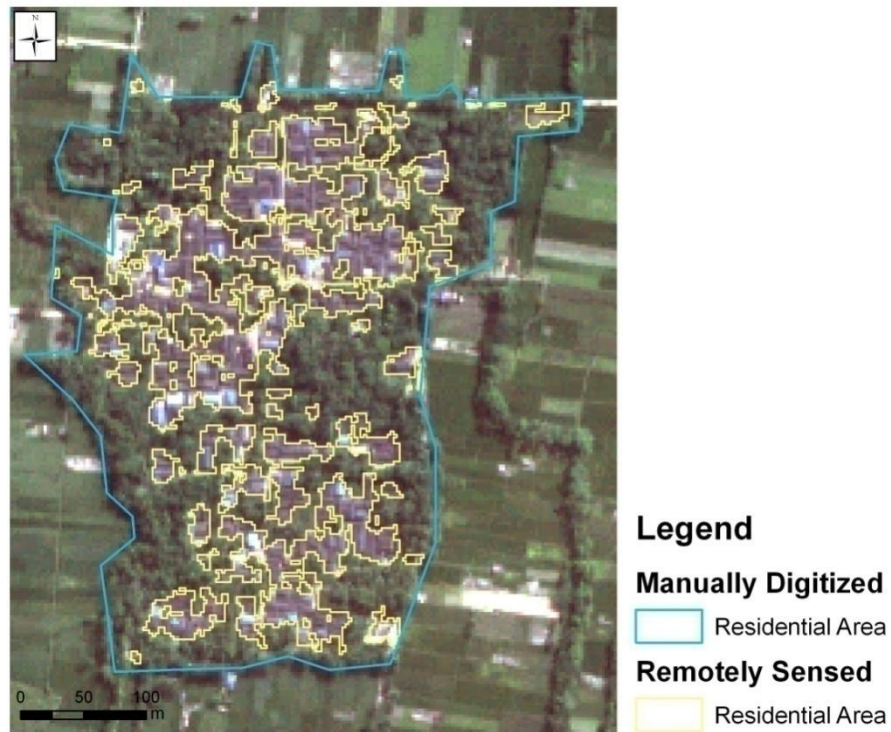


Figure 29: Comparison of residential areas delineated from satellite imagery (yellow) and manually digitized (blue). Note that the blue polygon does not only include buildings but also vegetation and bare soil, where the yellow polygons only include built structures.

### 6.7 Risk Assessment

The earthquake risk map is developed through a combination of the hazard and exposure map (objective 8). Figure 30 shows the risk map of the study area. It displays the spatial distribution of the classified results of the risk assessment, five risk classes ranging from very low to very high. From visual interpretation it is noticeable, that there is a great percentage of high risk areas in the north-western part of the study area (subdistrict Sewon). Sewon is the most densely populated sub-district of Bantul with a population density of 2500 - 3500 people per km<sup>2</sup>. Furthermore, the geological conditions of very thick unconsolidated sediments of the young volcanic deposits of the Mount Merapi (a drilling in the east of Sewon revealed a sedimentary thickness of 120 m (Sir MacDonald & Partners, 1984)) are favourable for the susceptibility to soil amplification and liquefaction. The sub-districts of Banguntapan, Bantul and Jetis have the same population density. According to the geological map (Rahardjo et al., 1997), the bedrock geology is similar in these three sub-districts. But the drilling profiles show that the thickness of the unconsolidated sediment is gradually decreasing towards the south and therefore the soil amplification hazard

decreases as well. The very low to low risk classes within the sub-district Imogiri can be explained by the local, geological conditions and the deep ground water level. The bedrock mainly consists of limestone and the soft sedimentary cover with approx. 35 m (Well E27) is thin compared to Sewon. In combination with a low population density this leads to the low risk for Imogiri.

Comparing the risk maps display in Figure 30, it becomes obvious that using built-up areas instead of residential polygons allows for a disaggregation of the risk. A more realistic picture of the areas at risk is displayed because only built-up areas are included.

Table 21 and

Table 22 list the distribution of the risk zones calculated from the risk maps display in Figure 30. Both display the same trend for the very low risk zone covering the smallest part of the study area. However, the exposure map based on the manually digitized residential polygon includes more than twice the area than the remotely-sensed residential areas, the corresponding risk zone distribution displays significant difference for the moderate and high risk zones.

Table 21: Distribution of risk zones using remotely-sensed built-up areas.

<b>Risk zone</b>	<b>Area (km<sup>2</sup>)</b>	<b>Area (%)</b>
Very low	3,54	8,96
Low	6,09	15,41
Moderate	9,17	23,20
High	10,76	27,23
Very high	9,96	25,2

Table 22: Distribution of risk zones using manually digitized residential polygons.

<b>Risk zone</b>	<b>Area (km<sup>2</sup>)</b>	<b>%</b>
Very low	2,97	7,52
Low	5,08	12,85
Moderate	11,34	28,69
High	13,52	34,21
Very high	6,61	16,73

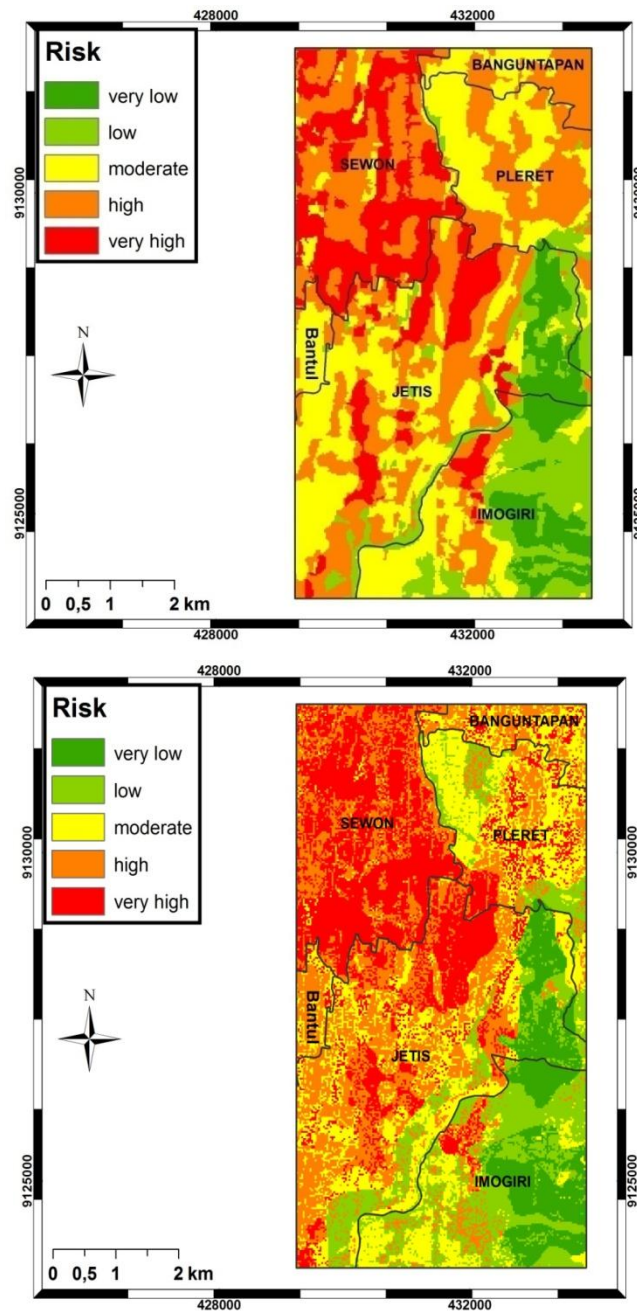


Figure 30: Risk map for building damage (upper figure) using manually digitized residential polygons and (lower figure) using remotely-sensing built-up areas. The zones with very high risk are mainly concentrated in the north-western part of the study area. The south-eastern part exhibits a significantly lower risk to earthquake-related building damage. The comparison reveals the generalizing effect of residential polygons. Using remotely-sensed built-up area a large degree of detail can be displayed.

# 7 Discussion and Conclusion

The overarching goal of this study was to demonstrate that earthquake risk maps can be developed by combining building damage distribution extracted from post-event satellite image and qualitative indicators describing damage influencing factors. Very-high resolution satellite Quickbird images were used for the building damage assessment and for improving pre-existing land use data. The case study for the May 2006 Yogyakarta earthquake demonstrated that using building damage from previous earthquakes a weighting scheme for damage influencing factors can be developed and applied for developing a building damage risk map.

## 7.1 Discussion

The first objective of this study was to provide a consistent terminology for the risk map development. In chapter 2.12.1, the disaster – related definitions used were introduced. Not taking site effects into account and with no local faults considered to be capable of a larger seismic event, on a small scale the seismic hazard is assumed to be uniform. This underlying, probabilistic hazard is differentiated by local ground conditions such as bedrock and topsoil type. These site effects and collateral hazards which can be induced by ground shaking need to be considered in seismic hazard assessment. As these effects are regionally site-related the morphology and topography of the study area was considered in the selection of the site effects and collateral hazards to be included in the hazard map. In this study, the exposure was defined as the ensemble of the assets at risk that can be disturbed by an earthquake event. The vulnerability of the assets was defined as the potential of the building environment to sustain loss due to the occurrence of a hazard event, in this case an earthquake. The earthquake risk was defined as the potential of loss (physical, monetary, human) due to an earthquake for a defined area and a reference time period. The earthquake hazard map displaying the collateral hazards due to ground shaking and an exposure map displaying the assets at risk weighted according to their vulnerability and importance were combined to a scenario-based, deterministic risk map.

In chapter 2, the study area is introduced which served as a test site for the developed methodology (objective 2). It is located south of Yogyakarta City on the very far foothills of Mount Merapi. The topography of the study area is dominated by the wide spread unconsolidated sediments of the Yogyakarta and Sleman formation. Overlain by a thick layer of soft sediments, in general the study area exhibits a shallow terrain, only in the western part the foothills of the Wonosari limestone plateau has some slope. From a drilling campaign conducted by Sir MacDonald and Partner in 1984, information on the ground-water level in the study area was available. The ground-water level is gradually decreasing from northwest to the southeast, ranging from 0,5m to 11m depth. The drilling profiles also provided information on the topsoil.

## Discussion and Conclusion

---

The dominating topsoil category is sandy topsoil, covering over 60% of the study area. This combination of ground conditions justified the selection of ground amplification and liquefaction as the collateral hazards to be considered in the hazard map.

In this presented study, no field survey for data collection was conducted and therefore the study completely relied on data collated by other research institutions, companies or working groups. The issue of data availability and data-related uncertainty was addressed in section 2.5. Most uncertainty arises from the missing information on how the employed data were collected and on the year of data acquisition. The problem of questionable data up-to-dateness was met by using pre-event Quickbird imagery for which the acquisition data was known (see chapter 5). However, this was only feasible for the land use data set. For applied population density, data no validation was possible as external, confident source on population were unavailable. A quantitative uncertainty assessment was not feasible for the underlying data of this study. It can be concluded that a certain degree of uncertainty will always remain. But some sort of identification and evaluation of potential sources of error and uncertainties associated with the data used has to be part of any study conducted in order to include these uncertainties in the overall quality assessment of the results. Especially today, with an extensive amount of data and information is circulating on the internet, often without proper metadata or reference. In this context, satellite images provide a valuable source of information, for which technical uncertainties are known. In this study, no data from ground surveys after the May 2006 earthquake were available for validation. This is often the case for rural areas as the major focus of survey after disasters is on urban areas with higher population density and high value assets. However, rapidly extracted damage pattern from post-event satellite imagery might serve as a guide to coordinate survey in rural areas in the future.

In the field of emergency management, satellite image are mainly used to provide information on the impact and extent of an event in urban areas. A range of techniques for urban damage distribution extraction from very-high resolution optical image already exist. Despite all technical advances in image processing, visual interpretation can yet not be replaced by computer programs. However, existing software offer a range of useful tools and an experience image interpreter can achieve high degrees of image classification accuracy. In addition to the image processing-related issues, some conditions for using satellite imagery for damage detection were identified in section 3.4. The kind of building damage which can be detected depends on the nadir-angle at which the image scene is recorded. Damage types like soft-storey collapse and walls cracks can only be observed from oblique, off-nadir images as the roof might still look intact on a nadir image. In this study, near nadir-images are employed and building damage is identified as debris piles instead of assessing the damage state of individual buildings.

In addition to the image related constraints, most existing damage detection methodologies were developed for urban areas and specific earthquake events and are not readily transferable to other sites. The fourth objective of this study was to compare the suitability of existing pixel-based and

object-oriented techniques to extracted building damage from pre-and post-event images for the May 2006 Yogyakarta earthquake (see chapter 4). With both techniques a total debris extent of 0,61 km<sup>2</sup> was identified. These consistent results were initially misleading. To assure that the identified damage is related to buildings and not other structures, the resulting debris layer were exported to ArcGIS and an overlay analysis was conducted using building outline previously manually digitized from a pre-event Quickbird image. This analysis revealed that the only 1/3 of changed pixels identified by the pixel-based approach was actually related to buildings. The remaining changed pixels were related to other source of change. In contrast, 80 % of the debris detected by the object-based technique was related to buildings. The major source of error for the pixel-based approach was the large time gap of 3 years between the pre- and post event image due to scarce image availability. Seasonal changes as different cropping periods for paddy fields do not constitute a major source of change as the image were recorded both in the same season. More likely, land use changes like new infrastructure construction like roads and settlements or clearance may have caused confusion. Previous studies document successful application of change detection for building damage detection using Quickbird images with a time gap of 1 year (Li & Tao, 2005; Adams 2004; Samadzadegan & Rastiveisi, 2007). In addition, the rather low image quality including a cloud cover of 49% had an influenced the image classification results. Consequently, for the analysis of the relation between building damage and damage influencing factors, the results obtained by the object-oriented image analysis were used (see section 6.1.)

Quickbird image were also employed in the development of the exposure map. As no additional information of up-to-dateness and quality of the data was available, the potential for Quickbird image for improving and updating land use data set is explored (objective 5). Chapter 5 presents an object-oriented methodology for land use / land cover detection from Quickbird images. The analysis conducted in chapter 5 leads to the conclusion that even associated with limited accuracy Quickbird images can improve land use data sets as at least the date of the land information is now known and can be considered as a known source of uncertainty. It has to be pointed out, that previous studies on land cover extraction using Quickbird image yield higher accuracy values but the dense vegetation and complex land use pattern of the test site lowered the accuracy in this study. Therefore, it is concluded that the feasibility of improving land use data using remote sensing strongly depends on the local environment of the study site.

In chapter 6, the methodology for generation earthquake risk maps was presented. In order to determine the relations between observed building damage and damage influencing factors, the extracted building damage pattern were analysed as a function of damage influencing factor. The following factors were considered: (1) topsoil, (2) bedrock, (3) sediment thickness, (4) slope, (5) ground-water depth, and (6) distance to epicentre. For each factor categories were defined and the normalized percentage of urban damage was calculated. In addition, the correlations between the factors were analysed. The analysis of urban damage as a function of topsoil revealed that the most urban damage occurred in areas with clayey topsoil. Almost equal damage percentages were observed for sandy topsoil and sand & gravel. No urban damage occurred in areas with no topsoil

## Discussion and Conclusion

---

cover. The geologic setting of the study area is dominated by widespread unconsolidated sediments. The analysis showed that the most damage occurred in areas with Quaternary sediments. Comparable low percentages of damage were observed in Quaternary alluvium or tertiary volcanoclastic rocks. For sediment thickness, it became obvious that the most buildings were damaged in areas with the thickest sediment layer. This trend is also true for ground-water level. The results of the analysis show that 11,12 % of the buildings in areas with the most shallow ground-water level were damaged. The slope analysis revealed that over 8 % of the buildings built on shallow terrain (slope  $< 5^\circ$ ) were damaged. Finally, the damage distribution was analysed as a function of distance to epicentre. The analysis did not reveal a trend as with ground-water level and sediment depth. This is due to the small distance from the epicentre (19 – 29 km). Based on the results of this analysis, in section 6.1 a weighting scheme was developed and each category was assigned an index.

In section 6.3, a hazard map for liquefaction was developed using the weighted ground parameters including liquefaction and amplification as collateral hazards. The liquefaction susceptibility of a site mainly depends on three factors (1) depth of ground-water level, (2) geologic properties of the deposit, and (3) topsoil type. The resulting liquefaction susceptibility map displayed that due to the wide spread unconsolidated sediments 46,06 % of the study areas has a high liquefaction potential. In particular, in the eastern part of the study area saturated sandy soil and shallow ground-water level led to very high liquefaction potential. In contrast, the combination of outcropping bedrock and deep ground-water level led to low liquefaction potential in the southeast of the study area. Section 6.4 presented the development of a ground amplification hazard map, considering the following parameters: (1) sediment depth, (2) topsoil and (3) bedrock. The amplification susceptibility was calculated based on an overlay analysis of the weighted parameters. The resulting hazard map displayed that the north-western part of the study areas has a high to very high susceptibility due to the great sediment thickness underlain by unconsolidated sediments. In contrast, the south-eastern part had low susceptibility due to the combination of a thin sediment layer and hard bedrock. In section 6.5 a hot spot analysis was conducted to identify areas susceptible to liquefaction and ground amplification. The collateral hazard hotspots were concentrated in the north-western part and in the middle of the study area.

The next step in the risk map developed constituted in the generation of an exposure map. The considered assets were residential buildings and population density. Both assets were weighted according to their vulnerability. The improvement of the land use data using Quickbird images was demonstrated by generating two exposure maps, one based on the pre-existing land use data including residential area polygons and the other using remotely-sensed built-up area. The comparison of the resulting exposure maps revealed the same distribution of vulnerability categories. High vulnerability areas were located in the north-western part of the study area due to high population density and low vulnerability areas in the south-eastern part of the study area due to low population density. However, a closer inspection revealed that using built-up areas instead of residential polygons a more realistic picture of the vulnerability distribution was

obtained. This main reason for this is that residential polygons also include vegetation and other land cover defined as residential due to their proximity to human settlements.

In section 6.7, the development of the risk map was presented by conducting an overlay analysis of the hotspot map for collateral hazards and the exposure map. The risk map displayed that there were a high percentage of high risk areas in the north-western part of the study area due to the high population density (2500 – 3000 people per km<sup>2</sup>) and the ground conditions with shallow ground-water level, thick layers of young sediments and sandy topsoil. The risk map also showed a trend of decreasing risk from northwest to southeast. This was due to decreasing and lacking topsoil cover, decreasing sediment thickness but increasing ground water depth in southeast direction. In addition, the sub-districts in the south-eastern part of the study areas had a lower population density than the rest of the study area. In order for this method to be easily reproducibly, the methodological steps and the related data requirements are listed in Table 23.

Table 23: Methodological steps for earthquake risk map development and required data sets

No.	Methodological Steps	Data required
1	Collection of ground parameter information and generation of vector layers	Bedrock geology, topsoil, ground-water level, sediment thickness, land use information, population information
2	Extraction of building damage pattern from selected earthquake event	Very-high resolution satellite images e.g. Quickbird, Worldview 2
3	Analysis of ground parameters as a function of urban damage and analysis of the correlations between the parameters	Data sets generated in steps no. 1 and 2
4	Development of liquefaction susceptibility map	Ground-water level, bedrock geology, Topsoil type
5	Development of ground amplification susceptibility map	Bedrock geology, topsoil type, sediment thickness
6	Development of collateral hazard hot spot map	Liquefaction susceptibility map Amplification susceptibility map
7	Development of exposure map	Residential or built-up areas, population density
8	Development of earthquake risk map	Collateral hazard hot spot map, exposure map

### 7.2 Conclusion and outlook

The proposed methodology enables the generation of an earthquake risk map based on simple and commonly available data. The required resolution for the ground parameter input information is rather low and therefore much easier to derive from existing maps and other documents. This is especially important for rural, remote regions with limited data availability.

The method allows for determining the damage influencing factors and the correlation between the individual factors. The identified factors and their degree of influence form the basis for weighting scheme development. Therefore, the weighting is only regionally valid for the selected event. The regional validity of the weighting is based on the assumption that the ground conditions of neighbouring regions are very similar. Using the developed weighting scheme, earthquake risk maps can be developed for neighbouring regions. In case of an earthquake striking this region, the building damage pattern of this earthquake can be used to recalibrate the weighting schema to the event. In order to validate this assumption of regional similarity, the presented method has to be applied to different neighbouring regions which have been affected by the same earthquake. The resulting weighting scheme should be compared to analyse if and in what the influence of different parameters varies spatially. In case the method is transferred to neighbouring regions, other collateral hazards could also be included depending on the geological conditions. In case of steeper terrain, landslides and rock falls should be considered and a set of qualitative indicators to assess the susceptibility to these hazards has to be developed.

Due to the semi-quantitative nature of the generated earthquake risk map, the accuracy is less than for detailed, quantitative microzonation maps. However, the required accuracy of an earthquake risk map strongly depends on the application it is designed for. In many parts of the world earthquake risk is still poorly assessed and detailed risk assessment studies are not available or of unknown quality. Here proposed risk map development methodology provides a practical and objective procedure to assess earthquake risk with moderate data requirement.

This kind of risk maps can be used in various applications. Earthquake risk maps can be used by land use planners to implement earthquake risk into land use planning e.g. to avoid the development of new settlements or building critical buildings like hospitals in high earthquake risk zones. In order to integrate information on earthquake risk into risk-sensitive planning and to be operational for governments, the proposed methodologies initially tested for test site in this study can be easily transferred to an administrative spatial unit for example the sub-districts of Bantul in which the study site is located in. For each sub-districts on the distribution of earthquake risk zones can be provided and the sub-districts can be ranked according to the earthquake risk. This way risk-relevant information can be implemented in planning processes towards risk mitigation, even in rural areas with limited resources for mitigation efforts like compliance of existing building codes. This makes the earthquake risk maps a useful tool for risk communication and decision making. In addition, for emergency planning, the spatial distribution

of different risk zones can help to identify areas in the need for large resources to handle a future emergency. Civil protection agencies can use earthquake risk maps to plan size and location of emergency services. In the aftermath of an earthquake, the risk map can help to identify areas suitable for establishing temporary shelter or reconstructing destroyed buildings. A detailed study of what kind of earthquake risk maps with respect to resolution and degree of information detail are employed by different institutions and stakeholder for disaster management would be very useful since the need of the user's could considered in the methodology development.



## 8 References

- Adams, B., 2004.** Improved disaster management through post-earthquake building damage assessment using multi-temporal imagery. In *Proceedings of the XXth ISPRS Congress*. Istanbul, 2004.
- Aki, B., 1988.** Local site effects on strong motion. In *Earthquake engineering and soil dynamics II - recent advantages on ground motion evaluation*. ASCE. pp.103 - 105.
- Baatz, M. et al., 2004.** *ecognition User Guide*. München.
- Baatz, M. & Schäpe, A., 2000.** Multiresolution segmentation: an optimization approach for high quality multi-scale image segmentation. In *Proceedings of the AGIT Symposium*. Salzburg, 2000.
- Baltsavias, F., 2004.** Object extraction and revision of image analysis using existing geodata and knowledge: Current status and steps towards operational systems. *International Journal of Photogrammetry and Remote Sensing*, (58), pp.129 - 151.
- Bardet, J., 2003.** Advances in analysis of soil liquefaction during earthquakes. In *International Handbook of Earthquake and Engineering Seismology Part B*. Lee, W.; Jennigns, P.; Kisslinger, C. ed. Academic Press. pp.1175 - 1201.
- Benz, U. et al., 2004.** Multi-resolution, object-oriented fuzzy analysis of remote sensing data for GIS-ready information. *International Journal of Photogrammetry and Remote Sensing*, pp.239 - 258.
- Bitelli, G., Camassi, R., Gusella, L. & Mognol, A., 2004.** *Image change detection on urban area: the earthquake case*. International Society of Photogrammetry and Remote Sensing.
- Blaß, H. & Fellmoser, P., 2007.** *Schadensanalyse von Bauwerken in Indonesien nach einem Erdbeben*. Karlsruhe: Universität Karlsruhe (TH), Lehrstuhl für Ingenieurholzbau und Baukonstruktion.
- Boore, D., Joyner, W. & Fumal, T., 1997.** Equations for estimating horizontal response spectra and peak acceleration from western North-American earthquakes: a summary of recent work. *Seismol.Res.Lett.*, pp.128 - 153.
- Brandes, H., 2003.** Geotechnical and Foundation Aspects. In *Earthquake Engineering Handbook*. Chen, W.; Scawthorn, C. ed. CRC Press. pp.7.1 - 7.53.

## References

---

- Brüstle, W., Renault, P., Schlüter, F. & Swain, T., 2007.** Erdbebenschäden bei Yogyakarta, Indonesien. In K. Meskouris & P. Renault, eds. *DGEB Erkundungsreise vom 01.07.-12.07.2006 Erdbebenschäden bei Yogyakarta, Indonesien*. Weimar: Deutsche Gesellschaft für Erdbebeningenieurwesen und Baudynamik e.V.
- Campbell, K., 1981.** Near-source attenuation of peak horizontal acceleration. *Bull.Seismol.Soc.Am.*, (71), pp.2039 - 2070.
- Campbell, J., 2002.** *Introduction to remote sensing*. 3rd ed. The Guilford Press.
- Carleer, A. & Wolff, E., 2006.** Region-Based Classification Potential for Land-Cover Classification with Very High Spatial Resolution Satellite Data. In *Proceedings of the Conference on Object-oriented Image Analysis (OBIA)*. Salzburg, 2006.
- Chiroiu, L. & Andre, G., 2001.** Damage assessment using high resolution satellite imagery application to 2001 Bhuj earthquake. *Risk World*.
- Chiroiu, L., Andre, G., Guillande, R. & Bahoken, F., 2002.** Earthquake damage assessment using high-resolution satellite imagery. In *Proceedings of the 7th U.S. National Conference on Earthquake Engineering*. Boston, 2002.
- Chokkalingam, U., Bhat, D. & Von Gemmingen, G., 2001.** Secondary forests associated with the rehabilitation of degraded lands in tropical Asia: A synthesis. *Journal of Tropical Forest*, pp.816 - 831.
- Definiens, 2007.** *Definiens Developer 7 Reference Book*.
- Di Gregorio, A. & Jansen, L., 1997.** A new concept for a land cover classification system. In *Proceeding of the Earth Observation and Evolution Classification*. Alexandria, 1997.
- Eastman, J., Jin, W., Kyem, P. & Toledano, J., 1995.** Raster procedure for multi-criteria / multi-objective decisions. *Photogrammetric Engineering & Remote Sensing*, (61), pp.539 - 547.
- EERI, 2006.** Liquefaction. What it is and what to do about it. In *Earthquake Basic Brief No. 1*. Earthquake Engineering Research Institute.
- Estrada, M., Yamazaki, F. & Matsuoka, M., 2001.** Use of Landsat Images for the identification of damage due to the 1999 Kocaeli earthquake. In *Proceedings of the 21th Asian Conference on Remote Sensing*., 2001.

**eurimage, 2010.** *eurimage price list*. [Online] Available at: HYPERLINK "www.eurimage.com" [www.eurimage.com](http://www.eurimage.com) [Accessed February 2010].

**Field, E., 2000.** A modified ground-motion attenuation relationships for southern California that accounts for detailed site classification and a basin - depth effect. *Bull.Seismol.Soc.Am*, (90), pp.209 - 221.

**Frauman, E. & Wolff, E., 2005.** Segmentation of very high spatial resolution satellite images in urban areas for segments-based classification. In *Proceedings of the ISPRS Joint Conference 3rd International Symposium Remote Sensing and Data Fusion Over Urban Areas (URBAN 2005) and 5th International Symposium Remote Sensing of Urban Areas (URS 2005)*. Tempe, 2005.

**Geist, H. & Lambin, E., 2002.** Proximate causes and underlying driving forces of tropical deforestation. *BioScience*, pp.143 - 150.

**Gusella, L., 2006.** *Use of Remote Sensing Technology for Disaster Mitigation*. Dissertation thesis. University of Bologna.

**Hamada, M., Ioyama, R. & Wakamatsu, K., 1995.** *The 1995 Hyogoken-Nanbu (Kobe) Earthquake, Liquefaction, Ground Displacement, and Soil Condition in Hanshin Area..* Association of Development of Earthquake Prediction.

**Hays, W., 1981.** *Facing geologic and hydrologic hazards - Earth Science Considerations*. USGS Professional Paper 1240 B.

**Herold, M., Scepan, J., Müller, A. & Günther, S., 2002** Object-oriented Mapping and Analysis of Urban Land Use/Cover Using IKONOS Data. In *Proceedings of the 22nd EARSeL Symposium on Remote Sensing*. Prague, 2002a.

**Hisada, Y., Shibayama, A. & Ghayamghamian, M., 2005.** Building damage and seismic intensity in Bam City from the 2003 Iran, Bam, earthquake. *Bull. Earthquake Res. Inst.*, 79, pp.81 - 94.

**Holekamp, K., 2006.** *Radiometric characterization of the IKONOS, QuickBird and Orb-View sensors*. Maryland: Science Systems and Applications, Inc. John C. Stennis Space Center.

## References

---

- Holmes, K., Chadwick, O. & Kyriakidis, P., 2000.** Error in a USGS 30-meter digital elevation model and its import on terrain modeling. *Journal of Hydrology*, (233), pp.154 - 173.
- Huyck, C., Adams, B., Sungbin, C. & Eguchi, R., 2005.** Towards rapid citywide damage mapping using neighborhood edge dissimilarities in very high-resolution optical satellite imagery - application to the 2003 Bam, Iran earthquake. *Earthquake Spectra*, (21), pp.255 - 266.
- International Charter, 2009.** *International Charter Space and Major Disasters*. [Online] Available at: HYPERLINK "www.disasterscharter.org" [www.disasterscharter.org](http://www.disasterscharter.org) [Accessed February 2010].
- Ivits, E., 2005.** *Tasselled Cap parameters for Ikonos*. Dissertation thesis. University Freiburg i. Brsg.
- Kauth, R. & Thomas, G., 1976.** The tasselled cap - A graphic description of the spectral-temporal development of agricultural crops as seen bey Landsat. In *Proceeding of the Symposium of Machine Processing of Remotely Sensed Data.*, 1976.
- Kawase, H., 2003.** Site Effects on Strong Ground Motions. In *International Handbook of Earthquake and Engineering Seismology (Part B)*. Lee, W.; Kanamori, P.; Kissinger, C. ed. Academic Press. pp.1013 - 1030.
- Kawasumi-Hiroshi, H., 1968.** *General report on the Niigata earthquake of 1964*. Tokyo: Tokyo Electrical Engineering College Press.
- Kerle, N., 2006.** Geoinformation-based response to the 27 May Indonesia earthquake - An initial assessment. In *Proceeding of the 27th Asian Conference on Remote Sensing*. Ulanbaatar, 2006.
- Kouchi, K. & Yamazaki, F., 2005.** Damage detection based on object-oriented segmentation and classification from high-resolution satellite images for the 2003 Bourmedes, Algeria earthquake. In *Proceedings of the Asian Conference on Remote Sensing*. Hanoi, 2005.
- Kumar, K., Martha, T. & Roy, P., 2006.** Mapping damage in the Jammu and Kashmir caused by 9 October 2005 M7.3 earthquake from the Cartosat-1 and Resourcesat-1 imagery. *International Journal of Remote Sensing*, 27, pp.4449 - 4459.
- Lee, Y. & Anderson, J., 2000.** Potential of improving ground motion relations in Southern California by incorporating various site parameters. *Bull.Seismol. Soc. Am.*, 90, pp.170 - 186.

- Liao, S., Veneziano, D. & Whitmann, R., 1988.** Regression models for evaluating liquefaction probability. *Journal of Geotechnical Engineering*, 114(4).
- Lillesand, T., Kiefer, R. & Chipman, J., 2008.** *Remote Sensing and Image Interpretation*. 6th ed. Wiley&Sons.
- Matsui, T. & Oda, K., 1996.** Foundation damage of structures. *Soils and Foundation, Special Issue 1*, Japanese Geotechnical Society, pp.189 - 200.
- Matsumoto, K., Vu, T. & Yamazaki, F., 2006.** Extraction of damaged buildings using high-resolution satellite images in the 2006 Central Java earthquake. In *Proceedings of the Conference of the Remote Sensing Society of Japan.*, 2006.
- Matsuoka, M. & Yamazaki, F., 1998.** Identification of damaged areas due to the 1995 Hyogoken-Nanbu earthquake using satellite optical images. In *Proceeding of the Asian Conference on Remote Sensing.*, 1998.
- Mirua, H., Yamazaki, F. & Matsuoka, M., 2006.** Building damage mapping of the 2006 central Java, Indonesia, earthquake using satellite optical images. In *Proceedings of the 4th International Workshop on remote sensing for post-disaster response*. Cambridge, 2006.
- Mitomi, H., Yamazaki, F. & Matsuoka, M., 2001.** Development of automated extraction method for building damage area based on maximum likelihood classifier. In *Proceeding of the 8th International Conference on Structural Safety and Reliability.*, 2001.
- Miura, H., Yamazaki, F. & Matsuoka, M., 2007.** Identification of damaged areas due to the 2006 central Java, Indonesia, earthquake using satellite optical images. In *Proceeding of the Urban Remote Sensing Joint Event*. Paris, 2007.
- NRC, 1999.** *Global Environmental Change: Research Pathways for the next decade*. Washington, D.C.: National Academy Press National Research Council, Board on Sustainable Development, Policy Division.
- Olgun, E., 2000.** Izmit (Turkey) earthquake, August 17, 1999 and the application of change detection techniques for damage assessment using Spot 4 satellite images., 2000.
- Ozirik, D., 2004.** *Post-earthquake damage assessment using satellite and aerial video imagery*. Dissertation thesis. University of Twente.
- Pang, A., 2008.** Visualizing Uncertainty in Natural Hazards. In Springer, ed. *Risk Assessment, Modeling and Decision Support*. Berlin.

## References

---

- Rahardjo, W., Sukandarrumidi, F. & Rosidi, H., 1997.** *Geological map of Yogyakarta - 135 quadrangle Java*. Yogyakarta.
- Rathje, E., Crawford, M., Woo, K. & Neuenschwander, A., 2005b.** Damage patterns from satellite image of the 2003 Bam, Iran, earthquake. *Earthquake Spectra*, 21, pp.295 - 307.
- Rathje, E., Woo, K., Crawford, M. & Neuenschwander, A., 2005a.** Earthquake damage identification using multi-temporal high-resolution optical satellite imagery. In *Proceedings of the IEEE International Geoscience and Remote Sensing Symposium*. Seoul, 2005a.
- Saito, K., 2008.** *High-resolution optical satellite images for post-earthquake damage assessment*. Dissertation thesis. Cambridge: Department of Architecture, University Cambridge.
- Saito, K. & Spence, R., 2004.** Image classification methods and post-earthquake damage assessment. In *2nd Workshop on remote sensing for disaster response*. Newport Beach, 2004.
- Saito, K., Spence, R., Going, C. & Markus, M., 2004.** Using high-resolution satellite images for post-earthquake building damage assessment: a study following the 26 January 2001 Gujarat earthquake. *Earthquake Spectra*, 20(1), pp.145 - 169.
- Satellite Imaging Cooperation, 2010.** [Online] Available at: HYPERLINK "www.satimagingcorp.com" [www.satimagingcorp.com](http://www.satimagingcorp.com) [Accessed March 2010].
- Scawthorn, C., 2003.** Earthquake Risk Management: An Overview. In F.-W. Chen & C. Scawthorn, eds. *Earthquake Engineering*. 1st ed. Boca Raton: CRC Press.
- Schowengerdt, R., 2007.** *Remote sensing: model and methods for image processing*. Academic Press Elsevier.
- Seed, H. & Wilson, S., 1973.** The Turnagain Heights landslides, Anchorage Alaska. In *The Great Alaska Earthquake of 1964*. Washington: National Academy of Science. pp.120 - 143.
- Shackelford, A. & Davis, C., 2003.** A hierarchical fuzzy classification approach for high resolution multispectral data over urban areas. *IEEE Transactions on Geoscience and Remote Sensing*, 41, pp.1920 - 1932.
- Shirzaei, M., Mansouri, B. & Shinozuka, M., 2006.** Multiresolution analysis of satellite optical images for damage detection using wavelet transform. In *Proceedings of the 4th International Workshop on Remote Sensing for Disaster Response*. Cambridge, 2006.

- Singh, A., 1989.** Digital change detection techniques using remotely sensed data. *International Journal of Remote Sensing*, 10(6), pp.989 - 1003.
- Sir MacDonald & Partners, 1984.** *Greater Yogyakarta - Groundwater resource study.* Government of the Republic of Indonesia, Ministry of Public Work, Directorate General of Water Resource Development.
- Smyth, H., Hall, R., Nichols & G., 2008.** Cenozoic volcanic arc history of East Java, Indonesia: The stratigraphic record of eruptions on an active continental margin. In *Formation and Applications of the Sedimentary Record in Arc Collision Zones: Geological Society of America Special Paper 436.* Draut, A.; Clift, P.; Scholl, D. ed. pp.199 - 222.
- Stewart, J., 1997.** *Key Geotechnical Aspects of the 1989 Loma Prieta Earthquake.* Berkeley: National Information Service for Earthquake Engineering.
- Thomas, N., Hendrix, C. & Congalton, R., 2003.** A comparison of urban mapping methods using high-resolution digital imagery. *Photogrammetric Engineering and Remote Sensing*, pp.963 - 972.
- Trifunca, M. & Lee, V., 1979.** *Dependence of pseudo-relative velocity spectra of strong motion acceleration on the depth of sedimentary deposits.* Los Angeles: Department of Civil Engineering, University of Southern California.
- Tuker, M. & San, B., 2003.** SPOT HRV data analysis for detecting earthquake-induced change in Izmit, Turkey. *International Journal of Remote Sensing*, 24, pp.2439 - 2450.
- US Geological Survey, 1997.** *USGS Earthquake Hazard Program.* [Online] USGS Available at: HYPERLINK "<http://earthquake.usgs.gov/earthquakes/world/indonesia/gshap.php>" <http://earthquake.usgs.gov/earthquakes/world/indonesia/gshap.php> [Accessed 2009].
- Vu, T., Matsuoka, M. & Yamazaki, F., 2005.** Preliminary results in development of an object-based image analysis method for earthquake damage assessment. In *Proceedings of the 3rd International Workshop on Remote Sensing for Disaster Response.* Chiba, 2005.
- Walter, T. et al., 2007.** Soft volcanic sediments compound 2006 Java earthquake disaster. *EOS, Transactions American Geophysical Union VOL. 88, NO. 46.*
- Wechsler, S. & Kroll, C., 2006.** Quantifying DEM Uncertainty and its Effect on Topographic Parameters. *Photogrammetric Engineering & Remote Sensing*, 72(9), pp.1081 - 1090.

## References

---

- Weidner, U., 2006.** Analysis and comparison of different high-resolution data sets for urban applications. In *Proceedings of the ISPRS Commission VII Mid-Term Symposium - From Pixels to Processes.*, 2006.
- Weidner, U. & Bähr, H., 2007.** Vergleich von pixel- und segmentbasierter Klassifizierung am Beispiel des Kaiserstuhls.. In *Proceedings of 27. wissenschaftliche Jahretagung der DGPF.* Muttentz, 2007.
- Woo, K., Rathje, E. & Crawford, M., 2005.** Comparison of earthquake damage evaluation using change detection and thematic classification. In *Proceedings of the 3rd International Workshop on Remote Sensing for Disaster Response.* Chiba, 2005.
- Yamazaki, F. et al., 2004.** Damage detection from high-resolution satellite images for the 2003 Boumerdes Algeria earthquake. In *13th World Conference on Earthquake Engineering.* Vancouver, 2004.
- Yamazaki, F., Yano, Y. & Matsuoka, M., 2005.** Visual Damage Interpretation of Buildings in Bam City using Quickbird Images following the Bam 2003, Iran, Earthquake. *Earthquake Spectra*, 21(1), pp.329 - 36.
- Youd, T., 1992.** Liquefaction, Ground failure and consequent damage during the 22 April 1991 Costa Rica Earthquake. In *Proceedings of the NSF / UCR U.S. Costa Rica Workshop on the Costa Rica Earthquake of 1990 - 1991: Effect on Soils and Structures.* Oakland, 1992. Earthquake Engineering Research Institute.
- Youd, T. & Perkins, D., 1978.** Mapping liquefaction induced ground failure potential. *Journal of the Geotechnical Engineering Division*, pp.433 - 446.
- Yuan, D., Elvidge, C. & Lunetta, R., 1999.** Survey of multispectral methods for land cover change analysis. In Lunetta, R. *Remote Sensing Change Detectio: Environmental monitoring methods and application.* London: Press, Sleeping Bear.
- Yusuf, Y., Matsuoka, M. & Yamazaki, F., 2003.** Damage detection from Landsat 7 satellite images for the 2001 Gujuarat, India earthquake. In *Proceedings of the 22nd Asian Conference on Remote Sensing.*, 2003.

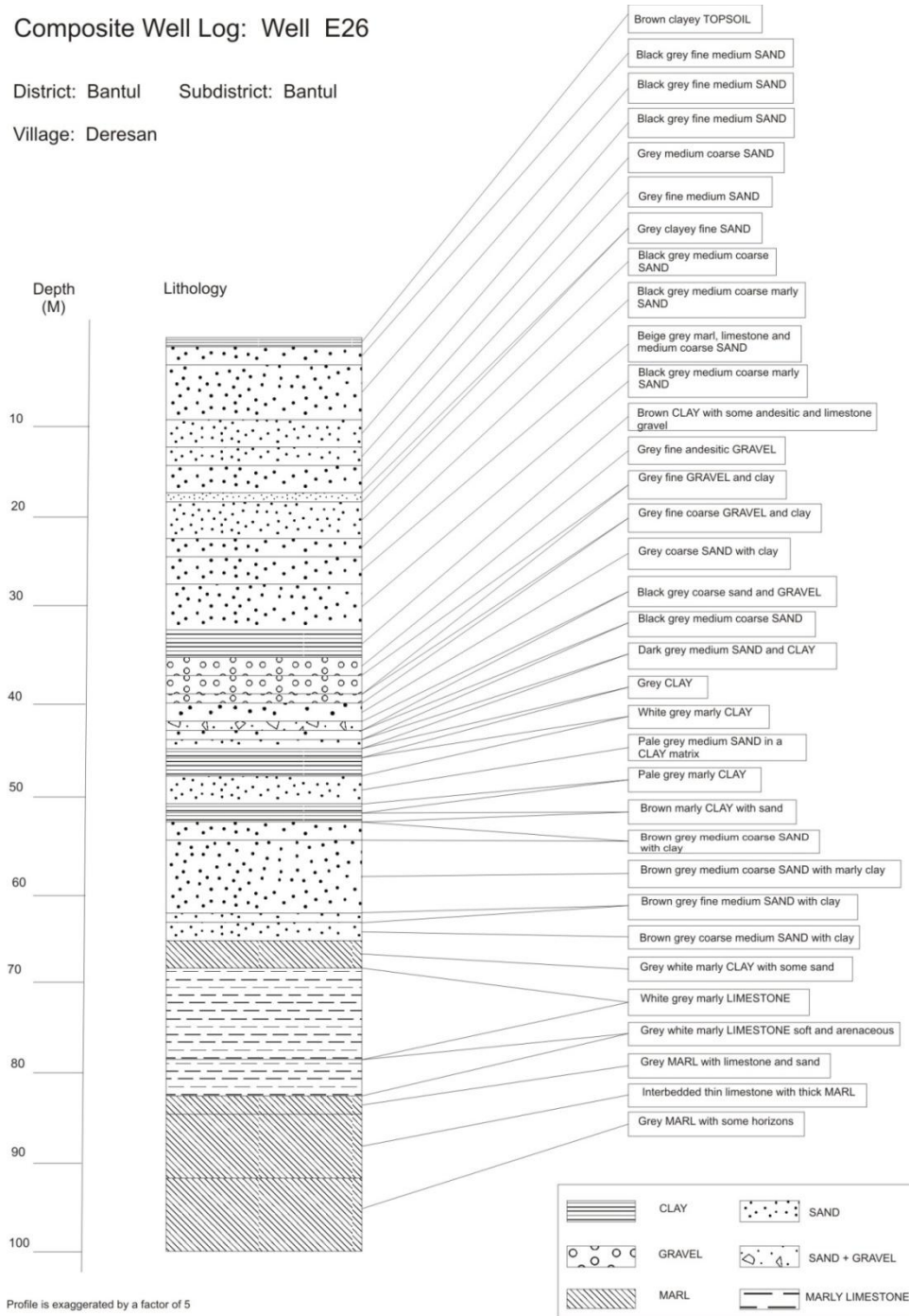
# Appendix I

# Appendix I

## Composite Well Log: Well E26

District: Bantul Subdistrict: Bantul

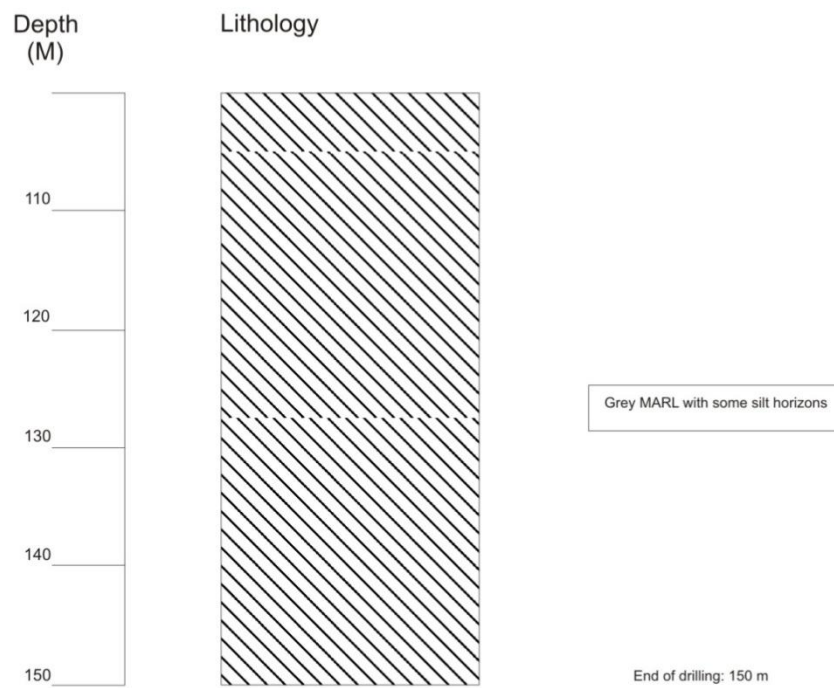
Village: Deresan



### Composite Well Log: Well E26

District: Bantul Subdistrict: Bantul

Village: Deresan

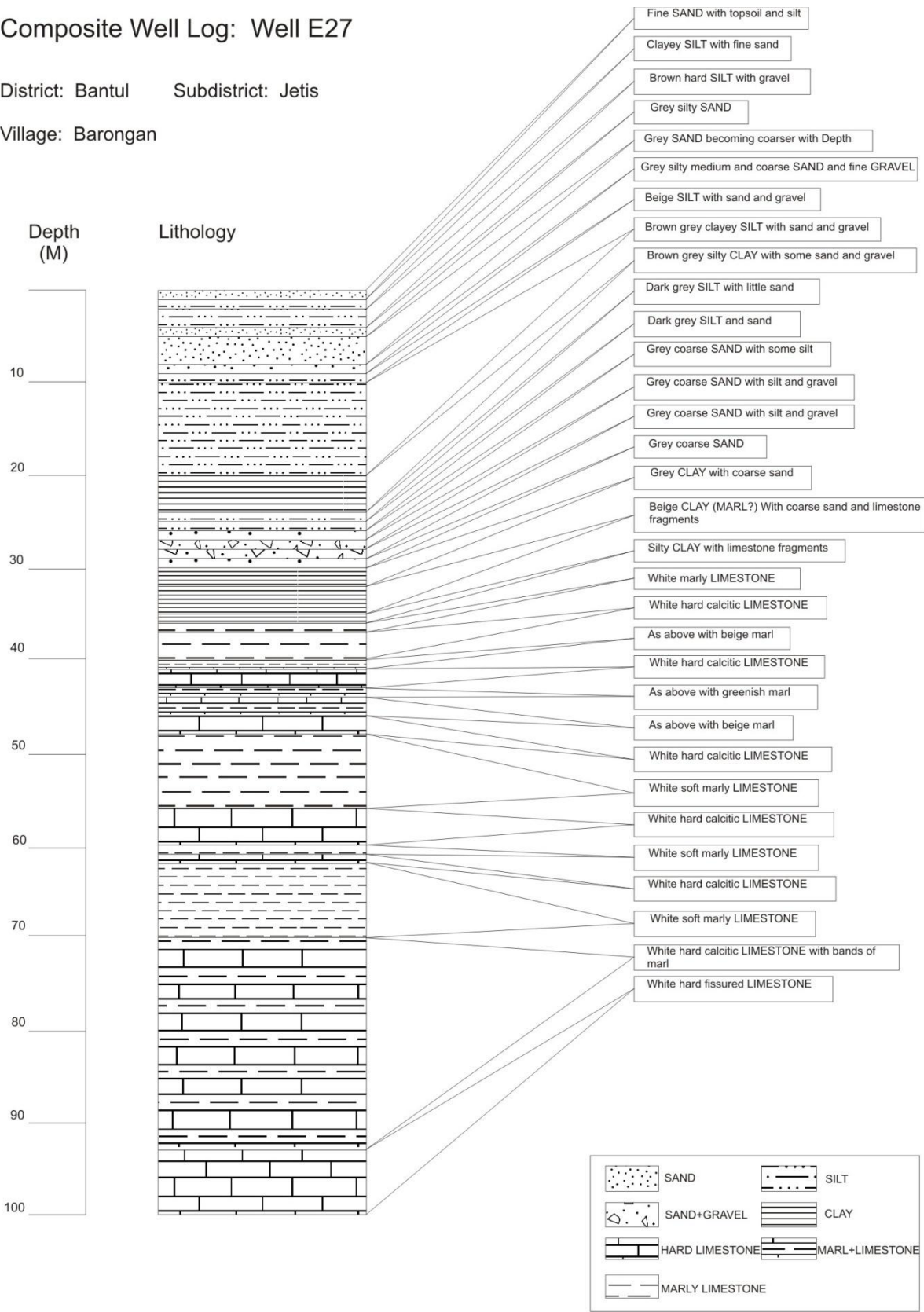


# Appendix I

## Composite Well Log: Well E27

District: Bantul Subdistrict: Jetis

Village: Barongan

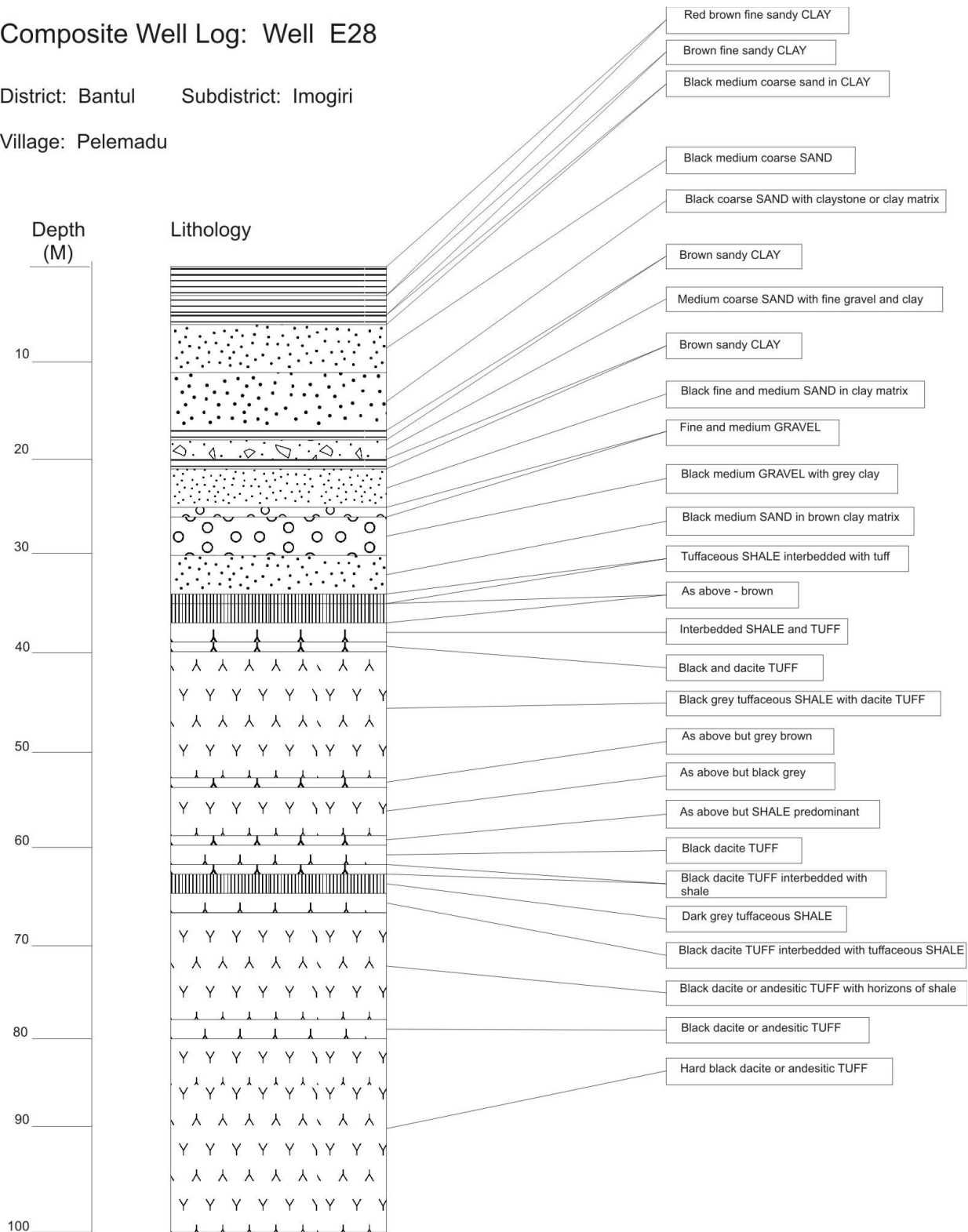


Profile is exaggerated by a factor of 5

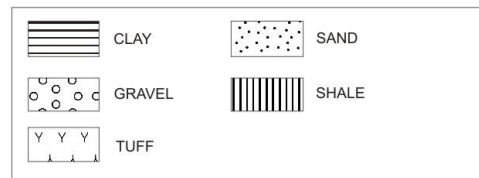
# Composite Well Log: Well E28

District: Bantul Subdistrict: Imogiri

Village: Pelemadu



Profile is exaggerated by a factor of 5

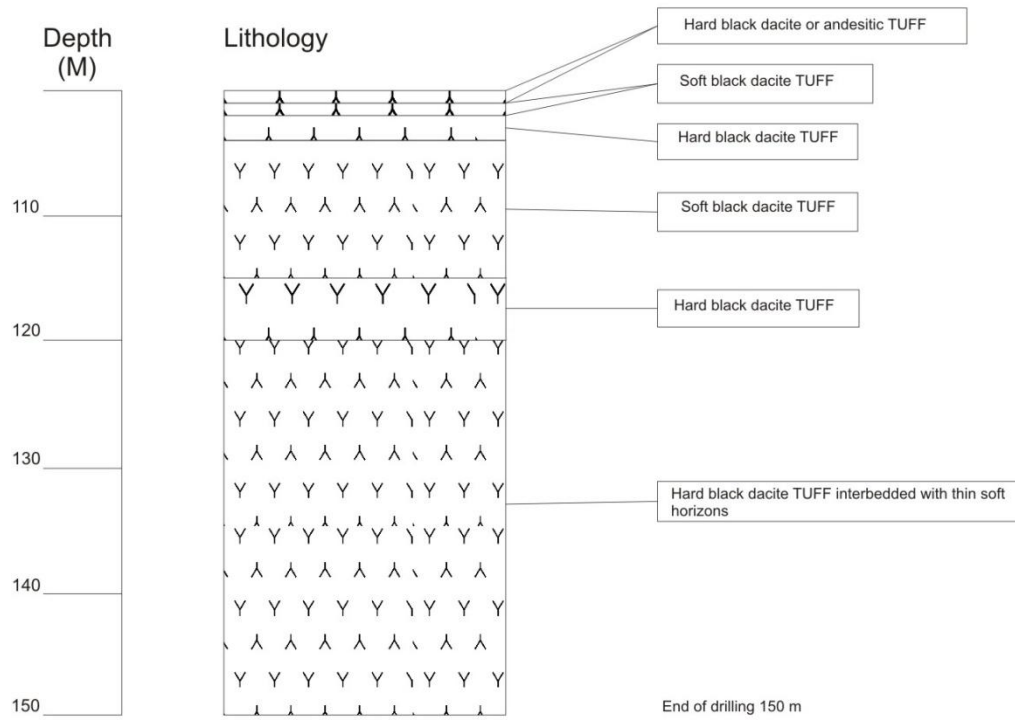


# Appendix I

## Composite Well Log: Well E28

District: Bantul Subdistrict: Imogiri

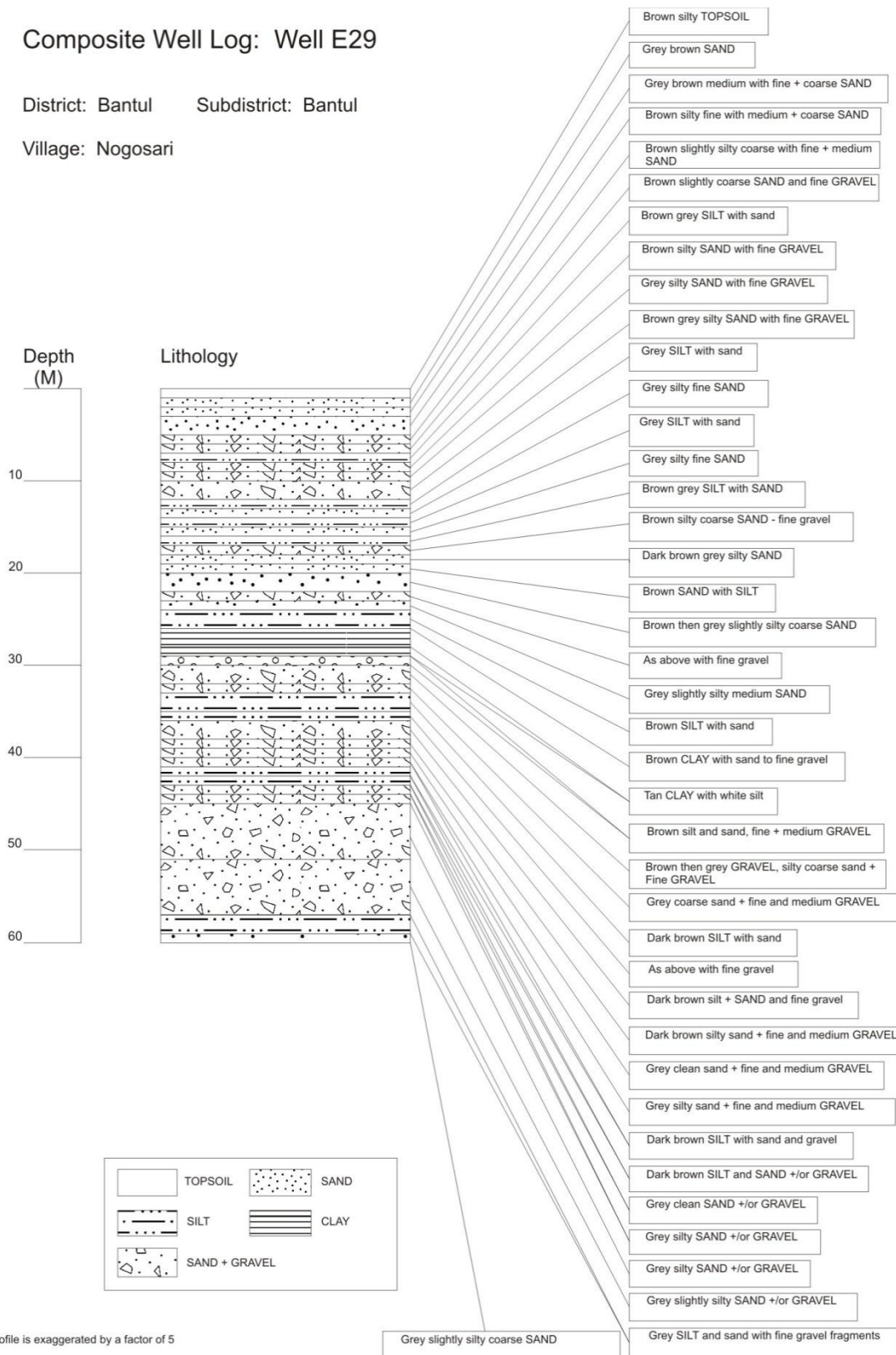
Village: Pelemadu



### Composite Well Log: Well E29

District: Bantul Subdistrict: Bantul

Village: Nogosari

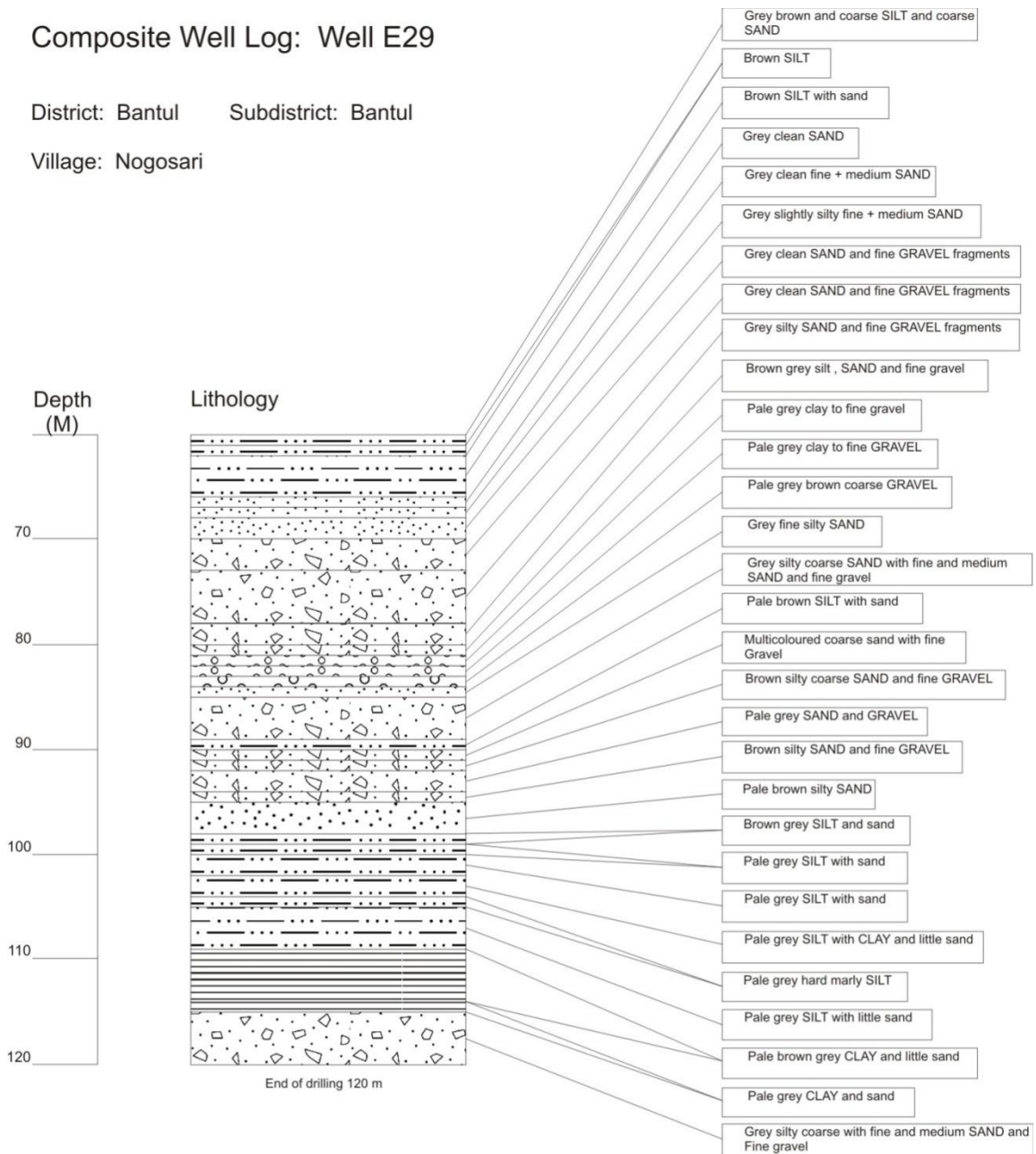


# Appendix I

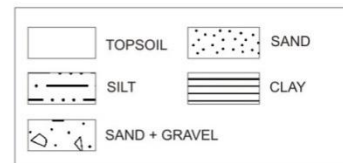
## Composite Well Log: Well E29

District: Bantul Subdistrict: Bantul

Village: Nogosari



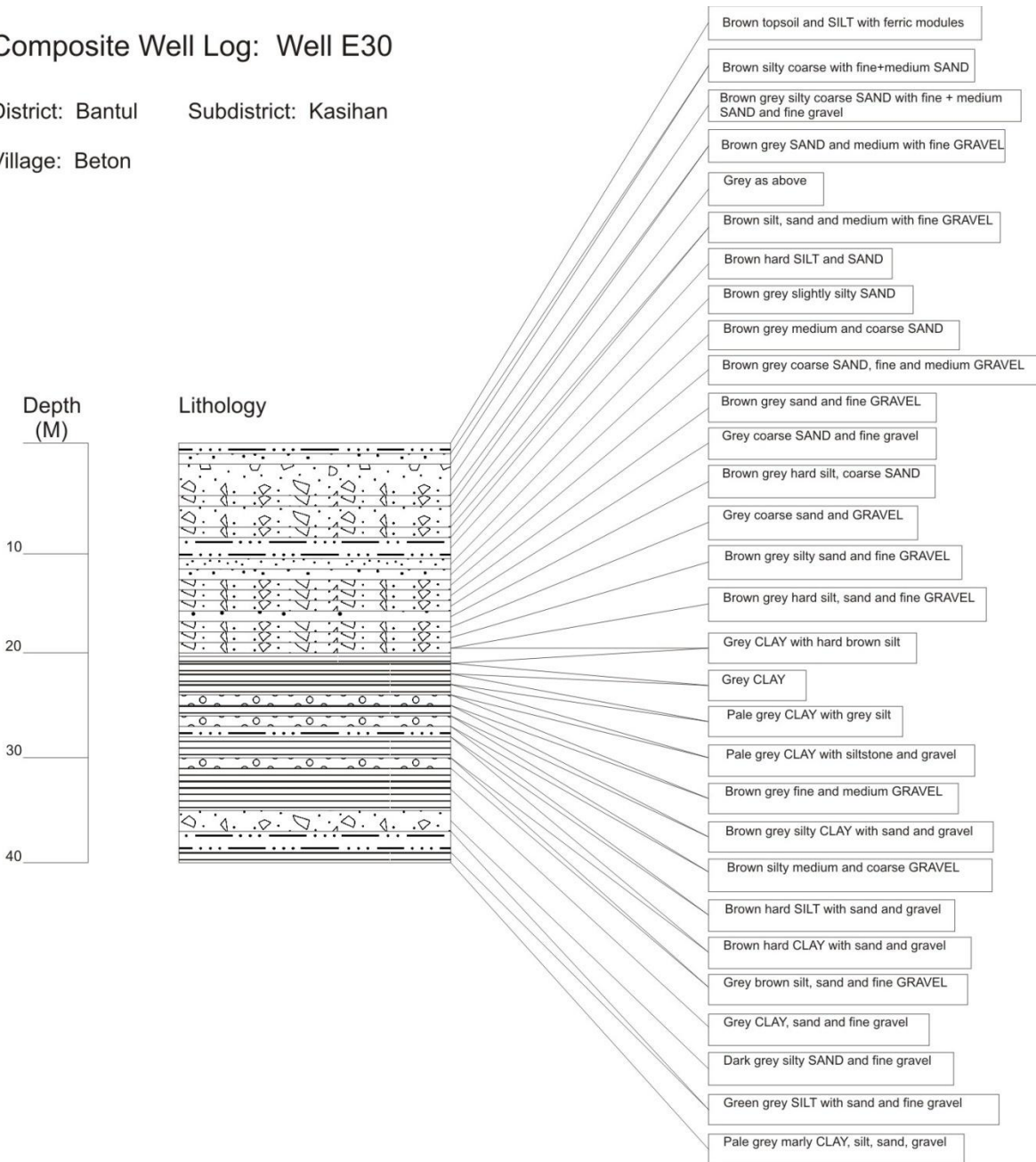
Profile is exaggerated by a factor of 5



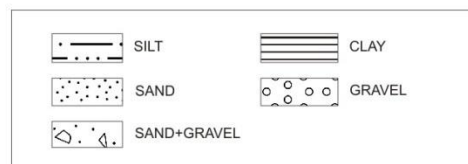
### Composite Well Log: Well E30

District: Bantul Subdistrict: Kasihan

Village: Beton



Profile is exaggerated by a factor of 5

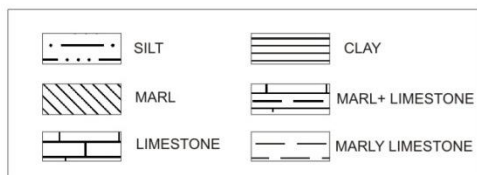
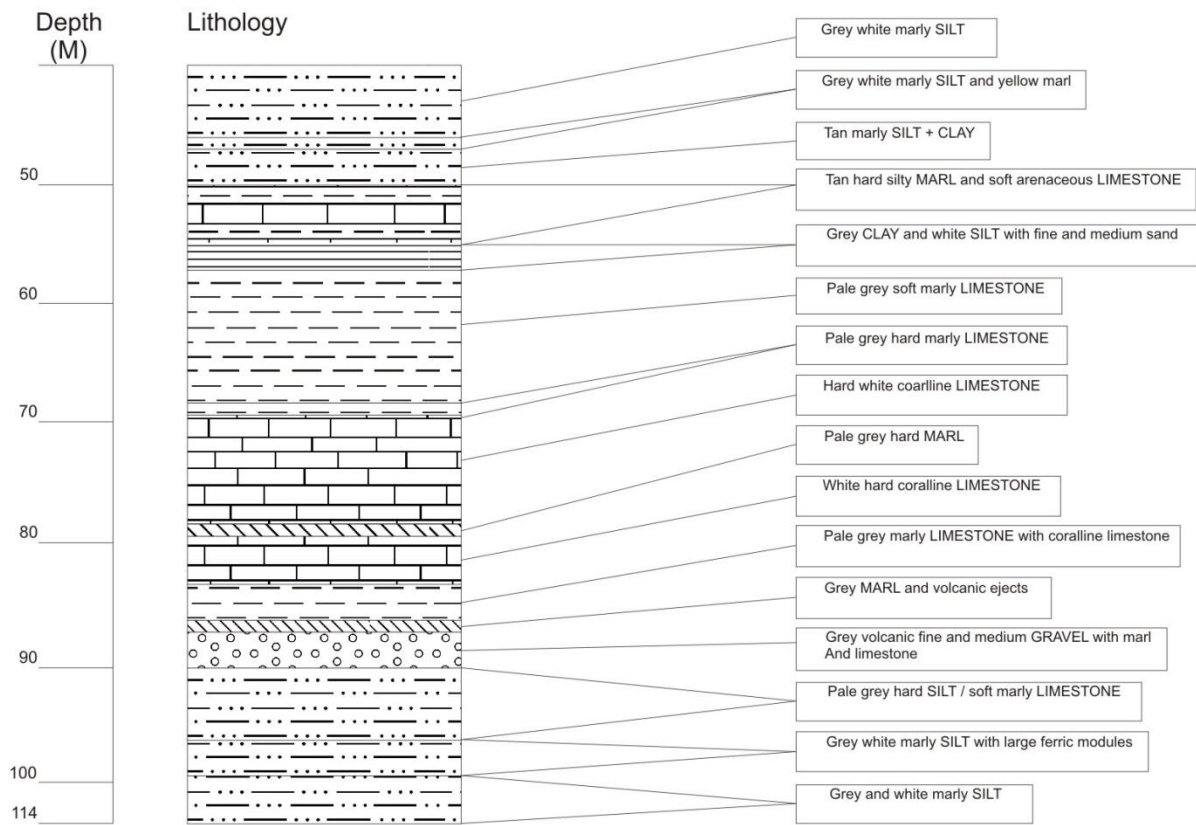


# Appendix I

## Composite Well Log: Well E30

District: Bantul Subdistrict: Kasihan

Village: Beton

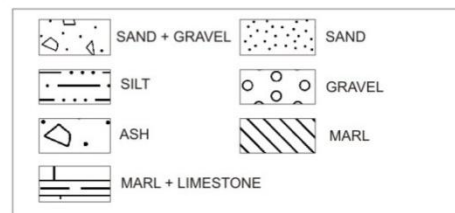
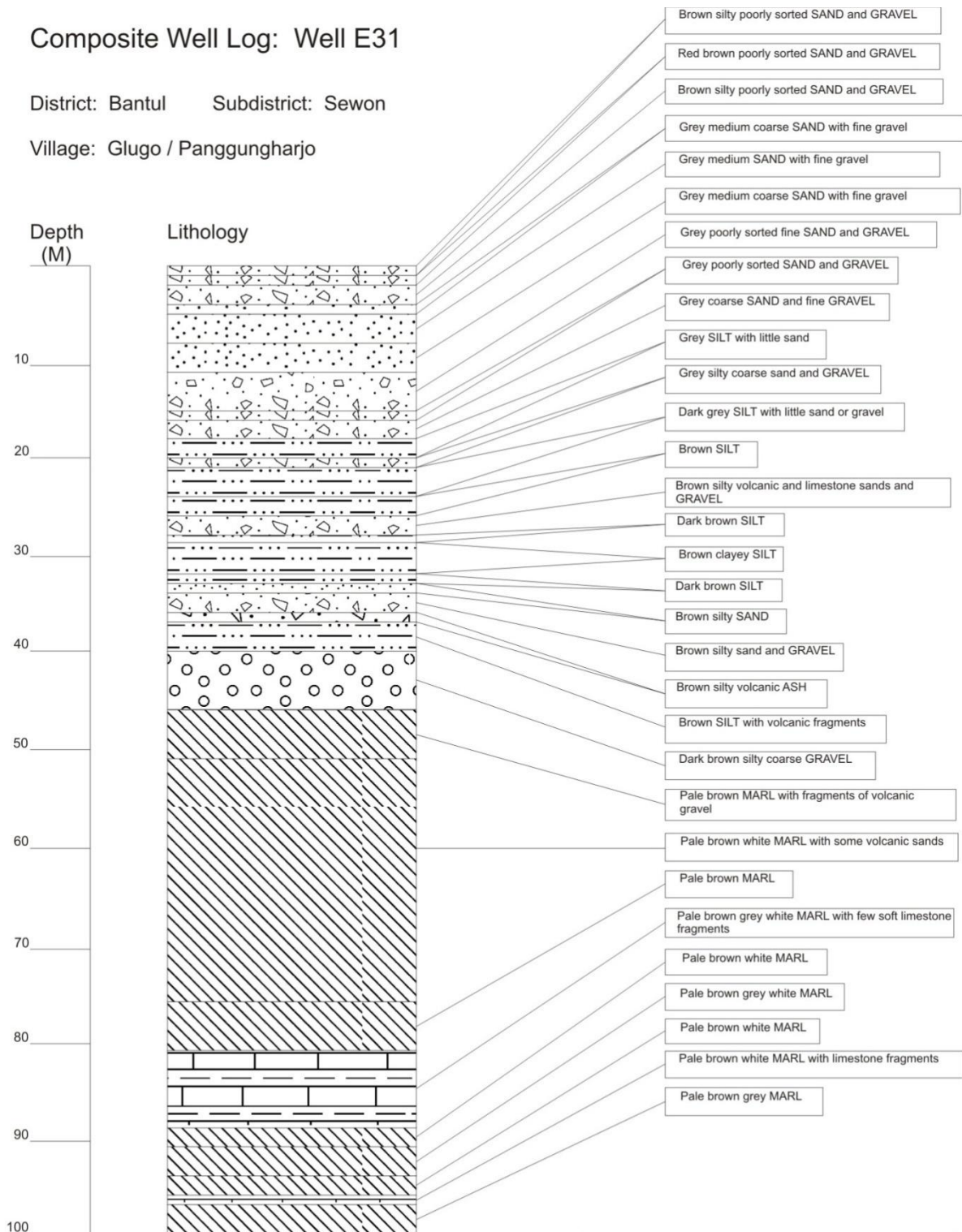


Profile is exaggerated by a factor of 5

### Composite Well Log: Well E31

District: Bantul Subdistrict: Sewon

Village: Glugo / Panggunharjo



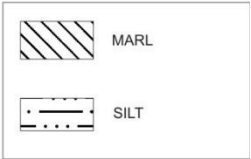
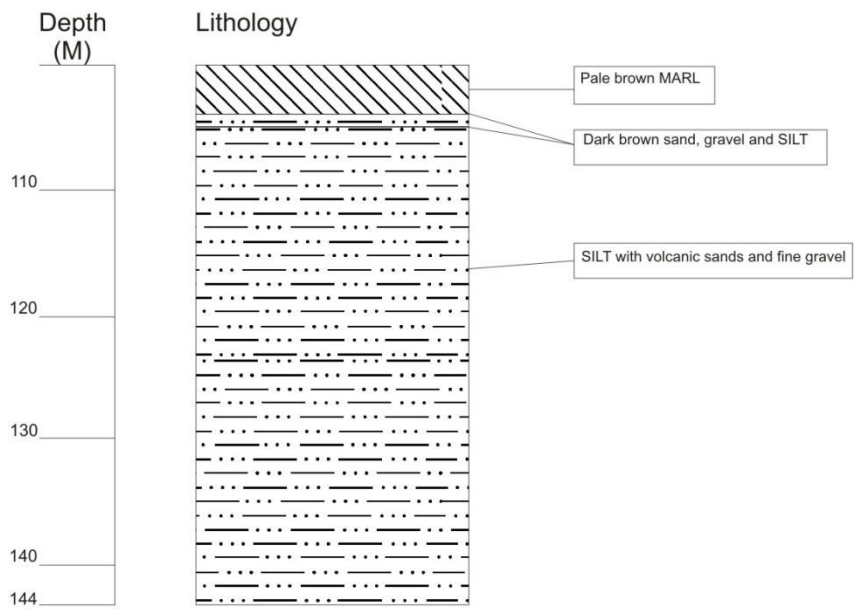
Profile is exaggerated by a factor of 5

# Appendix I

## Composite Well Log: Well E31

District: Bantul Subdistrict: Sewon

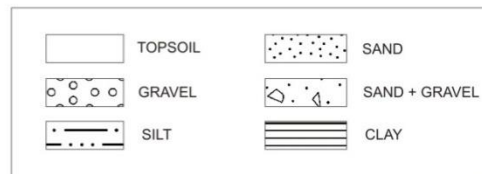
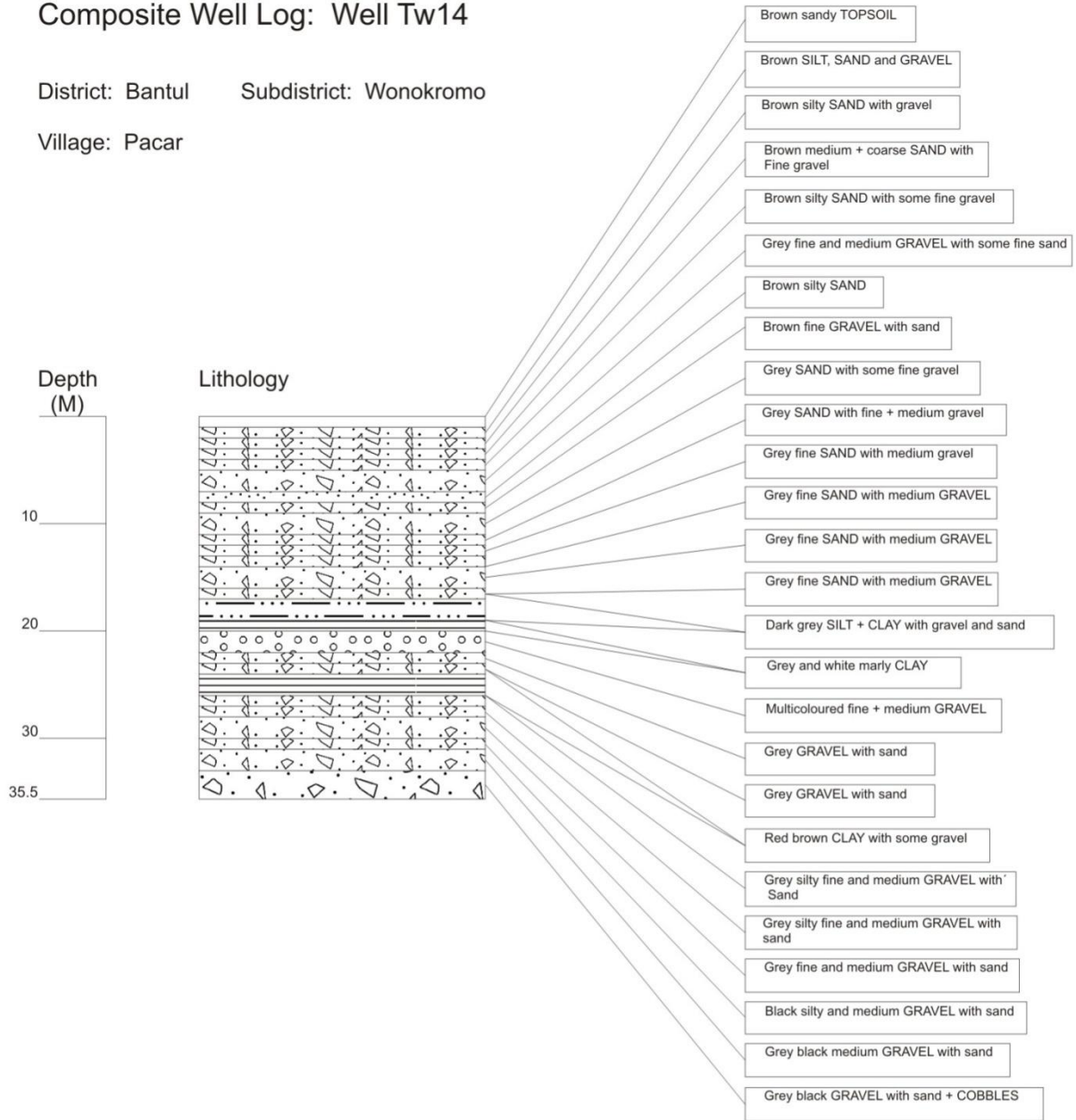
Village: Glugo / Panggunharjo



### Composite Well Log: Well Tw14

District: Bantul Subdistrict: Wonokromo

Village: Pacar

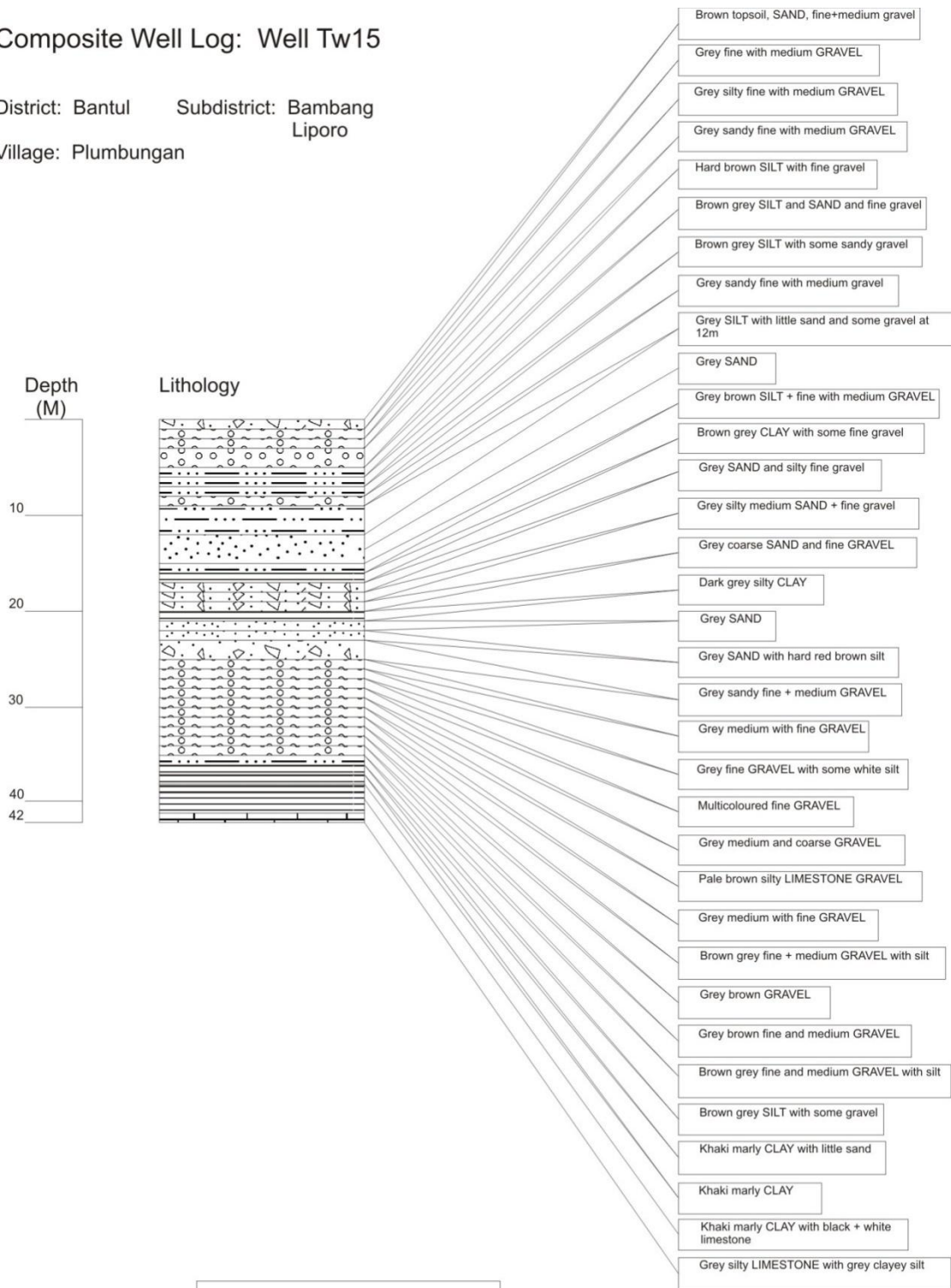


Profile is exaggerated by a factor of 5

# Appendix I

## Composite Well Log: Well Tw15

District: Bantul      Subdistrict: Bambang Liporo  
 Village: Plumbungan

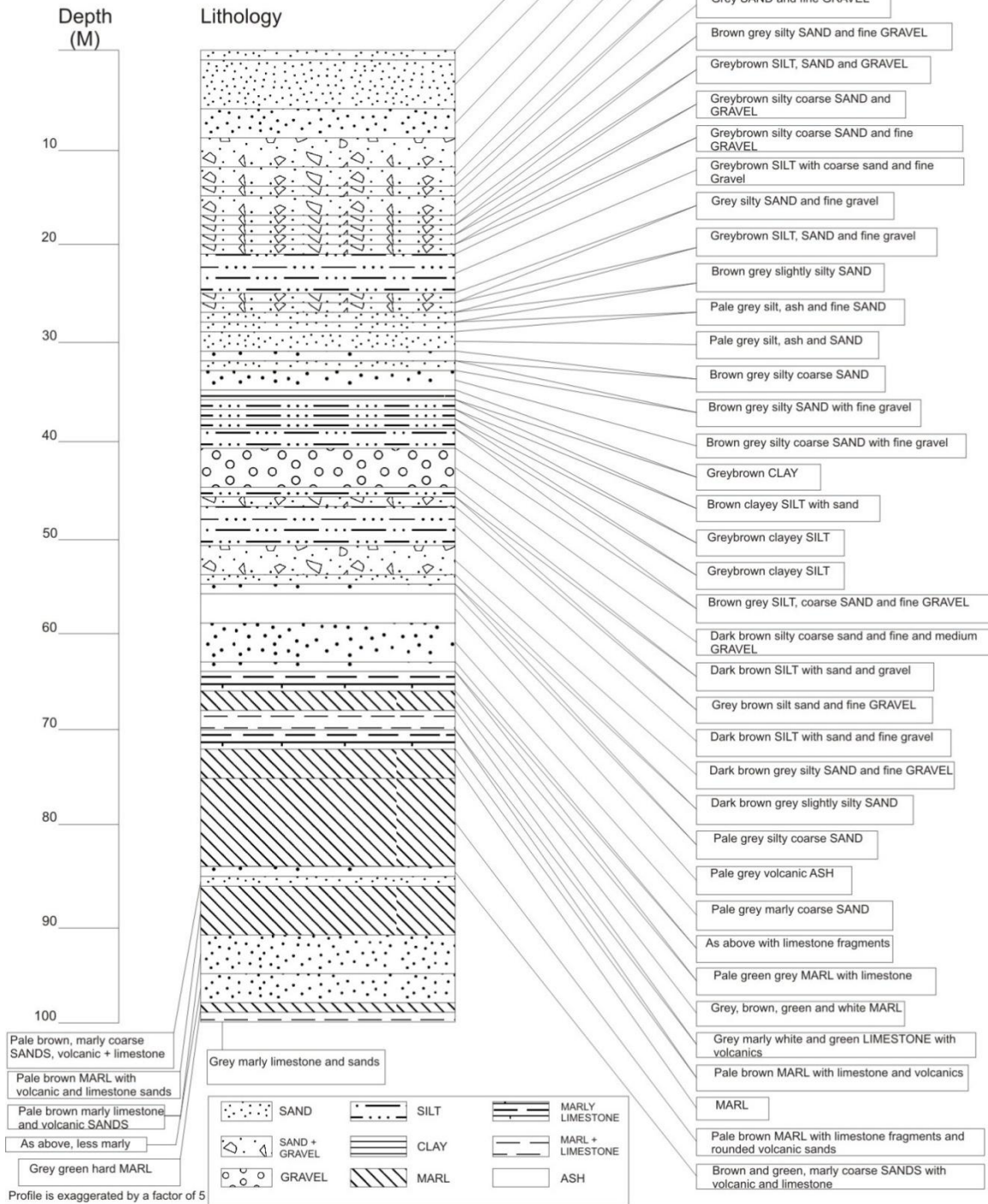


Profile is exaggerated by a factor of 5

### Composite Well Log: Well Tw21

District: Bantul Subdistrict: Sewon

Village: Glugo

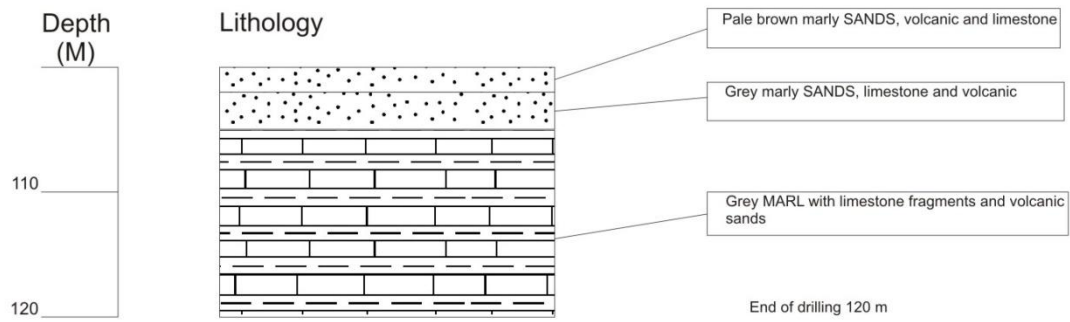


# Appendix I

## Composite Well Log: Well Tw21

District: Bantul      Subdistrict: Sewon

Village: Glugo



## Appendix II

Table 24: List of ground control points used for the co-registration of the pre- and post-event images in section 4.1.1.

<b>GCP</b>	<b>Quickbird 2003</b>	<b>Quickbird 2006</b>	<b>Spatial off-set</b>
1	E 429959,600	E 429986,000	-26,40
	N 9131703,200	N 9131717,600	-14,40
2	E 433019,600	E 433046,000	-26,40
	N 9130812,800	N 9130815,200	-02,40
3	E 430442,000	E 430480,400	-38,40
	N 9124289,600	N 9124284,800	04,80
4	E 431843,600	E 431882,000	-38,40
	N 9123761,600	N 9123761,600	00,00
5	E 429966,800	E 429995,600	-28,80
	N 9128818,400	N 9128816,000	02,40
6	E 431351,600	E 431382,800	-31,20
	N 9129749,600	N 9129754,400	-04,80
7	E 430470,800	E 430504,400	-33,60
	N 9127044,800	N 9127047,200	-02,40

# List of Figures

Figure 1 : Tectonic Setting of Indonesia. The Australian plate dips north-north-eastward beneath the Sunda Plate(US Geological Survey, 1997)..... 12

Figure 2: Seismic hazard map for Indonesia. The Island of Java has a moderate to high hazard with PGA ranging from 1,6 to 3,2 g/ m<sup>2</sup> for a 10 % exceedance probability in 50 years (US Geological Survey, 1997). ..... 13

Figure 3: Regional, seismic hazard map for Java. On a small scale the map shows a smooth hazard distribution of the moderate hazard with ranging from 1,6 to 2,4 g/ m<sup>2</sup> for a 10 % exceedance probability in 50 years (US Geological Survey, 1997)..... 13

Figure 4: Quickbird panchromatic satellite image. Left: Pre-event image acquired 11.07.2003. Right: Post-event image captured four days after the earthquake (31.05.2006). The red rectangles indicate buildings that were destroyed by the May 2006 earthquake. ... 15

Figure 5: Location of study area in the Special Region of Yogyakarta, south cost of Java. .... 15

Figure 6: Methodology flow diagram illustrating two different procedures applied for damage detection from Quickbird imagery. .... 29

Figure 7: Segmentation and Classification applied on Quickbird imagery. Figure A shows an image object representing a single house. Figure B shows the same Image Object classified as a House with a red roof..... 32

Figure 8: Classes hierarchy used for the image classification and features applied in the class description. .... 33

Figure 9: Rubble classified using object-oriented image classification; the colour code corresponds to the classes in figure 6. .... 33

Figure 10: Snapshot of 2D Feature Space Plot. The plot displays the correlation between the red and the NIR band. .... 38

Figure 11: Segmentation with incrementally increasing scale parameter for the land cover class grass land. The correlation curve displays an initial, steep decrease in the number of image objects between a scale parameter of 10 and 30..... 40

Figure 12: Methodology flow diagram for multi-resolution segmentation and classification of pre-event Quickbird imagery to determine an up-to-date land use inventory..... 42

Figure 13: Classes hierarchy used for image classification and features applied in the class description for the different land use / land cover classes..... 43

Figure 14: Land use / land cover map generated from pre-event Quickbird Imagery using an object-oriented, multi-resolution approach. The colour scheme corresponds to the class hierarchy in Figure 13. ....	45
Figure 15: (A) Original Quickbird image (true colour), (B) Segmentation for Quickbird image (C) Classification Stability: The smaller Segments show lower Classification Stability (red segments), (D) Classification for Quickbird image.....	47
Figure 16: Location of reference data sets for object-oriented accuracy assessment and manually digitized classes from pre-event, panchromatic Quickbird Imagery acquired 2003. ....	48
Figure 17: Diagram with surface percentage of all reference data sets compared to the classification results.....	48
Figure 18: Soil map for the study area. The majority of the study area is covered by sandy topsoil.....	52
Figure 19: Distribution of urban damage as a function of topsoil and ground water depth. The most damage is observed in areas with clayey topsoil and shallow ground water depth. No damage was observed in areas with no topsoil and outcropping bedrock.....	53
Figure 20: Geological map of the study area. The Quaternary sediments are the dominate bedrock formation. ....	55
Figure 21: Distribution of urban damage as a function of sediment thickness. No distinct correlation between urban damage and sediment thickness can be observed.....	56
Figure 22: Distribution of urban damage as a function of slope and topsoil. The most damage occurred in areas with slope < 5° and sandy topsoil.....	58
Figure 23: Distribution of urban damage as a function of distance to epicentre. The distribution of urban damage revealed no distinct correlation.....	59
Figure 24: Liquefaction susceptibility map of the study area. With 46,06 % the majority of the study areas exhibits a moderate liquefaction susceptibility. About 31 % of the study areas exhibit high liquefaction susceptibility.....	62
Figure 25: Ground amplification susceptibility map. Large parts of the north-western part of the study area exhibit a high to very high susceptibility. ....	65
Figure 26: Hotspot map for ground amplification and liquefaction. The areas with the highest susceptibility are located in the north-western part due to the shallow ground water level and unconsolidated sediments.....	66
Figure 27: (Left) Destroyed building near Bantul. (Right) Collapsed building (masonry / reinforced concrete) in Bangunharjo. The images were taken by the taskforce of the German Society for Earthquake Engineering and Building Dynamics (DGEB). ....	67

## List of Figures

---

- Figure 28: Exposure map of study area including residential areas and population density. (Right) Exposure map based on manually digitized residential areas, (Left) exposure map based on remotely sensed residential areas..... 69
- Figure 29: Comparison of residential areas delineated from satellite imagery (yellow) and manually digitized (blue). Note that the blue polygon does not only include buildings but also vegetation and bare soil, where the yellow polygons only include built structures. .... 70
- Figure 30: Risk map for building damage (upper figure) using manually digitized residential polygons and (lower figure) using remotely-sensing built-up areas. The zones with very high risk are mainly concentrated in the north-western part of the study area. The south-eastern part exhibits a significantly lower risk to earthquake-related building damage. The comparison reveals the generalizing effect of residential polygons. Using remotely-sensed built—up area a large degree of detail can be displayed..... 72

# List of Tables

Table 1: Characteristics of Quickbird images used in this study. ....	16
Table 2: Previous studies on building damage detection from satellite images after earthquakes using visual image interpretation.....	19
Table 3: Members and data provides of the International Charter. (International Charter, 2009).....	26
Table 4: Advantages and limitations of optical satellite imagery used for building damage detection after earthquakes.....	27
Table 5: Mean and standard deviation for defining the threshold for "changed" pixel.....	31
Table 6: NDVI ranges and Pearson's correlation coefficient for the NIR- and R-bands.....	37
Table 7: Pre-existing classes and results of suitability analysis.....	38
Table 8: Scale parameter ranges determined from the exploratory feature specific segmentation.....	41
Table 9: Confusion matrix for land user / land cover classification using Quickbird images (2003) based on 10 reference datasets. The area of each land use class in shown in ha. ....	49
Table 10: Results of the analysis of urban damage distribution as a function of topsoil and index assigned to each topsoil category.....	53
Table 11: Results of analysis of urban damage distribution as a function of bedrock and assigned index to each bedrock category .....	54
Table 12: Results of analysis of urban damage distribution as a function of sediment depth and index assigned to each category. ....	56
Table 13: Results of analysis of urban damage distribution as a function of ground-water level and index assigned to each category.....	57
Table 14: Results of analysis of urban damage distribution as a function of slope and index assigned to each category. ....	57
Table 15: Results of analysis of urban damage distribution as a function of distance to epicentre and index assigned to each category. ....	58
Table 16: Liquefaction susceptibility controlling factors and weighted categories based on the analysis of urban damage distribution.....	61

## List of Tables

---

Table 17: Liquefaction susceptibility raking with 5 classes. ....	61
Table 18: Ground amplification susceptibility controlling factors and weighted categories based on the analysis of urban damage distribution.....	64
Table 19: Ground amplification susceptibility raking using 5 classes. The majority of the study area exhibits a high to very high susceptibility.....	64
Table 20: Assets at risk used for the exposure map development. The residential areas are weighted heighted in the land use data set.....	68
Table 21: Distribution of risk zones using remotely-sensed built-up areas. ....	71
Table 22: Distribution of risk zones using manually digitized residential polygons.....	71
Table 23: Methodological steps for earthquake risk map development and required data sets .....	77
Table 24: List of ground control points used for the co-registration of the pre- and post-event images in section 4.1.1. ....	105